

ADA 040947

12

DNA 4202F

AN EVALUATION OF BOUNDARY LAYER FORCES AND MEASUREMENT METHODS

Kaman Sciences Corporation
P.O. Box 7463
Colorado Springs, Colorado 80933

October 1976

Final Report

DDC
RECEIVED
JUN 23 1977
C

CONTRACT No. DNA 001-75-C-0038

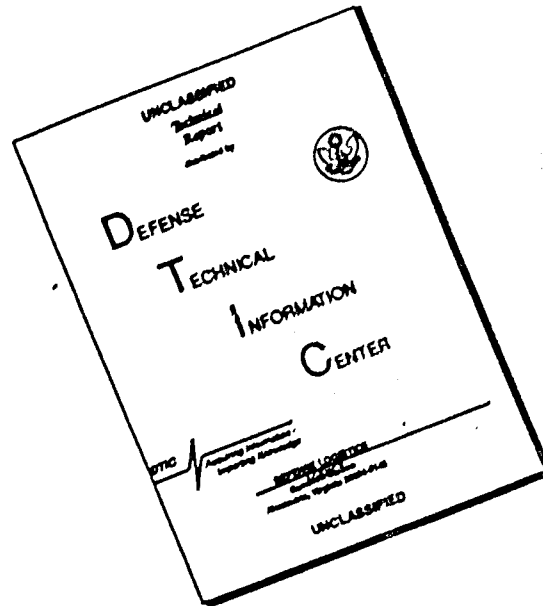
APPROVED FOR PUBLIC RELEASE;
DISTRIBUTION UNLIMITED.

THIS WORK SPONSORED BY THE DEFENSE NUCLEAR AGENCY
UNDER RDT&E RMSS CODES B342076464 N99QAXAC31324 H2590D,
B310076464 P99QAXDE50402 H2590D, AND X342075469 Q93QAXAD-
41024 H2590D.

AD NO. _____
DDC FILE COPY

Prepared for
Director
DEFENSE NUCLEAR AGENCY
Washington, D. C. 20305

DISCLAIMER NOTICE



THIS DOCUMENT IS BEST QUALITY AVAILABLE. THE COPY FURNISHED TO DTIC CONTAINED A SIGNIFICANT NUMBER OF PAGES WHICH DO NOT REPRODUCE LEGIBLY.

Destroy this report when it is no longer
needed. Do not return to sender.



UNCLASSIFIED

SECURITY CLASSIFICATION OF THIS PAGE (When Data Entered)

19 REPORT DOCUMENTATION PAGE		READ INSTRUCTIONS BEFORE COMPLETING FORM	
18 1. REPORT NUMBER	2. GOVT ACCESSION NO.	3. RECIPIENT'S CATALOG NUMBER	
DNA 4202F			
6 4. TITLE (and Subtitle)	9 5. TYPE OF REPORT & PERIOD COVERED		
AN EVALUATION OF BOUNDARY LAYER FORCES AND MEASUREMENT METHODS	Final Report		
10 7. AUTHOR(S)	14 6. PERFORMING ORG. REPORT NUMBER		
J. C. Nickell V. D. Peckham T. F. V. Meagher	K-76-118U (R)		
	15 8. CONTRACT OR GRANT NUMBER(S)		
	DNA 001-75-C-0038		
9. PERFORMING ORGANIZATION NAME AND ADDRESS		10. PROGRAM ELEMENT, PROJECT, TASK AREA & WORK UNIT NUMBERS	
Kaman Sciences Corporation P.O. Box 7463 Colorado Springs, Colorado 80933		Subtasks N99QAXAC313-24 P99QAXDE504-02 Q93QAXAD410-24	
11. CONTROLLING OFFICE NAME AND ADDRESS		12. REPORT DATE	
Director Defense Nuclear Agency Washington, D.C. 20305		11 October 1976	
14. MONITORING AGENCY NAME & ADDRESS (if different from Controlling Office)		13. NUMBER OF PAGES	
12 242p.		146	
		15. SECURITY CLASS (of this report)	
		UNCLASSIFIED	
		15a. DECLASSIFICATION DOWNGRADING SCHEDULE	
16. DISTRIBUTION STATEMENT (of this Report)			
Approved for public release; distribution unlimited.			
17. DISTRIBUTION STATEMENT (of the abstract entered in Block 20, if different from Report)			
18. SUPPLEMENTARY NOTES			
This work sponsored by the Defense Nuclear Agency under RDT&E RMSS Code B342076464 N99QAXAC31324 H2590D, B310076464 P99QAXDE50402 H2590D, and X342075469 Q93QAXAD41024 H2590D.			
19. KEY WORDS (Continue on reverse side if necessary and identify by block number)			
Boundary Layer Transition Turbulence Reentry Vehicle Forces Measurement Techniques			
20. ABSTRACT (Continue on reverse side if necessary and identify by block number)			
An analysis has been performed of the effects of asymmetric hypersonic boundary layer transition on conical reentry vehicles relative to the forces and moments acting on the vehicle. The relative importance of boundary layer thickening, increased surface mass transfer, and changes in skin friction have been addressed and the effects of each of these terms on the vehicle forces and moments have been estimated. This analysis indicates			

DDC
APPROVED
JUN 23 1977
RECEIVED
C

389 119

next page

UNCLASSIFIED

SECURITY CLASSIFICATION OF THIS PAGE (When Data Entered)

20. ABSTRACT (Continued)

→ that boundary layer thickening is the most significant factor occurring during boundary layer transition and may be a source of transient vehicle instability during the boundary layer transition event. ←

A survey has been completed of the open and classified literature to determine the state-of-the-art of boundary layer transition and pressure measuring transducers. Evaluations were made on the principal types of transducers used by experimenters. Features evaluated included response time, flow field effects, ease of calibration and overall performance. Major findings included the fact that there is no single technique which will accurately measure static pressure of reentry vehicles during flight tests, particularly after transition has occurred. Several methods were found to be capable of accurate measurement of transition events but with varying degrees of detail. Included in the transition event monitors are pressure transducers, acoustic sensors, surface thin films, and thermocouples in a variety of configurations.

UNCLASSIFIED

SECURITY CLASSIFICATION OF THIS PAGE (When Data Entered)

PREFACE

The program was monitored by Majors T. Swartz and W. Mercer of the DNA. Capt. M. Elliott of SAMSO/ABRES directed the effort and Messrs. W. Grabowski and M. Kausch of the Aerospace Corporation provided assistance and guidance. Dr. C. Lewis, VPI, provided theoretical and computational inputs to the program as a consultant to KSC. The authors gratefully acknowledge the valuable contributions made by each of the above named individuals.

APPROVED FOR	WFO Section <input checked="" type="checkbox"/>
NTIS	WFO Section <input type="checkbox"/>
U.S.	WFO Section <input type="checkbox"/>
RESTRICTED	
DISTRIBUTION	
BY	DISTRIBUTION/AVAILABILITY CODES
POST.	AVAIL. and/or SPECIAL
A	

CONVERSION UNITS

1 lb. =	.454 Kilograms
1 ft. =	.3048 meters
1 psf =	47.88026 newtons/m ²
1 Btu =	.1054 joules
1 Btu/ft ² sec =	1.13455 watts/cm ²
1 Btu/lb =	.4785 joules/gram
1 Btu/lb ^{°R} =	4.178 joules/gram ^{°K}
1 Btu/ft sec ^{°R} =	62.24 watts/cm ^{°K}
1 lb/ft ² sec =	4.887 Kg/m ² sec
1 lb force =	4.44822 newtons
1 ft·lb =	1.3558 newton·meter

TABLE OF CONTENTS

	<u>Page No.</u>
1.0 INTRODUCTION	9
1.1 Boundary Layer Transition Analysis	10
1.2 Boundary Layer Measurements - A Literature Survey	11
2.0 BOUNDARY LAYER ANALYSIS	15
2.1 Baseline Vehicle Characteristics	15
2.2 Aerodynamic Heating	15
2.3 Heatshield Ablation Response	23
2.4 Viscous and Inviscid Flow Fields	33
2.4.1 Zero Angle of Attack Analysis	33
2.4.2 Angle of Attack Analysis	59
2.4.3 Sharp Cone at Zero Angle of Attack	82
2.5 Aerodynamic Forces and Moments	86
3.0 BOUNDARY LAYER MEASUREMENTS - SURVEY RESULTS	99
3.1 Pressure Measurements	99
3.1.1 Transducer Size and Shape	101
3.1.2 Port Aerodynamics	104
3.1.3 Temperature Environments	111
3.1.4 External Noise Interference	111
3.2 Temperature Measurements	114
4.0 CONCLUSIONS AND RECOMMENDATIONS	126
4.1 Conclusions	126
4.2 Recommendations	129
5.0 REFERENCES/BIBLIOGRAPHY	131

LIST OF ILLUSTRATIONS

		<u>Page No.</u>
FIGURE 1	Reference Trajectory	16
FIGURE 2	Reference Vehicle Aerodynamic Heating Rates	22
FIGURE 3	Reference Vehicle Aerodynamic Heating Distributions at 24.384 km Altitude	24
FIGURE 4	Normalized Carbon Mass Loss in Air	28
FIGURE 5	Thermal Properties of Carbon Phenolic Char	30
FIGURE 6	Reference Vehicle Surface Temperature Histories	31
FIGURE 7	Reference Vehicle Surface Mass Loss Histories	32
FIGURE 8	Streamwise Pressure Distribution Zero Angle of Attack	42
FIGURE 9	Radial Entropy Distribution, Zero Angle of Attack	43
FIGURE 10	LTBLCEQL Wall Temperature Distribution	45
FIGURE 11	LTBLCEQL Normalized Wall Mass Transfer Distribution	46
FIGURE 12	Boundary Layer Edge Mach Number, Laminar Flow	48
FIGURE 13	Wall Shear Stress Distribution, Laminar Flow	49
FIGURE 14	Boundary Layer Displacement Thickness, Laminar Flow	50
FIGURE 15	Boundary Layer Velocity Thickness, Laminar Flow	51
FIGURE 16	Boundary Layer Edge Mach Number	54
FIGURE 17	Wall Shear Stress Distribution, Transitional Flow	55
FIGURE 18	Boundary Layer Displacement Thickness	56

LIST OF ILLUSTRATIONS (CONT'D)

		<u>Page No.</u>
FIGURE 19	Boundary Layer Velocity Thickness	57
FIGURE 20	Sharp Cone Pressure Distribution at Angle of Attack	73
FIGURE 21	Wall Shear Stress Distribution, $\alpha=1.5$ Degrees	75
FIGURE 22	Wall Shear Stress Distribution, $\alpha=3.0$ Degrees	76
FIGURE 23	Wall Shear Stress Distribution, $\alpha=4.5$ Degrees	77
FIGURE 24	Boundary Layer Displacement Thickness, $\alpha=1.5$ Degrees	78
FIGURE 25	Boundary Layer Displacement Thickness, $\alpha=3.0$ Degrees	79
FIGURE 26	Boundary Layer Displacement Thickness, $\alpha=4.5$ Degrees	80
FIGURE 27	Wall Shear Stress Comparison, Sharp Versus Blunt Cone	83
FIGURE 28	Boundary Layer Displacement Thickness Comparison, Sharp Versus Blunt Cone	84
FIGURE 29	Boundary Layer Velocity Thickness Comparison, Sharp Versus Blunt Cone	85
FIGURE 30	Boundary Layer Displacement Thickness Induced Pressure Distributions	89
FIGURE 31	Boundary Layer Displacement Thickness Induced Normal Force	92
FIGURE 32	Boundary Layer Displacement Thickness Induced Pitching Moment	93
FIGURE 33	Wall Shear Stress Pitching Moment	94
FIGURE 34	Total Normal Force With and Without Boundary Layer Effects	96
FIGURE 35	Total Pitching Moment With and Without Boundary Layer Effects	97

LIST OF ILLUSTRATIONS. (CONT'D)

	<u>Page No.</u>	
FIGURE 36	Flow Characteristics	100
FIGURE 37	Theoretical Size Correction Factor For Uniform Transducer (Reference 29)	102
FIGURE 38	Variations in the Estimated Power- Spectral-Density Measurements of the Surface-Pressure Fluctuations as Determined from 11 Different Trans- ducers (Reference 38)	103
FIGURE 39	Effect of the Flushness of a Trans- ducer Mounting on the Measurement of Wall Pressure Fluctuations (Refer- ence 34)	106
FIGURE 40	Static Hole Errors-Boundary Layer Pressure Measurements (Referene 33)	107
FIGURE 41	Comparison of Fluctuating Pressure Data from the Short and Long Port at 3.3 Nose Radii (Reference 35)	108
FIGURE 42	Power Spectral Density (Reference 32)	109
FIGURE 43	Integral Sound Pressure Levels (Reference 32)	109
FIGURE 44	Ported Gage Measurement, Flight Test (Reference 39)	110
FIGURE 45	Ported Gage Measurements (Reference 39)	112
FIGURE 46	Ported Gage Measurements, Flight Test (Reference 39)	113
FIGURE 47	Effect of Nozzle Wall Temperature on Disturbance Levels in Freestream (Reference 44)	115
FIGURE 48	Sources of Noise in Wind Tunnels (Reference 42)	116
FIGURE 49	Measurements of Fluctuation Pressures Under Laminar and Boundary Layers on a Sharp Cone in Mach 6 High Reynolds Number Tunnel at NASA Langley (Refer- ence 42)	117

LIST OF ILLUSTRATIONS (CONT'D)

		<u>Page No.</u>
FIGURE 50	Determination of Transition Location- a) Thin-Film Technique b) Thermocouple Technique (Reference 43)	118
FIGURE 51	Surface Temperature and Heat Flux, and Boundary-Layer (Reference 45)	119
FIGURE 52	Heat-Transfer Distribution on a Cone (Reference 46)	120
FIGURE 53	Thermocouple Techniques	124
FIGURE 54	Cross-Sectional Schematic of TCS Series Probe (Reference 16)	125

LIST OF TABLES

	<u>Page No.</u>
TABLE I Boundary Layer Measurands	13

1.0 INTRODUCTION

Disturbances in the motion of reentry vehicles during boundary layer transition have been observed with the assistance of on-board telemetered data for many years. These disturbances are most often observed as (1) a divergence in the angle of attack history of the vehicle, (2) an increase in the lateral rates and lateral accelerations of the vehicle, and (3) a sudden decrease, rather than a continued increase, in the aerodynamic frequency of the vehicle. These observed disturbances have been directly correlated with the inception of boundary layer transition on the heatshield of the vehicle as determined by shallow thermocouple measurements, base pressure measurements and many other transition monitoring devices. This study is concerned with:

- 1) Defining the source of trajectory disturbances which are derived from boundary layer turbulence;
- 2) Assessing the ability of existing transducers to measure these perturbing effects;
- 3) Designating transducer requirements if measurement deficiencies exist.

Analysis was applied to define and rank the perturbing forces while the transducer assessment was based upon a literature survey.

1.1 Boundary Layer Transition Analysis

In an effort to explain the source of these reentry vehicle motion disturbances resulting from boundary layer transition, calculations of the transitional hypersonic boundary layer on a typical conical reentry vehicle have been performed. The objective of these calculations was to rank the relative importance of various laminar-transitional-turbulent boundary layer parameters by determining their resultant effect on the aerodynamic forces and moments acting on the vehicle. The transitional boundary layer parameters addressed in this study were:

- 1) Boundary layer thickening due to transition;
- 2) Increased surface blowing due to transition;
- 3) Increased skin friction due to transition.

The desired result of this study was the isolation of a single parameter associated with the transitional boundary layer on a reentry vehicle which is the source of the observed vehicle motion disturbances. Another segment of this study addressed the question of how this parameter can be measured during the reentry flight and the development of instruments tailored toward this measurement.

Attention was necessarily confined to a single reentry vehicle shape flying a single reentry trajectory. The approach used to arrive at a proper description of the viscous flow field over the vehicle during boundary layer transition and the resulting aerodynamic forces and moments acting on the vehicle was as follows:

- 1) Calculate the aerodynamic heating rate history on the vehicle during the reentry.

- 2) Calculate the ablation response of the vehicle heatshield and the surface temperature, char gas and pyrolysis gas mass transfer rates into the boundary layer.
- 3) Calculate the viscous flow field over the vehicle at an altitude representative of boundary layer transition on the vehicle. Consider realistic transitional front asymmetries and vehicle angles of attack.
- 4) Determine the net forces and moments acting on the vehicle by integrating the pressures and shear stresses over the vehicle surface. Determine which boundary layer parameter(s) are the probable source of the vehicle motion disturbances occurring during boundary layer transition.

These studies are explained in detail in Section 2 of this report.

1.2 Boundary Layer Measurements - A Literature Survey

A review of both open and classified literature has been undertaken with the purpose of accumulating data on techniques for the measurement of boundary layer parameters on hypersonic reentry vehicles. The survey was corollary work to the studies outlined in Section 1.2 which examined the forces on the heatshield during reentry. The results showed that if asymmetrical transition were present, resultant forces caused trajectory errors. Insofar as measurements were concerned, two parameters were especially noted: 1) Transition asymmetry and 2) magnitude of gas pressure on the body which directly caused the body to be displaced or to be given an angular moment.

Having been provided with these guidelines, the measurement literature survey was initiated by selection of papers which reported on experiments, either ground or flight tests, in which boundary layer parameters were monitored. It was discovered that the sensors used were as varied as the boundary layer physical phenomena but that just a few techniques were applied by a majority of the investigators. Table I is a listing of boundary layer measurands along with the type of sensors used. Pressure, temperature/heating rate, and hot wires were observed to be in prominence in the literature.

The severe environment of an ICBM reentry eliminates the use of many of the sensors listed in Table I.

All techniques are applicable to wind tunnel tests as noted. Two primary techniques, hot wire anemometers and surface thin films are not very practical for flight tests due to the severe environment. Thin films can be used but are limited in altitude coverage if directly exposed to the flow.

Attempts have been made to use some of the more sophisticated techniques in flight tests; r.f. probes, interferometers, spectrometers, radiometers, and electrostatic probes were flown, but the equipment required tends to be bulky while results were not directly applicable to this study.

The best and most abundant data of transition phenomena were obtained with pressure, temperature, and heating rate transducers; therefore this report concentrates principal attention on these three methods.

TABLE I BOUNDARY LAYER MEASURANDS

<u>PARAMETER</u>	<u>MEASUREMENT TECHNIQUE</u>	<u>FLIGHT TESTS</u>	<u>WIND TUNNEL</u>
Static Pressure	Diaphragm Transducer	X	X
Pressure Fluctuations	Diaphragm Transducer, Piezo-electric Semiconductors	X	X
Surface Temperature	Thermocouples, RTD's*	X	X
Heating Rate (ΔT)	Thermocouples	X	X
Temperature Profile	Hot Wire, Thin Films		X
Thickness	Hot Wire Anemometer, Optical		X
Mass Flow Rate	Hot Wire		X
Velocity	Hot Wire		X
Density	Laser, Photography		X
Electron Density	Electrostatic Probe	X	X
Electrical Conductivity	RF Probes, Interferometers	X	X
Blowing Rate	Recession Rate Sensors	X	X
Friction Coefficients	Force Moment Balances		X
Optical Radiation	Spectrometer, Radiometer	X	X
Infrared Radiation	Spectrometer, Radiometer	X	X

* Resistive Temperature Detectors

In Section 3.0, detailed survey results are given for pressure and temperature with primary emphasis on the factors which cause errors. Section 4.0 contains conclusions and recommendations for future efforts in the measurement of transition. Section 5.0 contains the references and other reports reviewed which were found to have information pertinent to this survey.

2.0 BOUNDARY LAYER ANALYSIS

2.1 Baseline Vehicle Characteristics

The vehicle considered in this study was a state-of-the-art type vehicle consisting of a conical blunted cone with a 9-degree half-cone angle, a nose radius of 1.65 cm and a total vehicle length of 1.829 meters. The total vehicle weight at reentry was 771 kg and the vehicle possessed a nominal static margin of 5%. The heatshield was carbon phenolic on both the frustum and nosetip. The baseline trajectory consisted of a 10197 kilometer minimum energy trajectory with a 91.44 km altitude, reentry velocity of 7.163 km/sec and a flight path angle of 22 degrees below the local horizontal. Boundary layer transition was assumed to occur between 27.43 km and 21.34 km altitudes.

The reference trajectory used in the present study is shown in Figure 1. This trajectory was obtained from a three-degree of freedom point-mass simulation of the above vehicle reentering at the above described initial conditions. The variation of the aerodynamic drag characteristics of the vehicle with free stream Mach number and Reynolds number was considered for this calculation. The ballistic coefficient at 30.48 km altitude was 98155 N/m^2 , based upon inviscid drag only. High altitude viscous interaction, angle of attack effects and shape change effects are not included and are believed to be relatively insignificant.

2.2 Aerodynamic Heating

The aerodynamic heating on the vehicle was determined for the reference trajectory of Figure 1 using the ARROW code. The ARROW code was developed at Kaman and is capable of calculating the aerodynamic heating on a sphere-cone at zero angle of attack.

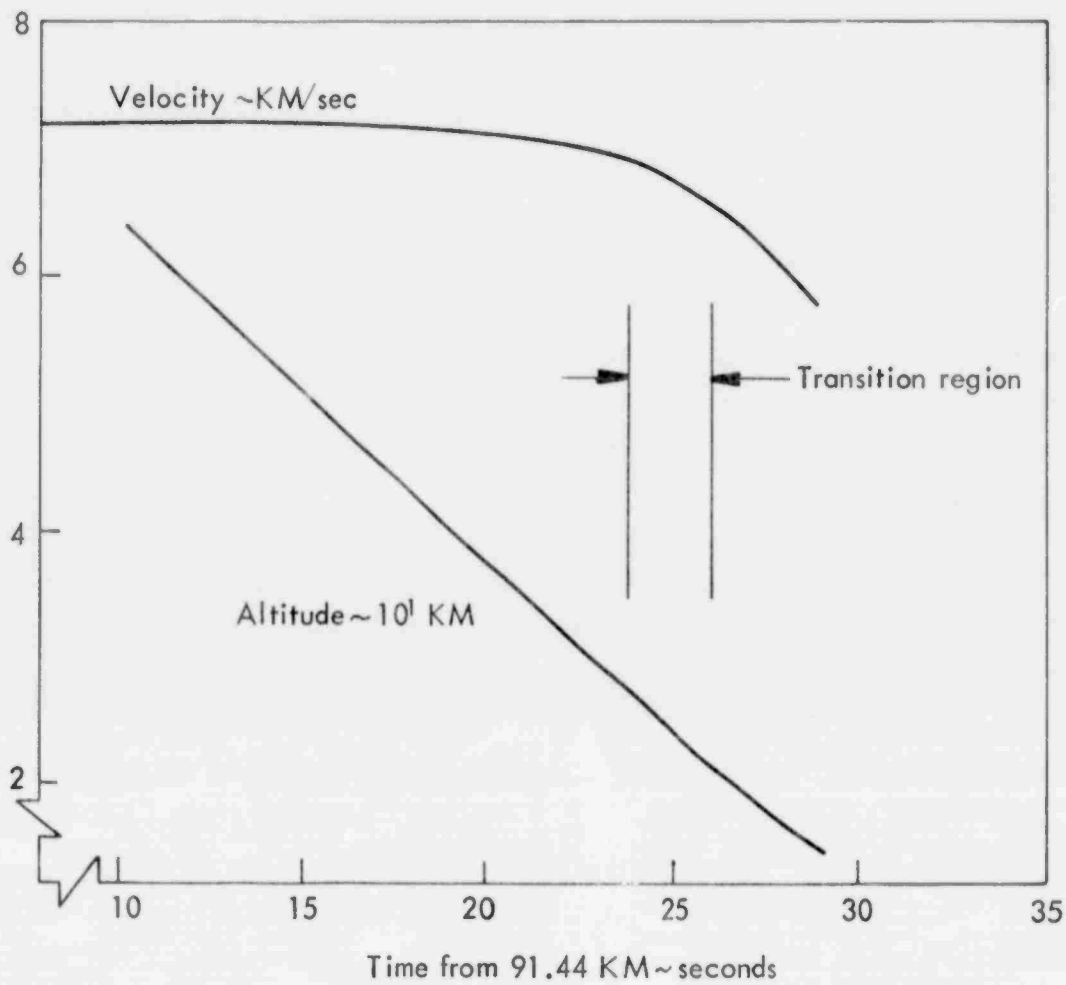


FIGURE 1 REFERENCE TRAJECTORY

The code uses general blunt body equations for both laminar and turbulent flow, accounts for nose bluntness effects on the pressure and entropy distribution along the edge of the boundary layer, and employs real gas thermodynamic and transport properties of air throughout.

The pressure distribution and shock shape are determined in ARROW through combined theoretical and empirical methods. Over the range of conditions of interest, the shock wave shape can be adequately approximated by the power law curve of Gregorek and Korkan (Reference 1) in the nose region, followed by a straight line at the sharp cone shock angle, i.e.,

$$R_S = R_N A \left(\frac{x}{R_N} + \frac{\Delta_n}{R_N} \right)^n (2)^{1-n} \quad \text{for } x \leq x_C \quad (1a)$$

where $A = 1.52 \epsilon_n^2 + \frac{1}{M_\infty^2}$

$$n = 0.44 + 0.76 \epsilon_n^2 + \frac{1}{2M_\infty^2}$$

and

$$R_S = R_C + (x - x_C) \tan \theta_C \quad \text{for } x > x_C \quad (1b)$$

Here θ_C is the sharp cone shock angle as computed from the correlations of Simon and Walters (Reference 2) and Δ_n is the bow shock standoff distance, given by Inouye (Reference 3) as

$$\frac{\Delta_n}{R_n} = 0.78 \epsilon_n \quad (2)$$

x_c denotes the match point between the two fits, i.e., the point where the slope of the power law fit is equal to $\tan\theta_c$. Once the local shock wave angle is known, the Rankine-Hugoniot equations in conjunction with a normal shock table can be used to find the entropy behind the shock.

The pressure coefficient distribution on the nose ($\phi < \phi_{tp}$) is obtained from a modification of Inouye's work (op. cit.)

$$\frac{C_p}{C_{p_{max}}} = 1 - \eta \sin^2 \phi + \nu \sin^4 \phi \quad (3)$$

where nominally $\eta = 1.25$ and $\nu = .302$. Back on the conical afterbody the pressure coefficient is determined by a modified version of the equation developed by Arne, et al (Reference 4)

$$\frac{C_p}{C_{p_c}} = 1 + \frac{.055}{1 + e^{11(\bar{x}-1.48)}} - .185 \frac{\bar{x}-.1}{\bar{x}^2+.00384} e^{-6.094(\bar{x}-.48)^2} \quad (4)$$

$$\text{where } \bar{x} = \frac{x}{R_N} \frac{C_{p_c}}{2}, \quad \bar{x} \geq .11.$$

This equation reflects the under-expansion on the cone caused by nose bluntness effects followed by a recompression to the sharp cone value C_{p_c} . The region between the tangent point and $\bar{x} = .11$ is then interpolated using a power law fit.

Once the pressure distribution and shock properties are known, it remains to determine the entropy distribution at the edge of the boundary layer. Because of the curved bow shock, the entropy varies from one streamline to another within the shock layer, i.e., an entropy gradient exists due to the presence of vorticity in the flow. Therefore, a mass balance technique

is used to define the appropriate streamline at the edge of the boundary layer for each point on the body.

$$\rho_{\infty} u_{\infty} \pi R_s^2 = 2\pi r \rho_e u_e (\delta - \delta^*).$$

An isentropic expansion is then taken along this streamline to the body pressure so that all properties at the edge of the boundary layer can then be computed.

The laminar boundary layer equations are modified versions of Lees' (Reference 5) local similarity analysis

$$\dot{q} = \frac{.332C}{(\text{Pr}^*)^{2/3}} \frac{\rho^* \mu^* u_e r}{(\tilde{S})^{1/2}} (h_r - h_w) \quad (5a)$$

$$\tau = .332C \frac{\rho^* \mu^* u_e^2 r}{(\tilde{S})^{1/2}} \quad (5b)$$

$$\theta = .664 \frac{(\tilde{S})^{1/2}}{\rho_e u_e r} \quad (5c)$$

where $S = \int_0^S \rho^* \mu^* u_e r^2 ds$

$$h_r = h_e + \sqrt{\text{Pr}^*} \frac{u_e^2}{2}$$

$$C = 1 + .205 \sqrt{\beta}$$

$$\beta = 2 \frac{d \ln u_e}{d \ln \tilde{S}}$$

Here the * denotes that the properties are evaluated at Eckert's reference enthalpy h^*

$$h^* = .22h_r + .28h_e + .50h_w \quad (6)$$

C is a correction factor to account for non-zero pressure gradient effects on the Blasius non-dimensional enthalpy gradient at the wall ($.332 Pr^{1/3}$). Values of δ and δ^* as a function of θ and other flow parameters are obtained from the work of Walker (Reference 6).

The turbulent boundary layer equations are modified versions of Walker's (Reference 7) particular solution of the momentum and integral equations.

$$\dot{q} = \frac{.0296C}{(Pr^*)^{2/3}} \frac{\rho^* \mu^{*.25} u_e r^{.25}}{(\tilde{S}_q)^{.2}} (h_r - h_w) \quad (7a)$$

$$\tau = .0296C \frac{\rho^* \mu^{*.25} u_e^{2.25+2.25H} r^{.25}}{(\tilde{S}_\theta)^{.2}} \quad (7b)$$

$$\theta = .037 \frac{(\tilde{S}_\theta)^{.8}}{\rho_e u_e^{2+H} r} \quad (7c)$$

where $\tilde{S}_q = \int_0^S \rho^* \mu^{*.25} u_e r^{1.25} ds$

$$\tilde{S}_\theta = \int_0^S \rho^* \mu^{*.25} u_e^{2.25+1.25H} r^{1.25} ds$$

$$h_r = h_e + P_r^{1/3} \frac{u_e^2}{2}$$

$$C = \begin{cases} 1 & \text{for } R_e^* < 2.52 \times 10^7 \\ .31 (R_e^*)^{.069} & \text{for } R_e^* > 2.52 \times 10^7 \end{cases}$$

Here, the * denotes that the properties are evaluated at Eckert's reference enthalpy, C is a correction factor to account for the fact that the Blasius flat-plate skin friction values are valid only below a Reynold's number of roughly 10^7 , and H is the boundary layer form factor. These equations assume fully developed turbulent flow over a smooth surface with a virtual origin at the stagnation point. Values of δ and δ^* as a function of θ and other parameters are obtained from the work of Walker and Schumann (Reference 8).

The above equations are solved in a step-by-step fashion, starting at the stagnation point and working back on the body. An iteration on the entropy is performed at each body point until the mass balance is satisfied. Thermodynamic properties of air are calculated using the NASA Ames real gas tables (Reference 3). The viscosity of air is based on Sutherland's equation for temperatures less than 3333°K , and a curve fit to Hansen's (Reference 9) data at higher temperatures. The Prandtl number is taken as constant at $P_r = 0.72$.

Calculations of the aerodynamic heating rates to the reference vehicle were obtained using the ARROW code and the reference trajectory of Figure 1. The heating rate histories at the stagnation point, sphere-cone tangency point and rearward-most cone station are shown in Figure 2. These calculations are based upon an assumed wall temperature of 2778°K . The heating rates shown in Figure 2 are laminar heating rates except for the

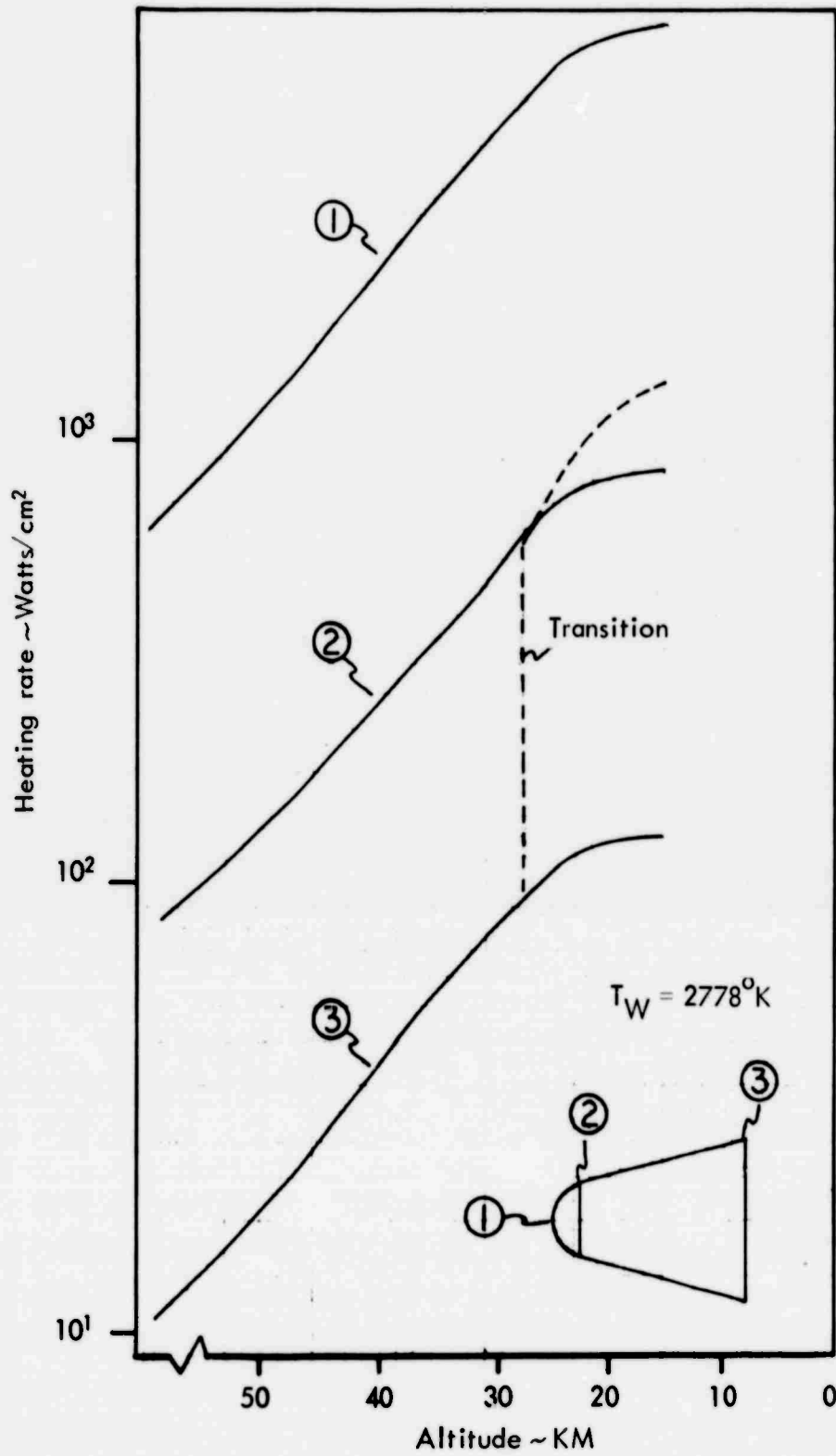


FIGURE 2 REFERENCE VEHICLE AERODYNAMIC HEATING RATES

rearward-most cone station where transition to turbulent flow at 27.43 km altitude is depicted with the dashed line. The increased heating due to turbulent flow at 27.43 km is significant, being approximately a sevenfold increase.

The heating rate distributions over the body for both laminar and turbulent flow at 24.38 km altitude are shown in Figure 3. Once again, these calculations are for an assumed wall temperature of 2778°K and the turbulent boundary layer has an assumed virtual origin at the stagnation point of the vehicle.

2.3 Heatshield Ablation Response

As mentioned above, the ARROW code solutions provided a description of the aerodynamic heating environment of the reference vehicle for the reference trajectory represented by an entry velocity of 7.163 km/sec and an entry angle of -22 degrees at an altitude of 91.44 km. The ARROW output was also utilized as input to the REKAP code to determine the ablation response of the carbon phenolic heatshield. The REKAP reaction kinetics ablation program is a one-dimensional transient thermal conduction in-depth pyrolysis and surface ablation computer program. The in-depth pyrolysis reactions are modeled by Arrhenius rate expressions and the surface ablation can be represented by either an equilibrium diffusion controlled or vaporization-controlled reaction.

When a typical inorganic-reinforced plastic such as carbon phenolic is subjected to atmospheric reentry at hypersonic velocity, a complex process known as ablation occurs which sacrifices the outer layer of material while protecting the bulk of the material from thermal damage. The initial response of the heatshield material to the reentry thermal pulse is the decomposition of the thermosetting phenolic resin, with the

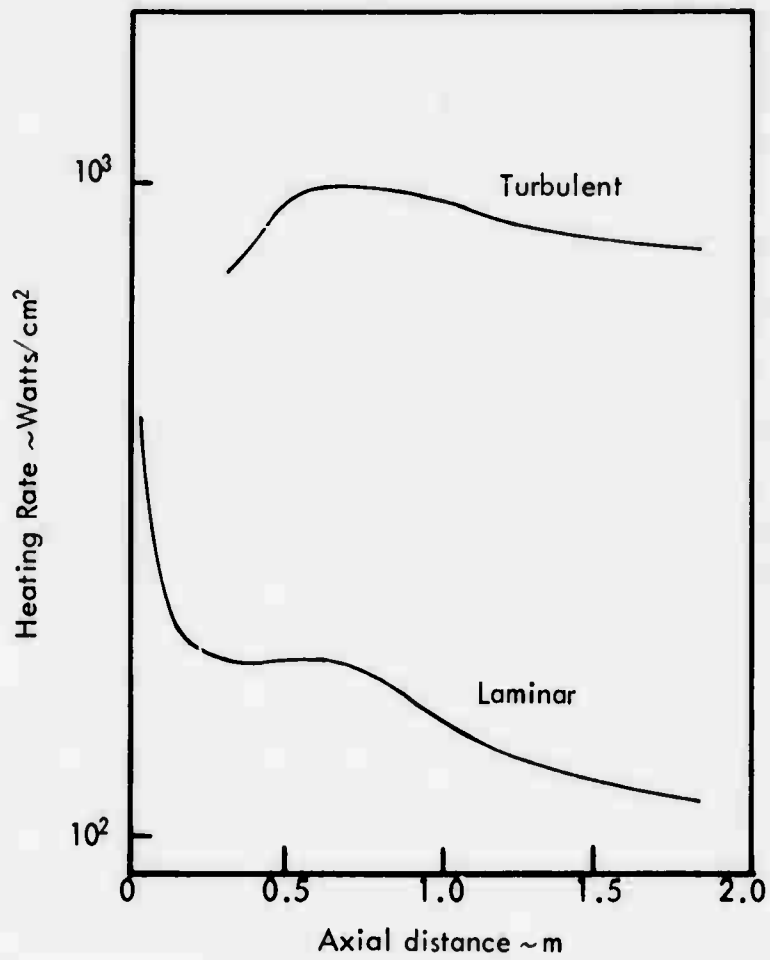


FIGURE 3 REFERENCE VEHICLE AERODYNAMIC HEATING DISTRIBUTIONS AT 24.384 KM ALTITUDE

resin pyrolyzed to a mixture of light gases and carbonaceous materials, or char layer. As the surface temperature of the char layer increases, it begins to react with oxygen in the boundary layer. Below approximately 1000°K, the carbon-oxygen reaction is kinetically controlled, being dependent solely upon the forward reaction rate of carbon and oxygen. Above approximately 1000°K, the carbon-oxygen reaction is limited by the diffusion of oxygen across the boundary layer. At very high temperatures, carbon undergoes sublimation/vaporization with free carbon given off, in addition to undergoing diffusion controlled oxygen and cyano reactions. The success of the ablation mechanism is dependent upon forming high char layer surface temperatures to reradiate the incoming heat plus the availability of high heats of pyrolysis in the thermosetting resin.

The REKAP ablation program is basically a transient, one-dimensional thermal conduction solution through a heatshield material containing a temperature-sensitive in-depth reaction. The conservation of energy within the heatshield is given by

$$\rho C_p \left[\frac{\partial T}{\partial t} + \bar{v} \cdot \nabla T \right] = \nabla \cdot (K \nabla T) - \sum \dot{w}_j h_j \quad (8)$$

where the term w_j represents the mass rate of production of species j by chemical reaction per unit volume per unit time, h_j is the enthalpy of species j including chemical, and \bar{v} is the ablation rate. This equation is the normal diffusion equation with the addition of the chemical source term $\sum \dot{w}_j h_j$ plus the term $\bar{v} \cdot \nabla T$ resulting from the use of a moving frame of reference. The chemical source terms are combined into a single gas production term \dot{w}_{gas} and the thermal degradation process

of the plastic can be represented by a second-order Arrhenius type rate controlled reaction over a large temperature range as follows

$$\dot{w}_{\text{gas}} = \rho_{\text{vp}} \left(\frac{\rho_{\text{p}} - \rho_{\text{c}}}{\rho_{\text{vp}}} \right)^2 \sum_i B_i e^{-E_i/RT} \quad (9)$$

where, for carbon phenolic

$$\begin{aligned} \rho_{\text{vp}} &= 1454 \text{ kg/m}^3 \\ \rho_{\text{c}} &= 1185 \text{ kg/m}^3 \\ B_1 &= 83.4 \text{ sec}^{-1} \\ B_2 &= 1.011 \times 10^6 \text{ sec}^{-1} \\ E_1 &= 12058 \text{ joules/gm}\cdot\text{mole} \\ E_2 &= 26796 \text{ joules/gm}\cdot\text{mole} \end{aligned}$$

An energy balance at the surface of the char layer provides the heat flux boundary condition for the numerical solution. The net conductive heat flux to the char layer is given by

$$-K \frac{\partial T}{\partial t} = (C_{\text{H}_2\text{O}} \rho_e u_e - \dot{m}_w \eta) (H_e - H_w) - \dot{m}_w (H_w - h_s) - \epsilon \sigma T_w^4 \quad (10)$$

where η is the transpiration blockage coefficient, assumed to be 0.77 for laminar flow and 0.30 for turbulent flow. The surface emissivity ϵ for a carbon phenolic char is assumed to be 0.85.

The mass transfer rate at the wall \dot{m}_w can be determined for the case of diffusion controlled oxidation by employing the relationship between heat and mass transfer in a laminar

boundary layer for unit Prandtl, Lewis and Schmidt numbers as proposed by Lees (Reference 10)

$$\frac{\tilde{K}_{oe}}{\tilde{K}_{ow}} = \frac{\dot{m}_w}{\rho_e u_e C_{H_0}} + 1 \quad (11)$$

where \tilde{K}_{oe} is the mass fraction of oxygen at the edge of the boundary layer (for air, $\tilde{K}_{oe} = 0.2314$) and \tilde{K}_{ow} is the mass fraction of oxygen at the wall. For the diffusion limited oxidation, all of the oxygen at the wall appears in the form of CO and

$$\dot{m}_w = 0.1734 \rho_e u_e C_{H_0} \quad (12)$$

As the surface temperature rises to above approximately 5000°R, the vaporization rate of atomic and molecular carbon species, such as C, C₂, C₃, C₄ and C₅, all increase exponentially. In addition, homogeneous and heterogeneous chemical reactions involving nitrogen and carbon begin to appear and form cyanogen (CN)₂ and the cyano radical CN. The REKAP mass transfer rates for a carbon surface undergoing combined vaporization and diffusion controlled oxygen and cyano reactions are based upon the work of Scala and Gilbert (Reference 11) for a nine component gas model using O, O₂, N, N₂, CO, CO₂, C, C₃ and CN, with updating of the transport and thermodynamic properties by Fogaroli and Brant (Reference 12). Figure 4 shows the variation of the normalized mass loss in the diffusion controlled oxidation and vaporization regimes as a function of surface temperature and pressure. The normalizing factor is the diffusion controlled oxidation mass transfer rate.

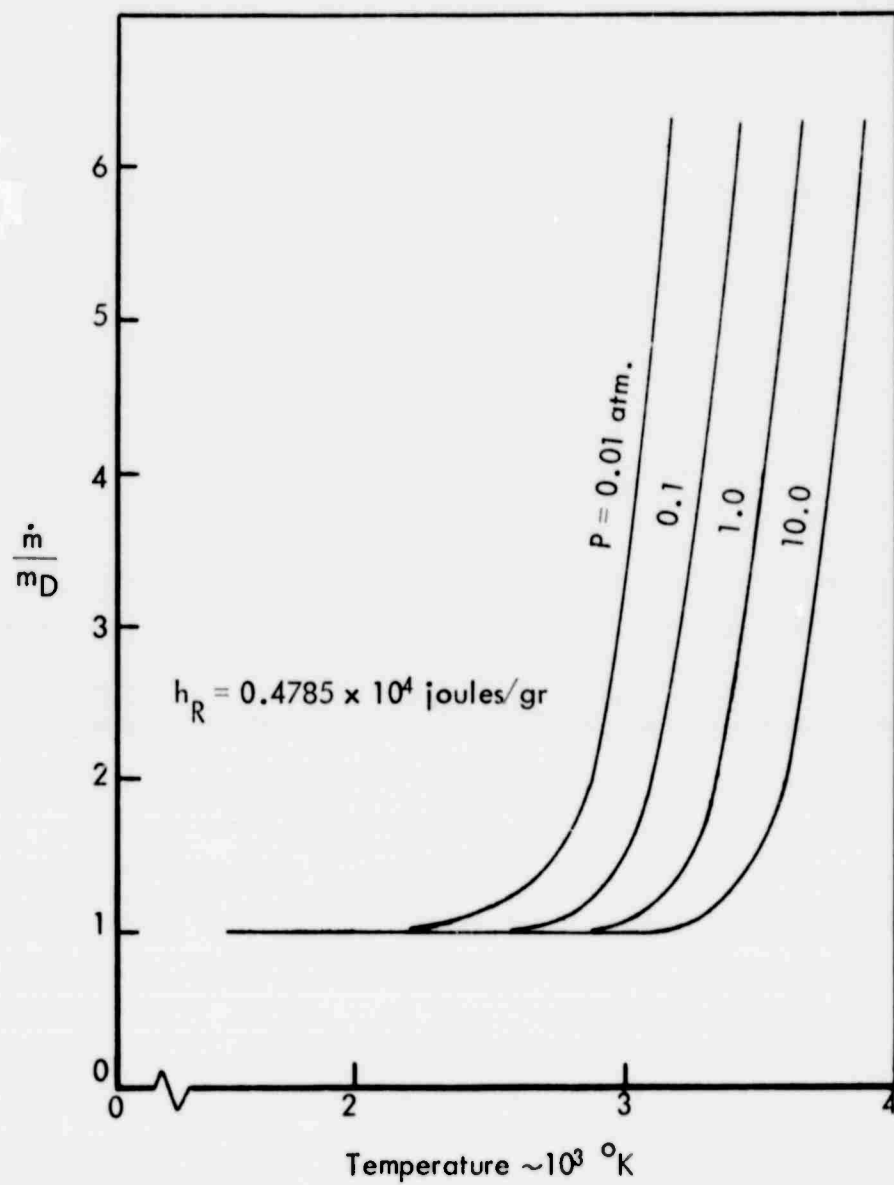


FIGURE 4 NORMALIZED CARBON MASS LOSS IN AIR

Using the above-defined set of equations to describe the transient heat conduction, in-depth pyrolysis reactions and surface energy and mass balances, the REKAP reaction kinetics ablation program solves the transient heat conduction equation by stable, explicit finite-difference equations. The thermal conductivity and specific heat of the carbon phenolic ablator are assumed to vary with temperature as shown in Figure 5. The ablator thickness was assumed to be 1.041-cm thick and was integrally attached to a 0.152-cm thick aluminum substructure with a .076-cm thick EA 934 adhesive layer. The effects of having an underlying substrate attached to the carbon phenolic were virtually insignificant since temperature rises in the substrate at the time of transition were 1-2 degrees K. As mentioned above, the ARROW heat transfer coefficient and recovery enthalpy distributions over the reference vehicle during reentry were employed by the REKAP program to determine the heatshield ablation response.

The results of the REKAP ablation analysis are shown in Figures 6 and 7 where the surface temperature and mass transfer rate histories at three body stations are shown. Surface temperatures are in the 1100-1400°K range during laminar flow and jump to approximately 3050°K within 2 seconds following boundary layer transition. Mass transfer rates shown approximately a six-to-eight fold increase due to boundary layer transition. At the 1.27-meter axial station on the body, the mass transfer rate increases from .044 to .29 kg/m²sec for boundary layer transition at 24.38 km. In terms of the free stream mass flux $\rho_{\infty}u_{\infty}$, the normalized blowing rates at the 1.27-meter station for laminar and turbulent flow would be .00014 and .00094, respectively.

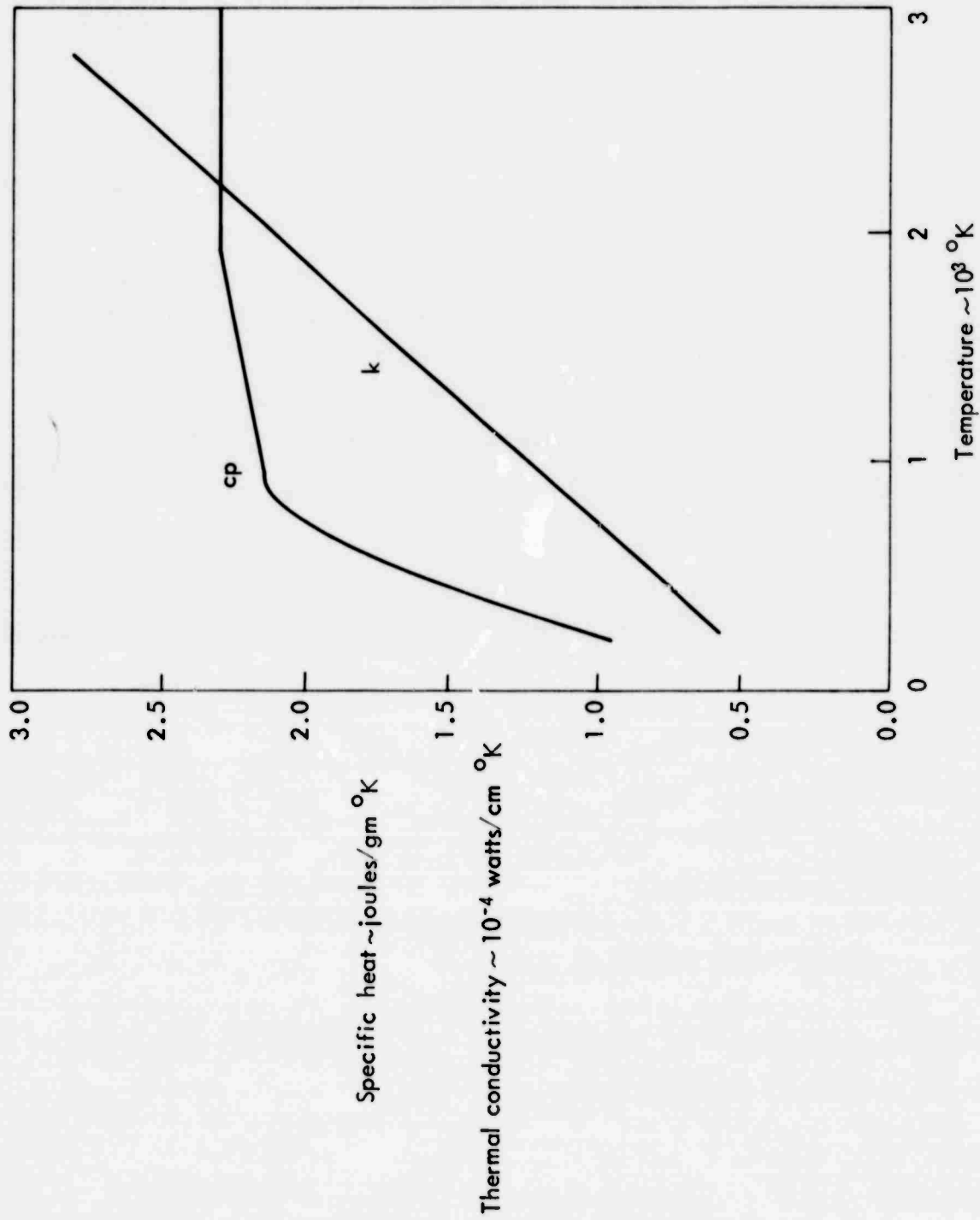


FIGURE 5 THERMAL PROPERTIES OF CARBON PHENOLIC CHAR

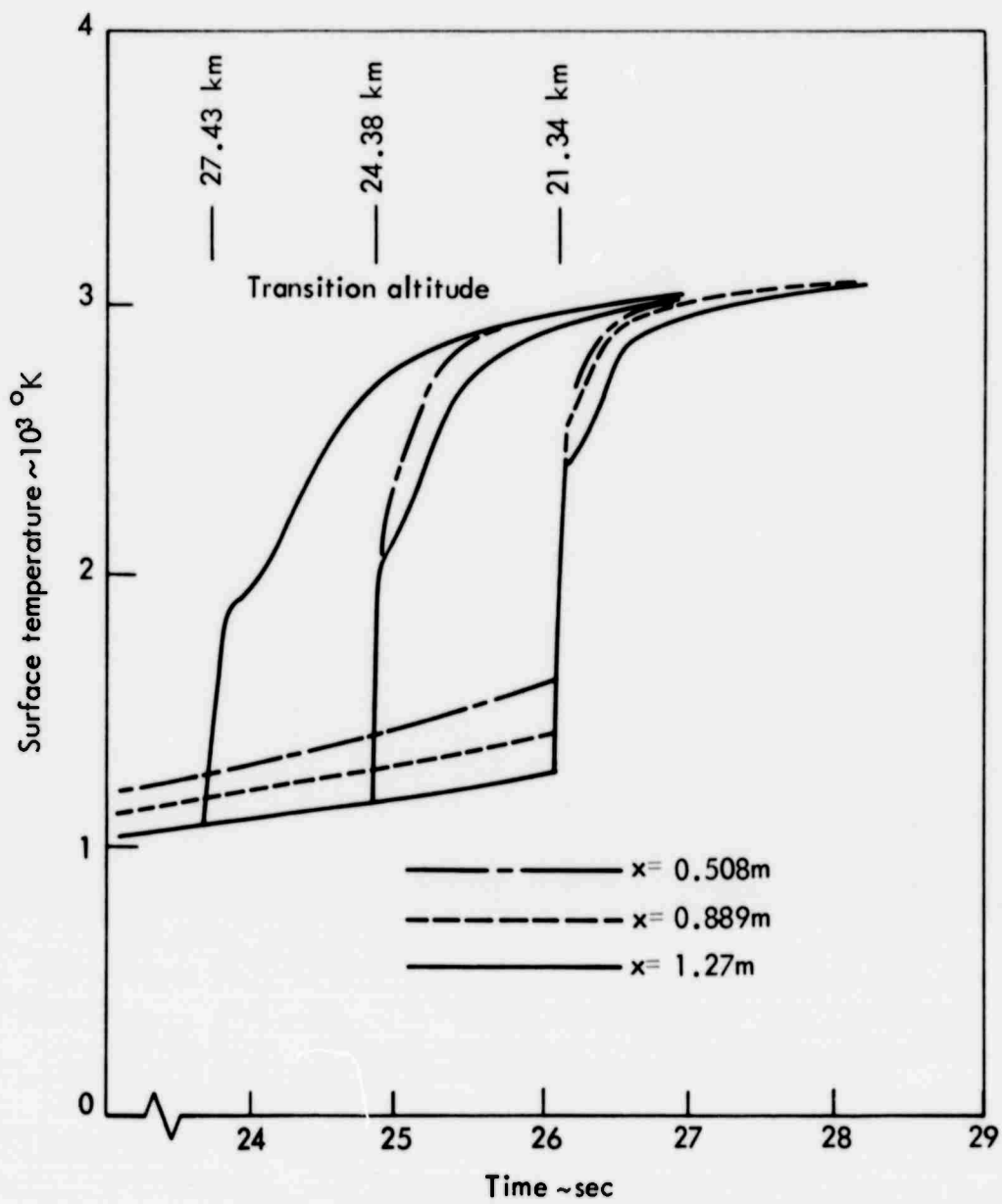


FIGURE 6 REFERENCE VEHICLE SURFACE TEMPERATURE HISTORIES

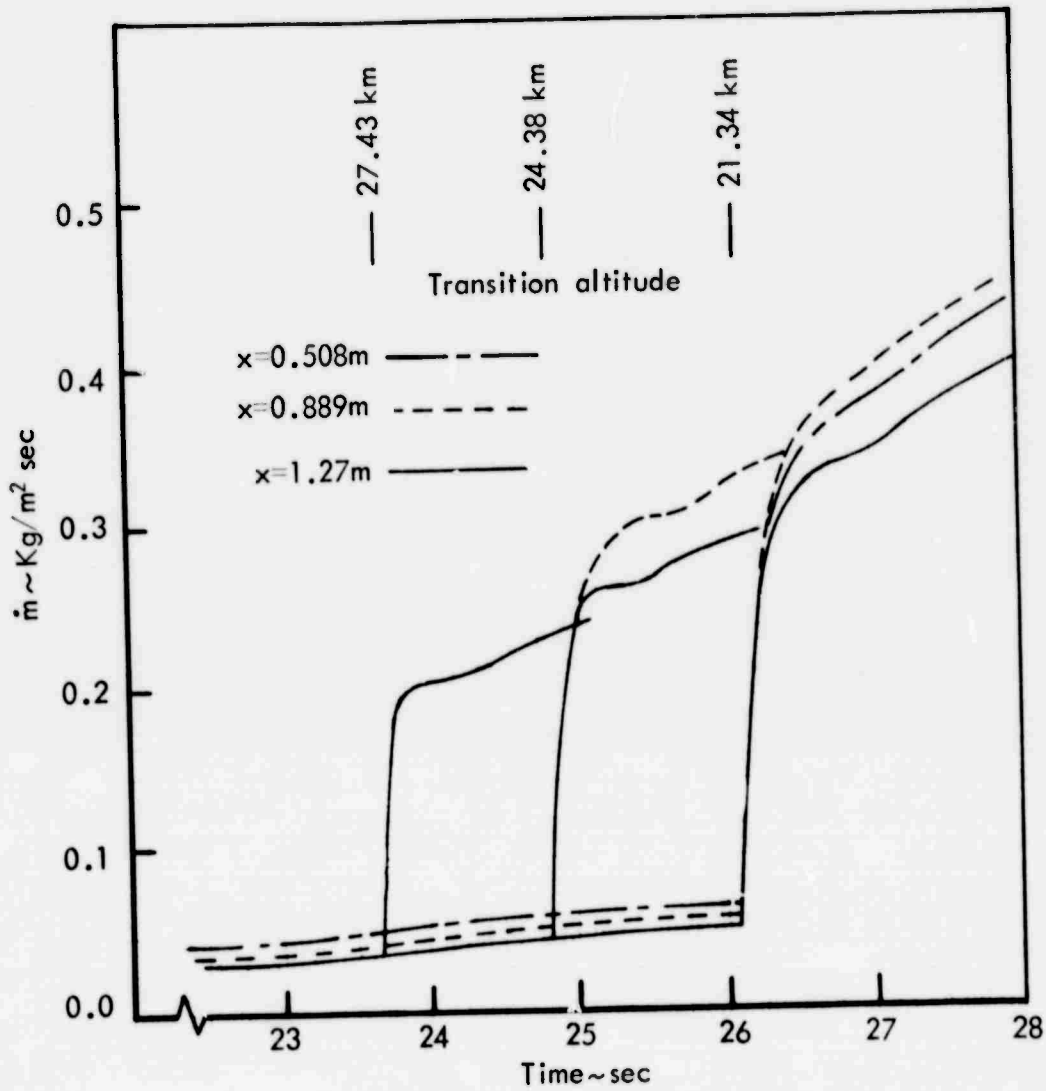


FIGURE 7 REFERENCE VEHICLE SURFACE MASS LOSS HISTORIES

2.4 Viscous and Inviscid Flow Fields

Critical to the work being reported on here is the postulated asymmetric transition which occurs during hypersonic reentry of conical shaped vehicles. The degree of asymmetry is not well understood except for some evidence derived from ground tests which indicates a preference for transition to first occur on the leeward side of conical shapes at angle of attack. Additionally, asymmetric surface roughness or manufacturing irregularities may be the source of the postulated boundary layer asymmetry. The objective of the work contained in this report is not to investigate the source or the degree of asymmetry which may be present during boundary layer transition, but instead to begin with the premise that an asymmetry exists and to attempt to discover those parameters associated with transitional boundary layers which are producing the excursions in the vehicle motion commonly observed during transition.

We will attempt to characterize the laminar and transitional hypersonic boundary layer on the reference vehicle at a single altitude of 24.38 km and a single velocity of 6.870 km/sec. Both non-zero and zero incidence angles will be considered. The influence of wall mass transfer associated with the ablation of the carbon phenolic heatshield will be investigated. Significant limitations in the analytical techniques will be pointed out where appropriate and recommendations for further study will be mentioned.

2.4.1 Zero Angle of Attack Analysis

Zero angle of attack viscous flow field calculations for the reference vehicle at the 24.38 km altitude flight condition were obtained using the LTBLCEQL (Laminar and Turbulent Boundary Layer with Chemical Equilibrium) computer code (Reference 13). This computer code solves the compressible boundary layer equations for two

dimensional or axisymmetric flows of either perfect gases or reacting gases in chemical equilibrium. The equations of motion are cast in non-dimensional form using the Levy-Lees variables and reduced to ordinary differential equations. The resulting parabolic differential equations are solved using finite difference techniques.

The governing equations for compressible boundary layer flows contain the normal eddy viscosity and eddy conductivity transport terms in both the momentum and energy equations, respectively. By merely setting the eddy viscosity and eddy conductivity terms equal to zero, nonsimilar laminar boundary flows may be computed. Options are available for calculating either instantaneous transition from laminar to turbulent flow or transition over a prescribed distance. The effects of wall mass transfer are included with injectant gases of either air, helium, carbon dioxide and argon. Boundary conditions consist of specification of the wall temperature and wall mass transfer distributions, the free stream conditions and the boundary layer edge pressure and entropy. The actual boundary layer edge entropy is solved for within the computer code using an input radial entropy distribution and streamline tracking techniques. The boundary layer edge pressure is normally determined from a separate inviscid flow field solution, as is the radial entropy distribution.

Defining the turbulent shear and the turbulent flux of total enthalpy in terms of eddy viscosity and eddy conductivity analogies, the governing equations for compressible laminar or turbulent two-dimensional or axisymmetric boundary layer flows can be written as

Continuity

$$\frac{\partial(\rho u r^j)}{\partial x} + \frac{\partial[(\rho v + \overline{\rho'v'})r^j]}{\partial y} = 0 \quad (13)$$

Momentum

$$\rho u \frac{\partial u}{\partial x} + (\rho v + \overline{\rho'v'}) \frac{\partial u}{\partial y} = \rho_e u_e \frac{du_e}{dx} + \frac{\partial}{\partial y} \left[\mu \frac{\partial u}{\partial y} + \rho \epsilon \frac{\partial u}{\partial y} \right] \quad (14)$$

Energy

$$\rho u \frac{\partial H}{\partial x} + (\rho v + \overline{\rho'v'}) \frac{\partial H}{\partial y} = \frac{\partial}{\partial y} \left[\frac{\mu}{P_r} \frac{\partial H}{\partial y} + \frac{\rho C_p}{P_r} \epsilon_K \frac{\partial H}{\partial y} + \mu \left(1 - \frac{1}{P_r} \right) \right] \quad (15)$$

Species

$$\rho u \frac{\partial C_i}{\partial x} + \rho v \frac{\partial C_i}{\partial y} = - \frac{\partial J_i}{\partial y} \quad (16)$$

where $j = 0$ for two dimensional flow

$j = 1$ for axisymmetric flow

The boundary layer equations are transformed by the Levy-Lees transformation equations

$$d\xi = \rho_e u_e \mu_e r^{2j} dx \quad (17a)$$

and
$$d\eta = \frac{\rho_e u_e r^j}{(2\xi)^{1/2}} \frac{\rho}{\rho_e} dy \quad (17b)$$

With the aid of the definitions

$$f' = u/u_e \quad (18a)$$

$$f = \int f' d\eta \quad (18b)$$

the continuity equation may be written as:

$$V_{\eta} = 2\xi f' \xi - f' \quad (19a)$$

where

$$v = \frac{2\xi}{\rho_e u_e \mu_e r^{2j}} \left[f' \eta_x + \frac{(\rho v + \overline{\rho' v'}) r^j}{(2\xi)^{1/2}} \right] \quad (19b)$$

With the further definitions

$$\begin{aligned} F &= f' \\ g &= H/H_e \\ C &= \rho \mu / \rho_e \mu_e \\ \epsilon^+ &= \epsilon / \nu \end{aligned} \quad (20)$$

and

$$\beta = \frac{2\xi}{u_e} \frac{du_e}{d\xi}$$

the energy and momentum equations can be written in the following standard form

$$\phi'' + A_1 \phi' + A_2 \phi + A_3 + A_4 \phi_{\xi} = 0 \quad (21)$$

where the prime superscripts denote differentiation with respect to η and the ξ subscript denotes differentiation with respect to ξ .

For the momentum equation, $\phi = F$ and the coefficients are given by the following equations:

$$\begin{aligned} A_1 &= \frac{C'}{C} + \frac{\overline{A}'_0}{\overline{A}_0} - \frac{v}{\overline{A}_0} \\ A_2 &= \beta F / \overline{A}_0 \\ A_3 &= \beta \rho_e / \rho \overline{A}_0 \end{aligned} \quad (22)$$

$$A_4 = -2\xi F/A_0$$

$$A_0 = C(1+\epsilon^+)$$

$$\bar{A}_0 = A_0/C$$

For the energy equation, $\phi = g = H/H_e$, and the coefficients are given by the following equations:

$$A_1 = \frac{C'}{C} + \frac{\bar{A}'_0}{\bar{A}_0} - \frac{V}{A_0}$$

$$A_2 = 0$$

$$A_3 = \frac{u_e^2}{H_e} \left(1 - \frac{1}{P_r}\right) \left[\frac{C'}{C\bar{A}_0} FF' + \frac{F'^2}{\bar{A}_0} + \frac{FF''}{\bar{A}_0} \right] \quad (23)$$

$$A_4 = -2\xi F/A_0$$

$$A_0 = \frac{C}{P_r} \left(1 + \epsilon^+ \frac{P_r}{P_{rt}}\right)$$

and $\bar{A}_0 = A_0/C.$

The above equations are constrained by the boundary conditions at the wall, $\eta = 0$, and at the outer edge of the boundary layer, $\eta = \eta_e$. The boundary conditions are

$$\text{at } \eta = 0: \quad F = 0, \quad g = \frac{H_w}{H_e} = \frac{h_w}{H_e}; \quad V = V_w$$

$$\text{at } \eta = \eta_e: \quad F = 1; \quad g = 1.$$

Two boundary layer transition models are available in the LTBLCEQL computer code. The first transition model changes the flow instantaneously from laminar to turbulent flow at a specified location on the body. Heat transfer results obtained with this model show a much steeper rise during transition than occurs in experimental data. On this basis, the instantaneous transition model is not completely satisfactory.

The second transition model provides for a regime of transition between laminar and turbulent flow. The calculation is started with the flow laminar and the eddy viscosity equal to zero. At a specified location (the beginning of transition) the turbulent eddy viscosity is gradually undamped until it reaches its fully turbulent value at some prescribed distance downstream (the beginning of fully turbulent flow). The undamping parameter used for the eddy viscosity is referred to as the transition intermittency factor given by

$$\Gamma = 1 - \exp(-A\bar{\xi}^2) \quad (24)$$

where $A = 0.412$

$$\bar{\xi} = \frac{x - x_0}{\lambda}$$

and $\lambda = \frac{x_f - x_0}{4}$

The distances x_0 and x_f refer to the starting and ending positions of boundary layer transition.

For turbulent and transitional flows, the Reynolds shear term is given by an eddy viscosity. The eddy viscosity, ϵ , is evaluated using the concept of a two layer eddy viscosity model consisting of an inner law, ϵ_i , valid near the wall and an outer law, ϵ_o , for the remainder of the boundary layer. The inner eddy viscosity law is based on Prandtl's mixing length concept expressed as

$$(\rho'v')u' = \rho\ell^2 \left(\frac{du}{dy}\right)^2 = \rho\epsilon_i \frac{du}{dy} \quad (25)$$

where ℓ is the mixing length. Prandtl proposed that this length will, in its simplest form, be related to the distance from the wall, at least in the region of development of turbulence. His proposition that

$$\frac{d\ell}{dy} = \text{constant} \quad (26)$$

has been tested under a variety of conditions and found to be quite adequate in the fully turbulent portion of the wall region. Van Driest (Reference 14) has provided a modification to Prandtl's mixing length hypothesis to allow for damping of the Reynolds shear stress near the wall. The expression given by Van Driest is

$$\ell = Ky(1 - e^{y/A}) \quad (27)$$

where $A = 26\nu / \sqrt{\frac{\tau_w}{\rho}}$

This expression is modified further for the case of mass transfer at the wall, where the damping term A becomes

$$A = 26\nu \left(\exp(-v_w / \sqrt{\tau_w/\rho}) / \sqrt{\tau_w/\rho} \right) \quad (28)$$

The outer eddy viscosity law is based upon the work of Clauser in combination with the Klebanoff intermittency factor and is expressed as

$$\epsilon_o = K u_e \delta_i^* \gamma \quad (29)$$

where δ_1^* is the incompressible boundary layer displacement thickness

$$\delta_1^* = \int_0^{\infty} \left(1 - \frac{u}{u_e}\right) dy \quad (30)$$

and γ is Klebanoff's intermittency factor

$$\gamma = \left[1 + 5.5 \left(\frac{y}{\delta}\right)^6\right]^{-1} \quad (31)$$

Numerically, the inner eddy viscosity increases with increasing distance away from the wall until it exceeds the outer eddy viscosity. This crossover point is monitored within the code and is used to define the limits of the inner and outer turbulent boundary layer regions.

With the boundary layer equations written in the standard form shown in Equation (21), solutions are obtained using a three-point, finite difference method. The solution procedure may be fully implicit or fully explicit. The implicit method of Crank-Nicolson has proved to be most satisfactory. The finite difference solution procedure has been developed for a variable spacing of the nodal points in the normal η coordinate direction. This permits a close spacing of points in the region near the wall where the variation of fluid and dynamic properties is greatest.

The LTBLCEQL computer code requires the specification of a number of boundary conditions before a solution can be obtained. As mentioned before, the REKAP analysis supplied information regarding the surface temperatures and pyrolysis and char gas mass transfer rates for laminar and turbulent boundary layer heating. In addition to this, boundary layer edge properties are required.

The LTBLCEQL computer code relies on the assumption that the inviscid and viscous flow fields are uncoupled and that inviscid solutions can be used for the specification of edge of boundary layer pressure and entropy distribution. This assumption is valid as long as the boundary layer displacement thickness is small in comparison to the shock layer thickness, providing that an entropy entrainment type analysis is used. We will proceed with the approach that the inviscid and viscous flow fields are uncoupled and employ an axisymmetric method of characteristics solution to obtain the inviscid flow field properties. The validity of the uncoupled approach will be re-examined upon completion of the boundary layer analysis.

The inviscid pressure and entropy distributions for the zero angle of attack viscous flow field cases were determined using the NASA real gas method of characteristics solution developed by Inouye, Rakich and Lomax (Reference 15). The axial pressure distribution and radial entropy distribution are shown in Figures 8 and 9. Note the pressure over-expansion and re-compression caused by the nose bluntness of the body. The radial entropy distribution is converted to a body surface distribution within the LTBLCEQL code using an iterative solution of the entropy swallowing by tracking streamlines from the shock crossing point to the boundary layer edge using a boundary layer-shock layer mass balance.

Using the boundary layer code conditions given by the method of characteristics solution and the wall temperature and wall mass transfer distributions given by the REKAP solutions, viscous flow fields were obtained with the LTBLCEQL computer code for four different boundary layer flows. They were:

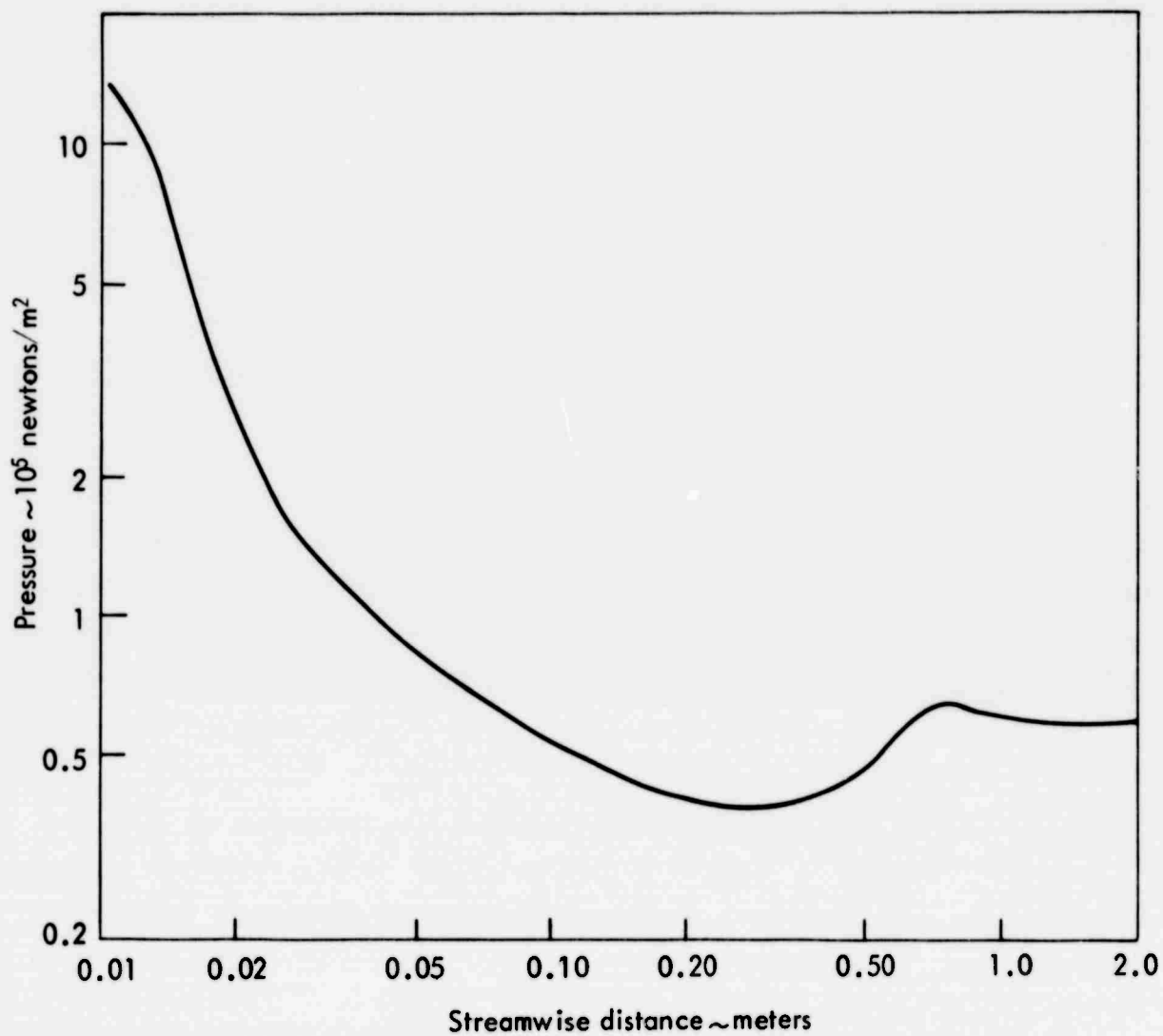


FIGURE 8 STREAMWISE PRESSURE DISTRIBUTION ZERO ANGLE OF ATTACK

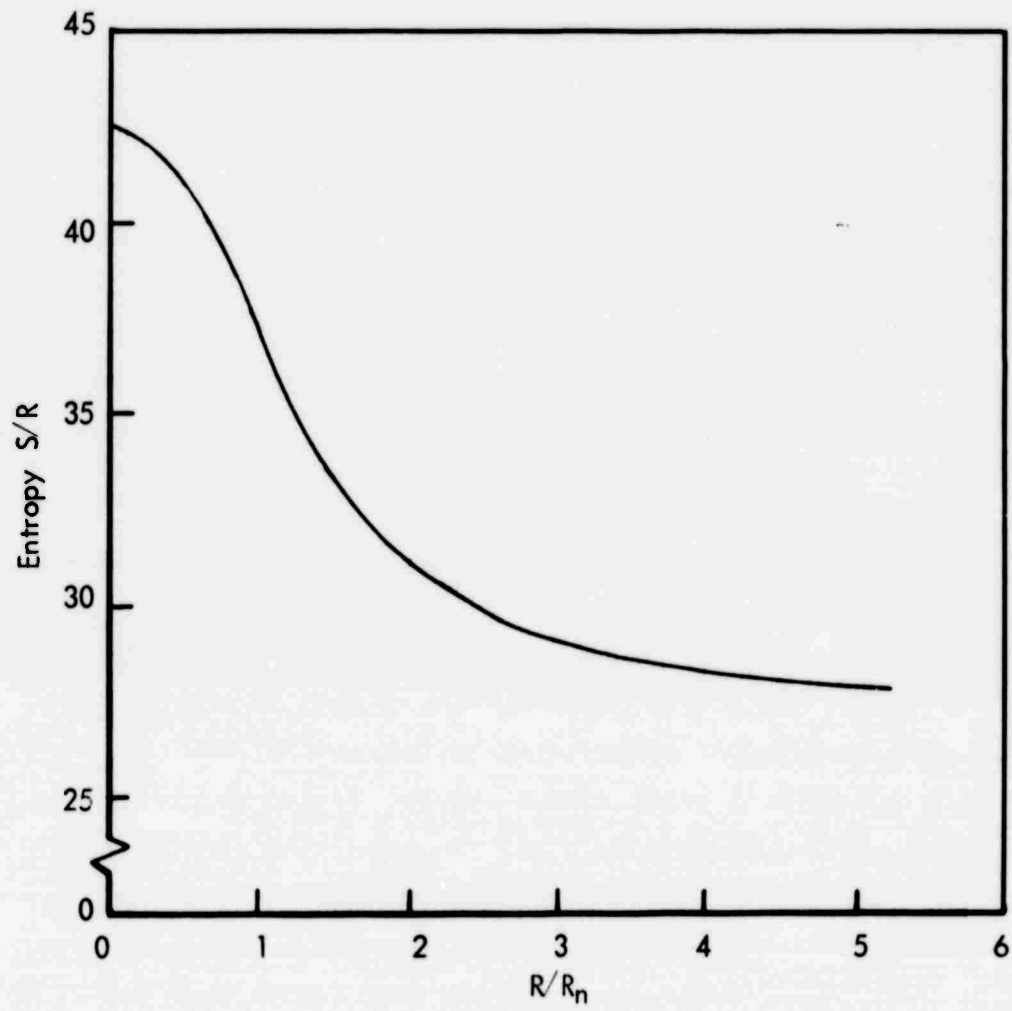


FIGURE 9 RADIAL ENTROPY DISTRIBUTION, ZERO ANGLE OF ATTACK

- 1) Fully laminar with wall mass transfer
- 2) Fully laminar without wall mass transfer
- 3) Transitional with wall mass transfer
- 4) Transitional without wall mass transfer.

For the transitional boundary layer flow calculations, transition was assumed to begin at an axial length of .61 meters and end at an axial length of 1.22 meter, thereby dividing the vehicle length into a forward one-third region with laminar flow, a middle one-third region with transitional flow and a rearward one-third region with fully developed turbulent flow. The selection of a transitional boundary layer pattern described above coupled with a fully laminar pattern represented an attempt to bound the problem of asymmetrical transition on the vehicle.

The wall mass transfer rates and wall temperature distributions were determined from the REKAP analysis described in Section 2.3. The choice of the wall mass transfer rates and wall temperature distributions during transitional and turbulent boundary layer heating was somewhat arbitrary since the actual values are dependent on both the boundary layer state and the time duration of the boundary layer state. The actual wall temperatures and wall mass transfer rates used for both the laminar and transitional LTBLCEQL solutions are shown in Figures 10 and 11. Air was chosen to simulate the injectant gas. The high surface temperatures and mass transfer rates associated with the nose tip environment were not simulated in the LTBLCEQL calculations.

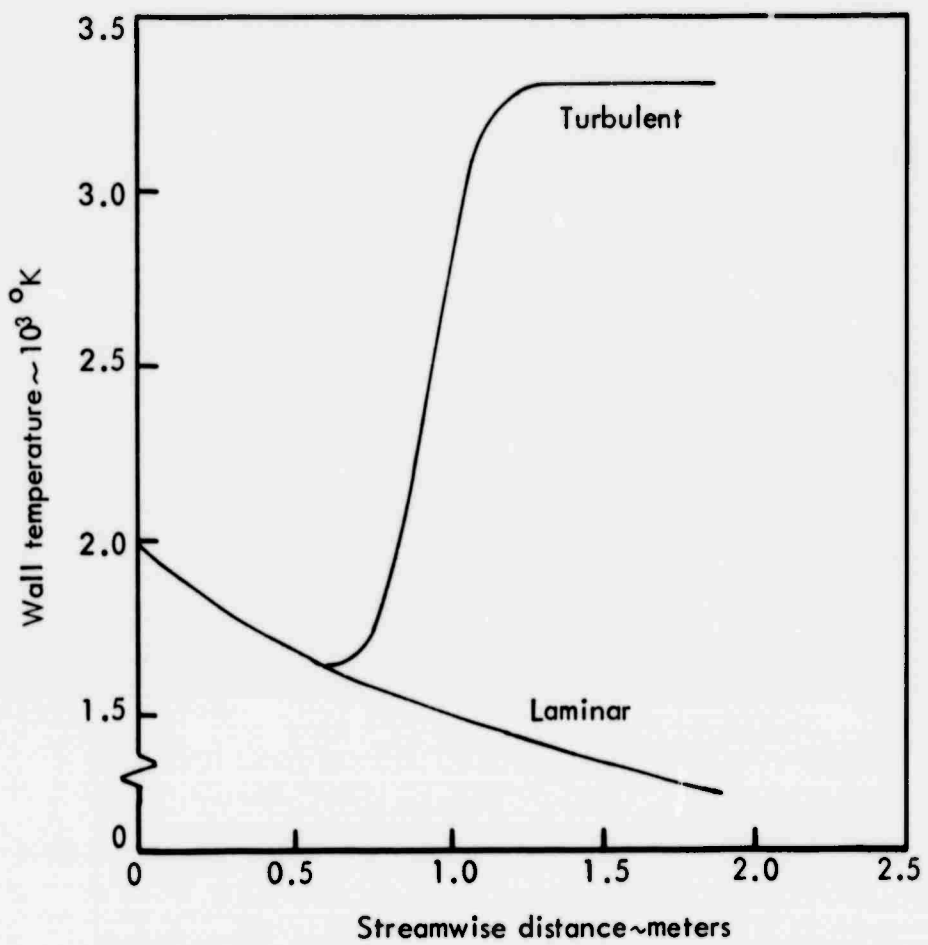


FIGURE 10 LTBLCEQL WALL TEMPERATURE DISTRIBUTION

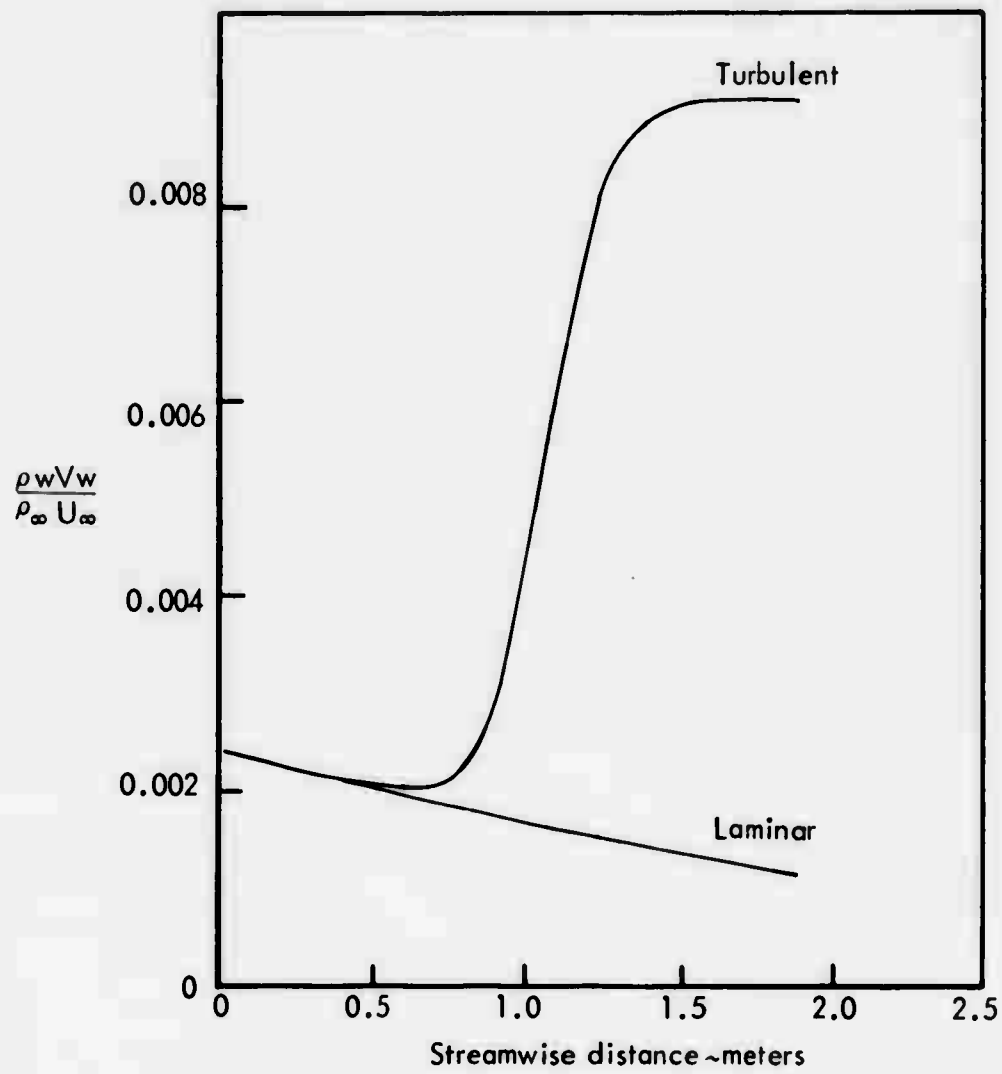


FIGURE 11 LTBLCEQL NORMALIZED WALL MASS TRANSFER DISTRIBUTION

Shown in Figures 12 through 15 are the results of the LTBLCEQL fully laminar boundary layer solutions with and without wall mass transfer. Figure 12 depicts the boundary layer edge Mach number distribution. This figure is significant in that it shows the extent of shock layer entropy swallowing by the boundary layer. The streamline which passes through a normal shock can achieve a maximum Mach number back on the cone of only 3.5, whereas a streamline which passes through a conical shock achieves a Mach number of 12. These two values represent the extremes in the boundary layer edge Mach number on the cone. The end of body Mach number of 8 in Figure 12 indicates that nose tip effects are still significant even through the streamwise distance is equivalent to 113 nose radii.

Figure 13 portrays the boundary layer shear stress distribution on the wall due to skin friction. The effects of wall mass transfer are much in evidence with the transpiration effect reducing the skin friction by approximately 20 percent. Also much in evidence is the pressure overexpansion and recompression aft of the nosetip, indicating the strong coupling between the skin friction and the boundary layer edge pressure.

The growth of the boundary layer over the body is shown in Figures 14 and 15 where both the boundary layer velocity thickness δ and the boundary layer displacement thickness δ^* are plotted as a function of the streamwise distance. The boundary layer displacement thickness δ^* is defined as

$$\delta^* = \int_0^{\infty} \left(1 - \frac{\rho u}{\rho_e u_e} \right) dy \quad (32a)$$

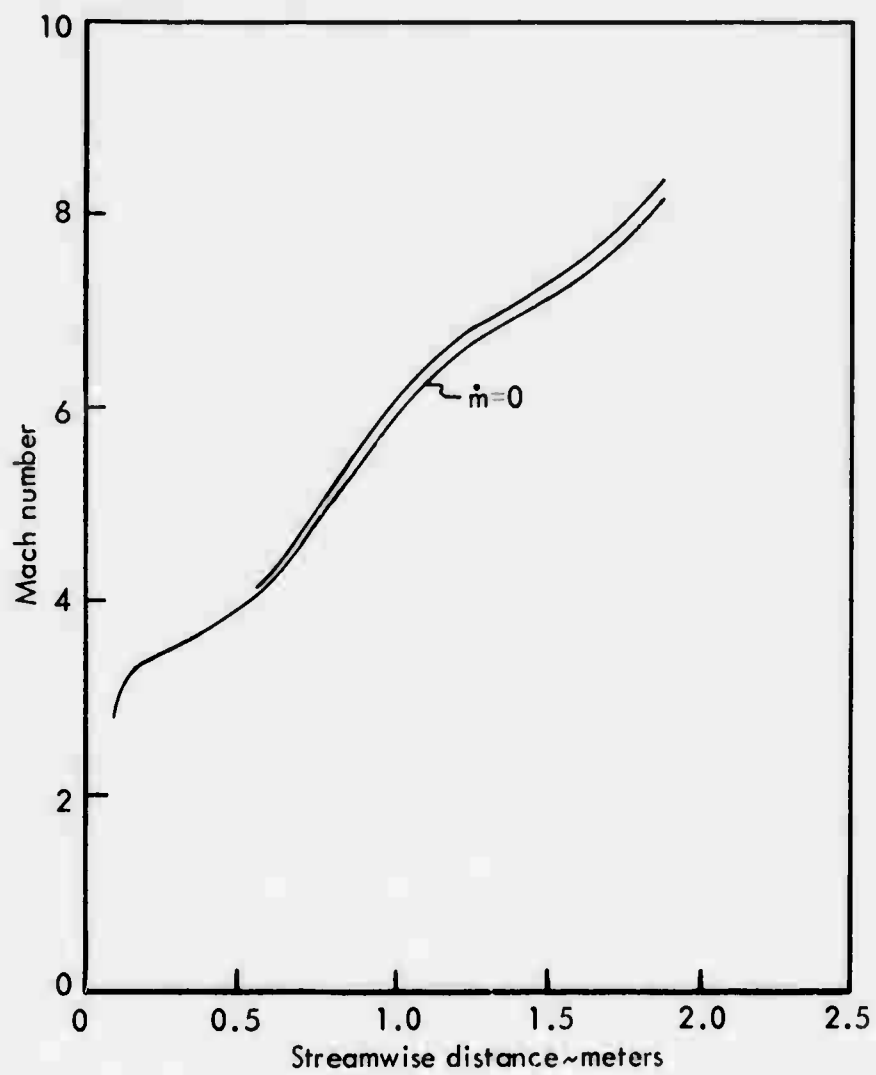


FIGURE 12 BOUNDARY LAYER EDGE MACH NUMBER, LAMINAR FLOW

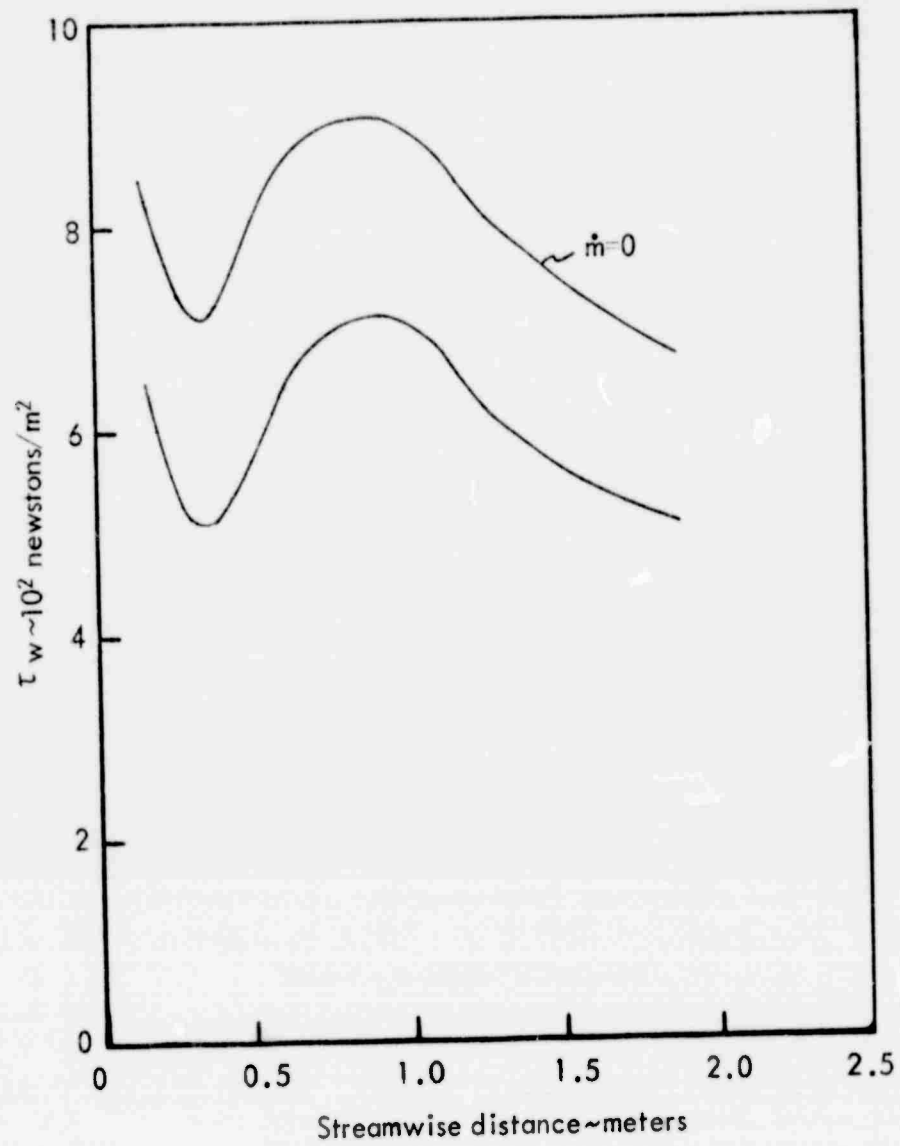


FIGURE 13 WALL SHEAR STRESS DISTRIBUTION, LAMINAR FLOW

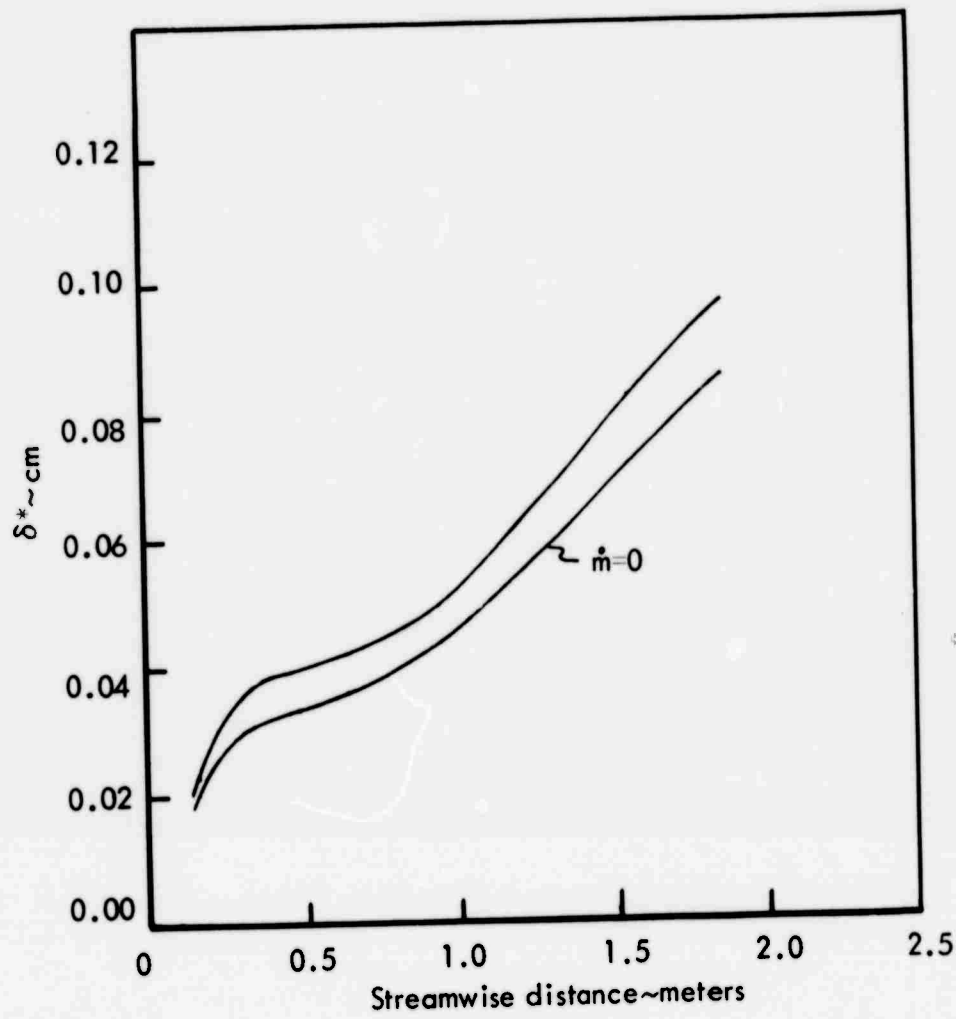


FIGURE 14 BOUNDARY LAYER DISPLACEMENT THICKNESS, LAMINAR FLOW

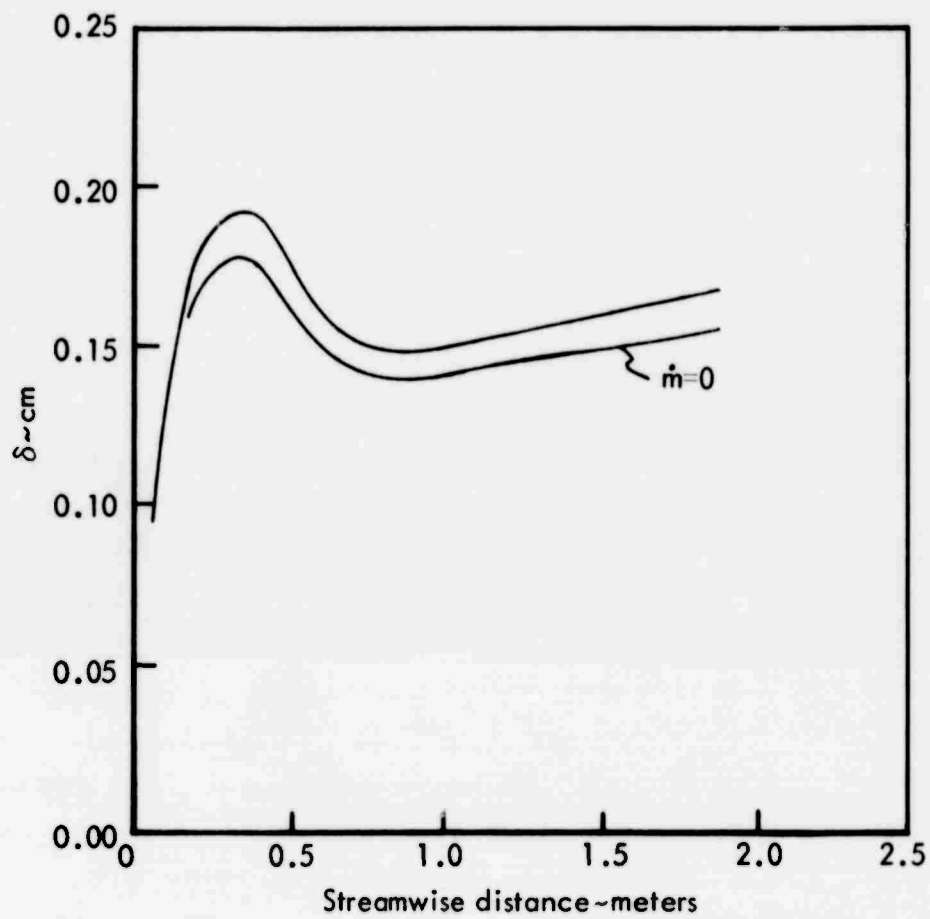


FIGURE 15 BOUNDARY LAYER VELOCITY THICKNESS, LAMINAR FLOW

or, in transformed variables as

$$\delta^* = \int_0^{\eta_{\infty}} \left(\frac{\rho_e}{\rho} - f' \right) \frac{\sqrt{2\xi}}{e e^r} d\eta \quad (32b)$$

and represents the amount of displacement of the inviscid flow beyond the normal outline of the actual body shape produced by the presence of the boundary layer. The boundary layer velocity thickness δ is defined as the height above the wall where the velocity in the boundary layer is 0.995 that of the inviscid velocity.

The inclusion of wall mass transfer is seen to increase both the displacement thickness and the velocity thickness, with the effects of mass transfer more observable in the displacement thickness profile. The velocity thickness is roughly a constant .15 cm over most of the body, unlike the displacement thickness which grows monotonically with running length. The relatively constant thickness boundary layer is the result of the strong entropy gradient which exists along the length of the body. The forward regions of the body are typified by high entropy, low density normal shock gas and the entropy decreases and density increases at the more rearward stations. This results in an increase in the mass flux within the boundary layer with increasing running length without a corresponding increase in the boundary layer thickness.

The total standoff of the shock wave from the body at the end of body station is 4.27 cm as determined from the inviscid flow method of characteristics solution. This corresponds to a boundary layer displacement thickness of .091 cm shown in Figure 14. Thus, the boundary layer displacement thickness is seen to be small in comparison to the shock layer thickness for the case of fully laminar flow, indicating that an uncoupled approach to the viscous and inviscid flow should be satisfactory.

Transitional boundary layer calculations at zero angle of attack were accomplished using the LTBLCEQL computer code assuming that boundary layer transition began at the .61-meter axial station and ended at the 1.22-meter axial station. Thus, fully laminar flow existed from the nose rearward to the .61-meter axial station and fully turbulent flow existed from the 1.22-meter to the 1.83-meter axial station (end of body). Solutions were obtained for both zero wall mass transfer and the turbulent wall mass transfer distribution shown in Figure 11. The boundary layer transitional flow was modeled using the transition intermittancy factor described above.

The results of the LTBLCEQL transitional boundary layer calculations are plotted in Figures 16 through 19. Figure 16 depicts the boundary layer edge Mach number as a function of the streamwise distance. This plot is an effective measure of the degree of shock layer entropy swallowing which occurs due to boundary layer growth on the body. As seen in the figure, the boundary layer edge Mach number increases rapidly during the transitional flow region and approaches the sharp cone inviscid Mach number of 12 at the end of the transitional region. This is due to the rapid increase in boundary layer thickness and mass flux during the transition process. The presence of wall mass transfer is seen to have only a minimal effect on the edge Mach number distribution.

The streamwise distribution of the boundary layer wall shear stress is pictured in Figure 17. The rapid increase in wall shear stress is observed during transitional flow, with the wall shear stress increasing by about a factor of six during transition. The double hump shape of the shear stress distribution is caused by the external pressure distribution, with the first maxima a direct function of the pressure maxima at $x \approx 1$ meter and the second maxima corresponding to the onset of fully

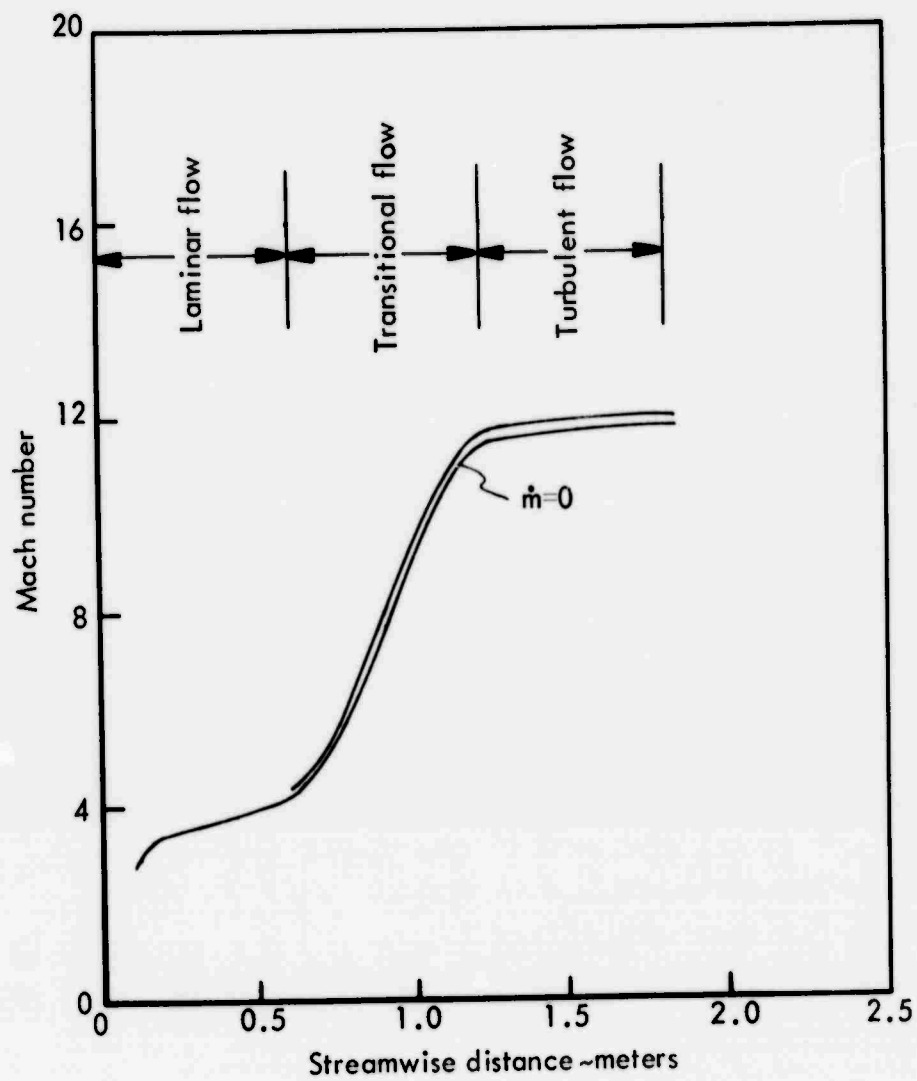


FIGURE 16 BOUNDARY LAYER EDGE MACH NUMBER

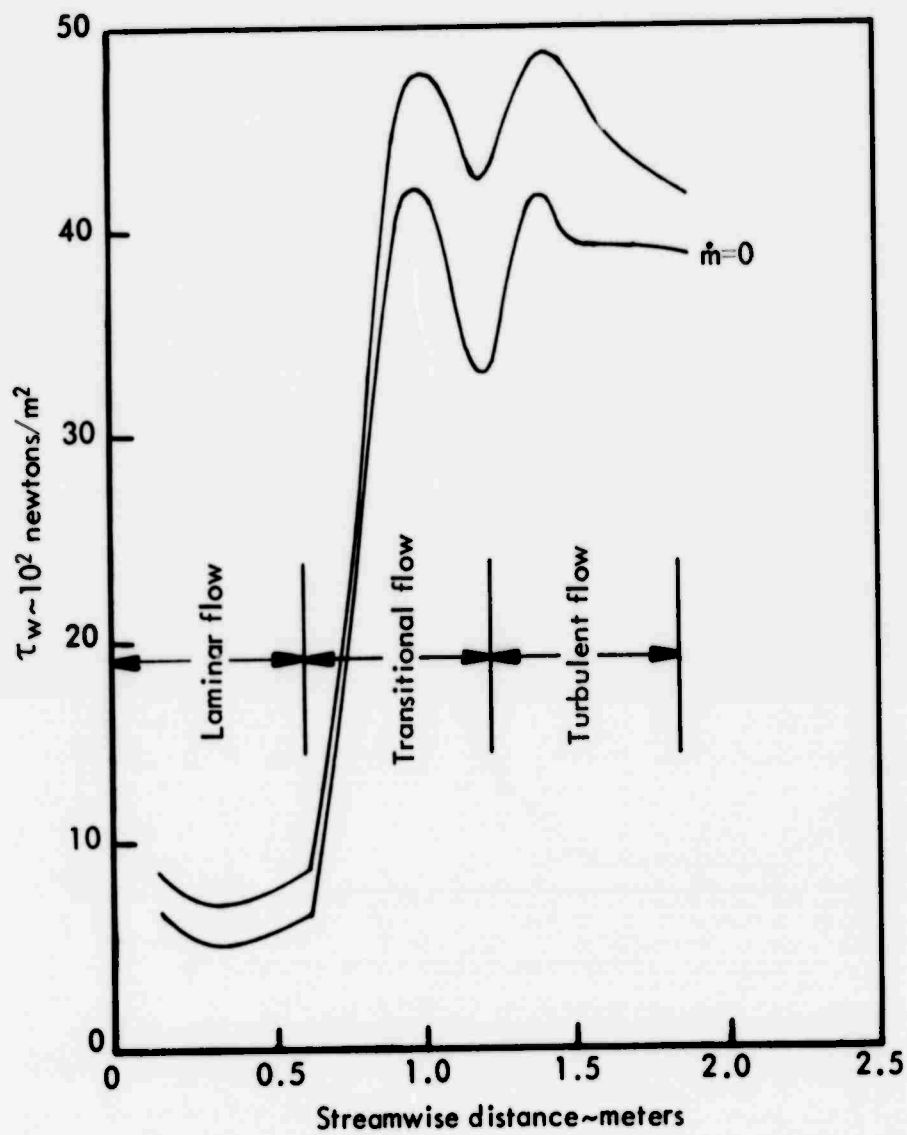


FIGURE 17 WALL SHEAR STRESS DISTRIBUTION, TRANSITIONAL FLOW

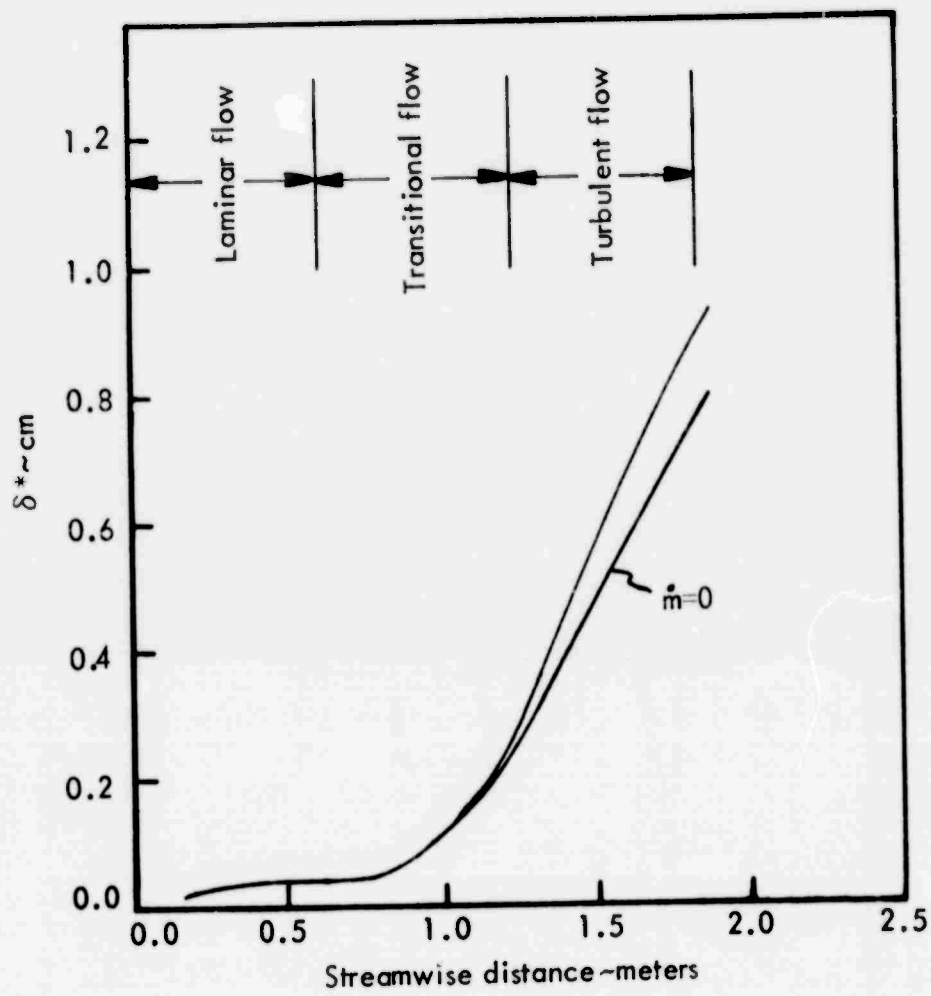


FIGURE 18 BOUNDARY LAYER DISPLACEMENT THICKNESS

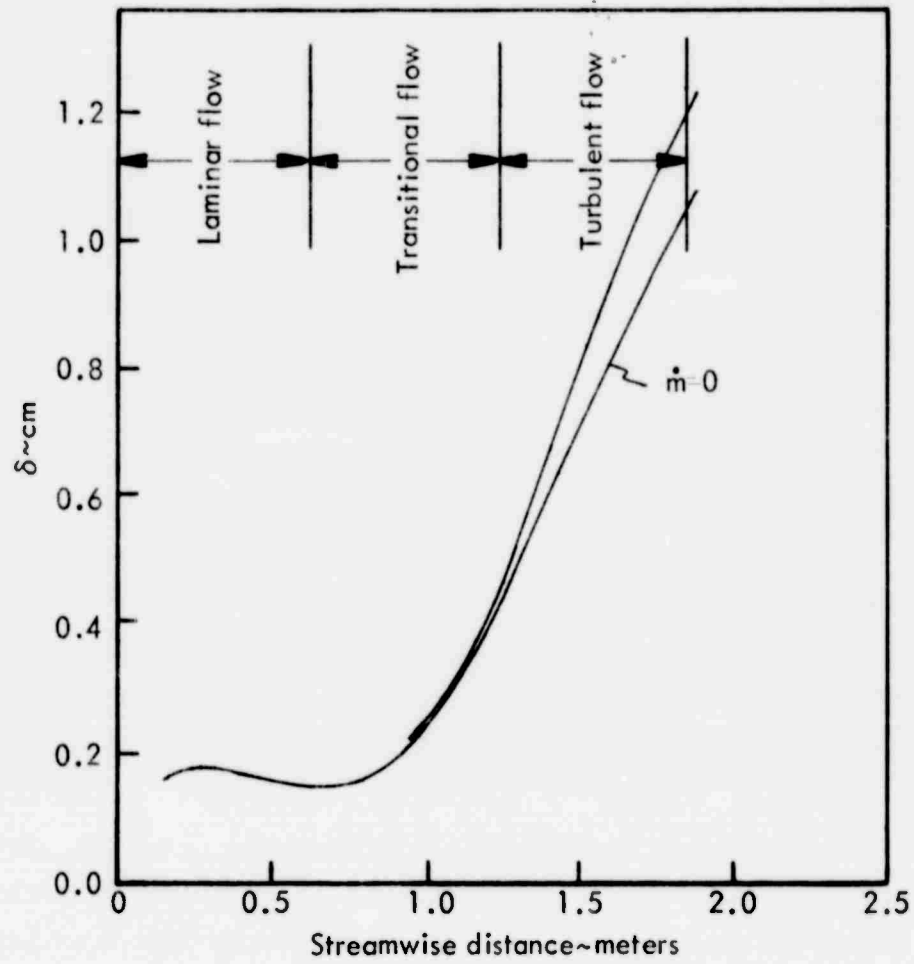


FIGURE 19 BOUNDARY LAYER VELOCITY THICKNESS

developed turbulent flow. The effect of wall mass transfer is observed to be almost of the same importance as with the fully laminar solutions, with a 10-20 percent reduction in the turbulent skin friction due to transpiration effects.

The variation of the boundary layer displacement thickness δ^* and the boundary layer velocity thickness δ along the length of the body is shown in Figures 18 and 19. The displacement thickness begins to increase rapidly during the transitional flow region and continues to increase at about the same rate throughout the turbulent boundary layer region. The turbulent boundary layer displacement thickness is approximately an order of magnitude greater than the laminar boundary layer displacement thickness at the end of body station. This can be compared to an increase in the turbulent boundary layer velocity and displacement thickness of about 10 percent for the non-zero wall mass transfer case when compared to the zero wall mass transfer case. Thus the most important boundary layer thickening mechanism appears to be the onset of turbulence within the boundary layer rather than the onset of high blowing rates caused by turbulent heat transfer. The increased mass transfer rates associated with turbulent boundary layer ablation produces increases in the boundary layer thickness that is an order of magnitude less than that associated with the onset of purely unblown turbulence in the boundary layer.

The turbulent boundary layer displacement thickness at the end of the body of .91 cm is approximately 20 percent of the end of body shock layer thickness of 4.27 cm. The assumption of uncoupled inviscid and viscous flows is being strained somewhat for the situation of turbulent boundary layer flow at 24.38-km altitude. While the solutions presented here are adequate, the 24.38-km altitude at transition most likely represents the limiting altitude at which the uncoupled approach can be employed. Calculations of transitional boundary layer flows at higher

altitudes should employ either an iterative approach to the inviscid-viscous flow field interface or a viscous shock layer approach.

2.4.2 Angle of Attack Analysis

In practice, all reentry vehicle flight tests possess non-zero angle of attack values coincident with the occurrence of boundary layer transition on the heatshield. Coupled with this is the experience gained in ground tests which uniformly show leeward side progression of transition on sharp and blunt cones at angle of attack. Thus, angle of attack effects may be critical to the understanding of the effects of boundary layer transition on the dynamic behavior of reentry vehicles. Included in this effort was a study of angle of attack effects on the reference vehicle at the reference altitude of 24.38 km. Angles of attack of 1.5, 3.0 and 4.5 degrees were considered.

The angle of attack boundary layer solutions were obtained using the 3-D boundary layer code (Reference 16). This code treats the full three-dimensional steady boundary layer analysis of sharp and blunt cones at angle of attack to supersonic and hypersonic flows. The program includes the effects of surface mass transfer of various foreign gases at the wall to simulate ablation and also includes laminar, transitional and turbulent boundary layer analysis. The turbulent boundary layer has been modeled using an invariant model of three-dimensional turbulence which employs the two-layer eddy viscosity mixing length approach. An intermittency factor has been used through the transition regime to express the probability of flow being turbulent at each solution point. The governing boundary layer equations are integrated on a digital computer using a marching implicit finite-difference scheme.

The three dimensional compressible boundary layer equations are very similar to those developed above for axisymmetric flow with the added complexity of the velocity component w and the fluctuating velocity component w' acting in the ϕ direction. The analysis employed in the 3-D boundary layer code is limited to ideal gas flows and does not treat entropy gradient effects. The usual assumption of an uncoupled approach to the inviscid flow is in effect. For completeness, the compressible three-dimensional boundary layer equations are presented here without derivation in terms of mean physical variables.

Continuity Equation

$$\frac{\partial}{\partial x} (\rho u r) + \frac{\partial}{\partial y} (\rho V r) + \frac{\partial}{\partial \phi} (\rho w) = 0 \quad (33)$$

Streamwise Momentum Equation

$$\rho u \frac{\partial u}{\partial x} + \rho V \frac{\partial u}{\partial y} + \rho \frac{w}{r} \frac{\partial u}{\partial \phi} - \rho \frac{w^2}{r} \frac{\partial r}{\partial x} = \frac{-\partial P_e}{\partial x} + \frac{\partial}{\partial y} \left[\mu \frac{\partial u}{\partial y} - \rho u' v' \right] \quad (34)$$

Transverse Momentum Equation

$$\rho u \frac{\partial w}{\partial x} + \rho V \frac{\partial w}{\partial y} + \rho \frac{w}{r} \frac{\partial w}{\partial \phi} + \rho \frac{uw}{r} \frac{\partial r}{\partial x} = \frac{-1}{r} \frac{\partial P_e}{\partial \phi} + \frac{\partial}{\partial y} \left[\mu \frac{\partial w}{\partial y} - \rho v' w' \right] \quad (35)$$

Normal Momentum Equation

$$\frac{\partial P}{\partial y} = 0 \quad (36)$$

Energy Equation

$$\rho u \frac{\partial H}{\partial x} + \rho V \frac{\partial H}{\partial y} + \rho \frac{w}{r} \frac{\partial H}{\partial \phi} = \frac{\partial}{\partial y} \left[\mu \left(\frac{\partial H}{\partial y} + \frac{1-Pr}{Pr} \frac{\partial h}{\partial y} \right) - \rho v' H' \right] \quad (37)$$

$$+ \frac{\partial}{\partial y} \left[\frac{\mu}{Pr} (Le-1) (h_f - h_i) \frac{\partial C_f}{\partial y} + \sum_i h_i \rho v' C_i' \right]$$

Species Equation

$$\rho u \frac{\partial C_i}{\partial x} + \rho v \frac{\partial C_i}{\partial y} + \rho \frac{w}{r} \frac{\partial C_i}{\partial \phi} = \frac{\partial}{\partial y} \left(\frac{\mu}{Pr} \frac{\partial C_i}{\partial y} + \rho v' C_i' \right) \quad (38)$$

where $V = v + \rho'v'/\rho$. The equation of state for each species is:

$$P_i = \frac{\rho_i}{M_i} RT \quad (39)$$

where R is the universal gas constant. Only one species equation is necessary since in a two-component mixture the mass fractions sum to unity:

$$\sum_i C_i = 1 \quad (40)$$

The viscosity and thermal conductivity are related by the Prandtl number:

$$Pr = \mu C_p / k \quad (41)$$

where

$$C_p = \sum_i C_i C_{p_i}$$

Similarly, diffusion and thermal conductivity are related by the Lewis number:

$$Le = \rho D_{if} C_p / k \quad (42)$$

The boundary conditions on the above equations are as follows:

Momentum Equations

$$\begin{aligned}y = 0: \quad u = w = u'v' = v'w' = \rho'v' = 0, \quad v = v_w \\y \rightarrow \infty: \quad u = u_e, \quad w = w_e \\u'v' = v'w' = \rho'v' = 0\end{aligned} \tag{43}$$

Energy Equations

$$\begin{aligned}y = 0: \quad H = H_w, \quad v'H' = 0 \\y \rightarrow \infty: \quad H = H_e, \quad v'H' = 0\end{aligned} \tag{44}$$

Species Equations

$$\begin{aligned}y = 0: \quad C_f = C_{f_w} = \left(\frac{D_{if}}{v} \frac{\partial C_f}{\partial y} \right)_w, \quad v'C'_i = 0 \\y \rightarrow \infty: \quad C_f = 1.0, \quad v'C'_i = 0\end{aligned} \tag{45}$$

In the derivation of the conservation equations the usual assumptions regarding the fluctuating quantities have been employed. These are:

- 1) The turbulent level is small and therefore terms having the mean square of the velocity fluctuation are dropped from the equations.
- 2) Molecular transport parameters are approximated by the mean flow counterparts.
- 3) The rate of change of mean flow properties in the normal direction is an order of magnitude greater than the rates of change in the streamwise and transverse directions.

The solution of the governing equations requires the expression of the turbulent shear terms and the turbulent flux of total enthalpy in terms of the mean flow quantities. A popular concept used to obtain these expressions is the eddy viscosity, eddy-conductivity analogy with the molecular viscosity and conductivity where:

$$\begin{aligned} -\rho u'v' &= \epsilon_x \partial u / \partial y \\ -\rho v'w' &= \epsilon_\phi \partial w / \partial y \end{aligned} \quad (46)$$

and

$$-\rho v'H' = k_t \partial H / \partial y$$

and where the dimensionless transport parameters are:

$$Pr_t = C_p \epsilon / k_t$$

$$Le_t = \rho D_t C_p / k_t$$

Windward Plane Conservation Equations

On the windward plane of a cone, the transverse (crossflow) velocity, w , and $\partial Pe / \partial \phi$ vanish due to symmetry; however, the crossflow velocity gradient does not vanish and still appears in the continuity equation. Under these conditions the transverse momentum equation would vanish completely at the windward plane where initial profiles are generated for the remaining integration of the governing equations. To avoid this problem, Moore (Reference 17) has suggested that the transverse momentum equation first be differentiated with respect to ϕ before neglecting terms which vanish at the windward streamline. This procedure results in the following transverse momentum equation at the windward plane:

$$\begin{aligned} \rho u \frac{\partial}{\partial x} \left(\frac{\partial w}{\partial \phi} \right) + \frac{\rho}{r} \left(\frac{\partial w}{\partial \phi} \right)^2 + \rho v \frac{\partial}{\partial y} \left(\frac{\partial w}{\partial \phi} \right) + \rho \frac{u}{r} \frac{\partial w}{\partial \phi} \frac{\partial r}{\partial x} \\ = \frac{-1}{r} \frac{\partial^2 p_e}{\partial \phi^2} + \frac{\partial}{\partial y} \left[(\mu + I_f \epsilon) \frac{\partial}{\partial y} \left(\frac{\partial w}{\partial \phi} \right) \right] \end{aligned} \quad (47)$$

The remaining conservation equations are reduced to a quasi-two-dimensional form at the windward plane where $w = 0$. The continuity equation serves as the only coupling between the transverse momentum equation and the remaining governing equations. For cones at zero angle of attack the transverse momentum equation in either form vanishes identically leaving a completely axisymmetric problem.

A more convenient form of the governing equations for numerical solution is obtained by introducing two stream functions defined as follows:

$$\Psi(x, y) = \sqrt{2\xi} f(\xi, \eta) \quad (48a)$$

$$\psi(x, y) = \sqrt{2\xi/r} g(\xi, \eta) \quad (48b)$$

where ξ, η are the Levy-Lees transformed coordinates defined as follows:

$$\xi(x) = \int_0^x \rho_r \mu_r u_r r^2 dx \quad (49a)$$

$$\eta(x, \phi, y) = \rho_e u_e r / \sqrt{2\xi} \int_0^y \frac{\rho}{\rho_e} dy \quad (49b)$$

This coordinate transformation removes the singularity at $x = 0$ and stretches the normal coordinate. Accordingly, the transformed derivatives become:

$$\frac{\partial}{\partial x} = \rho_r u_r \mu_r r^2 \frac{\partial}{\partial \xi} + \frac{\partial \eta}{\partial x} \frac{\partial}{\partial \eta} \quad (50a)$$

$$\frac{\partial}{\partial \phi} = \frac{\partial}{\partial \phi} + \frac{\partial \eta}{\partial \phi} \frac{\partial}{\partial \eta} \quad (50b)$$

$$\frac{\partial}{\partial y} = \rho u_e r / \sqrt{2\xi} \frac{\partial}{\partial \eta} \quad (50c)$$

Satisfying the continuity equation with the above stream functions, the following relations are obtained:

$$\rho u r = \frac{\partial \Psi}{\partial y} \quad (51a)$$

$$\rho w = \frac{\partial \psi}{\partial y} \quad (51b)$$

$$\rho v r = \frac{-\partial \Psi}{\partial x} - \frac{\partial \psi}{\partial \phi} \quad (51c)$$

Using Equations (50a), (50c) and (51c) results in the following expression:

$$\frac{\rho v r \sqrt{2\xi}}{\rho_r u_r \mu_r r^2} + \eta_x \delta r f' + \eta_\phi \delta g' + 2\xi \frac{\partial f}{\partial \xi} + f + \delta \frac{\partial g}{\partial \phi} = 0 \quad (52)$$

or

$$V + 2\xi \frac{\partial f}{\partial \xi} + f + \delta \frac{\partial g}{\partial \phi} = 0 \quad (53)$$

where

$$V = \rho v r \sqrt{2\xi} / \rho_r u_r \mu_r r^2 + \eta_x \delta r f' + \eta_\phi \delta g' \quad (54)$$

and

$$\delta = 2\xi / \rho_r u_r \mu_r r^3 \quad (55)$$

Differentiation of Equation (51a) with respect to y using Equation (50c) gives the expression for f' :

$$f' = \frac{u}{u_e} \quad (56)$$

Similarly, differentiation of Equation (51b) with respect to y using Equation (50c) gives the expression for g' :

$$g' = \frac{w}{u_e} \quad (57)$$

Evaluating the momentum Equations (34) and (35) at the outer edge gives the pressure gradients as:

$$\frac{-\partial P_e}{\partial x} = \rho_e u_e \frac{\partial u_e}{\partial x} + \frac{\rho_e w_e}{r} \frac{\partial u_e}{\partial \phi} - \frac{\rho_e w_e^2}{r} \frac{\partial r}{\partial x} \quad (58)$$

$$\frac{-1}{r} \frac{\partial P_e}{\partial \phi} = \rho_e u_e \frac{\partial w_e}{\partial x} + \frac{\rho_e w_e}{r} \frac{\partial w_e}{\partial \phi} + \frac{\rho_e u_e w_e}{r} \frac{\partial r}{\partial x} \quad (59)$$

Using Equations (50a) - (59) the governing conservation equations are now expressed in terms of transformed variables.

To obtain the transformed equations at the windward streamline, two new stream functions are introduced in order to satisfy the windward plane continuity equation, as follows:

$$\Psi = \sqrt{2\xi} f \quad (60)$$

$$\psi = \sqrt{2\xi} g \quad (61)$$

The transformed equations are then obtained in the same manner as for the general three-dimensional case. For a cone at zero angle of attack, the system of transformed equations reduces to a fully axisymmetric system without a transverse momentum equation.

Equations at the Stagnation Point

At the stagnation point of a blunt cone, the boundary-layer equations have a removable singularity. In the limit as $\xi \rightarrow 0$ the expressions for ξ and η are:

$$\xi(x) = \rho_e \mu_e \frac{du_e}{dx} x^4/4 \quad (62)$$

and

$$\eta(x,y) = \left[2\rho_e/\mu_e \frac{du_e}{dx} \right]^{1/2} \int_0^y \rho/\rho_e dy \quad (63)$$

Also at the stagnation point of a blunt cone the expression for V in the windward plane continuity equation becomes:

$$V = \frac{\rho v}{\left[2\rho_e \mu_e \frac{du_e}{dx} \right]^{1/2}} \quad (64)$$

Eddy-Viscosity Models

Prandtl's mixing length hypothesis states that the eddy viscosity is the product of some characteristic length and the normal velocity gradient. For two-dimensional flow this concept leads to:

$$\epsilon = \rho l_*^2 \left| \frac{\partial u}{\partial y} \right| \quad (65)$$

Prandtl's studies assumed that the eddy viscosity should depend only on local eddy scale and on the properties of turbulence. Adams (Reference 18) extended this concept to the three-dimensional case by assuming that the eddy viscosity is also independent of coordinate direction. In the three-dimensional case ϵ becomes:

$$\epsilon = \epsilon_x = \epsilon_\phi = \rho l_*^2 \left[\left(\frac{\partial u}{\partial y} \right)^2 + \left(\frac{\partial w}{\partial y} \right)^2 \right]^{1/2} \quad (66)$$

which reduces to the two-dimensional form when $w = 0$. This is referred to as the invariant turbulence model.

The model used in this investigation is the common two-layer inner-outer model which uses the Prandtl mixing length theory and the Van Driest or Reichardt damping near the wall. The mixing length distribution is as follows:

$$\begin{aligned} \ell_* &= k_* y & \{0 < y \leq \lambda y_\ell / k_*\} \\ \ell_* &= \lambda y_\ell & \{\lambda y_\ell / k_* < y\} \end{aligned} \quad (67)$$

where

$$k_* = 0.435$$

$$\lambda = 0.09$$

$$y_\ell = y \text{ when } \left[(u^2 + w^2) / (u_e^2 + w_e^2) \right]^{1/2} = 0.99$$

The inner law is damped near the wall so as to yield the exact laminar shear stress term at the wall. To accomplish this, two different damping factors are used in the computer code, Van Driest's with local shear stress and Reichardt's (Reference 19) damping term.

Cebeci (Reference 20) developed a mass transfer correction to Van Driest's inner eddy-viscosity law by modifying the damping constant A^* . For turbulent flows with mass transfer Cebeci determined the damping constant to be

$$A^* = 26 \exp(-5.9 v_w^+) \quad (68)$$

where

$$v_w^+ = v_w / (\tau_w / \rho)^{1/2}$$

Reichardt's expression for the inner eddy-viscosity law was obtained by curve fitting experimental pipe flow data. The expression is:

$$\epsilon_i = \mu k_* \left[\frac{y \sqrt{\tau \rho}}{\mu} - 11.0 \tanh \left(\frac{y \sqrt{\tau \rho}}{11\mu} \right) \right] \quad (69)$$

As can be seen, this expression does not involve the velocity gradient terms. For this reason it is preferred for use in numerical solutions, since it usually requires fewer iterations to converge.

Following Equations (66) and (67), the outer eddy-viscosity law is:

$$\epsilon_o = \lambda^2 y_\ell^2 \partial E / \partial y$$

The outer eddy-viscosity law is used in conjunction with the Klebanoff (Reference 21) intermittency factor assures a smooth approach of ϵ_o to zero as $y \rightarrow \delta$. The modified law is:

$$\epsilon_o = \lambda^2 y_\ell^2 \gamma \partial E / \partial y \quad (70)$$

where γ is Klebanoff's intermittency factor:

$$\gamma = \left[1 + 5.5 (y/\delta)^6 \right]^{-1} \quad (71)$$

Transition Models

Two models of transition from laminar to turbulent flow are used in the computer code. One model is simply instantaneous transition to turbulent flow, and there really is no transition region or zone at all. In the second case a smooth transition to turbulent flow occurs over a prescribed distance. This distance is known as the transition zone and is defined as the distance between the onset of transition at $x = X_t$ and the beginning of fully turbulent flow at $x = X_T$ at some point downstream.

The probability of turbulent flow at any point is expressed by a model by Dahwan and Narasimha (Reference 22) as:

$$I_f(X) = 1 - \exp \left[0.412 (2.917)^2 \left(\frac{(X-X_t)}{(X_T-X_t)} \right)^2 \right] \quad (72)$$

The transition intermittency factor is employed as a simple multiplier of the eddy viscosity in the governing equations and therefore acts as a damping coefficient for the fully turbulent eddy viscosity.

Finite-Difference Method

The finite-difference method used in our investigation follows the method used by McGowan and Davis (Reference 23) which is similar to the method developed by Dwyer (Reference 24) with modifications by Krause (Reference 25). The method has been further modified to include variable spacing for the normal coordinate. The accuracy of this method is second order. The method is stable for negative transverse velocities when proper step sizes are chosen.

The momentum, species and energy equations are written in standard parabolic form as:

$$A_0 \frac{\partial^2 w}{\partial \eta^2} + A_1 \frac{\partial w}{\partial \eta} + A_2 w + A_3 + A_4 \frac{\partial w}{\partial \xi} + A_5 \frac{\partial w}{\partial \phi} = 0 \quad (73)$$

where w is the dependent variable in each case. The coefficients A_0 through A_5 are determined from the transformed governing equations.

The derivatives in Equation (73) are replaced with finite-difference expressions at each of the grid points in η, ϕ, ξ space.

The finite-difference form of the Equations (73) results in simultaneous linear algebraic equations of tridigonal form which are solved by a method developed by Richtmyer (Reference 26). The boundary conditions at both the wall and the outer edge must be specified for this method.

Edge of the boundary layer conditions for the 3-D boundary layer code are established through the usual software interface with an uncoupled inviscid flow solution. Since the 3-D code does not perform entropy gradient calculations, only the boundary layer edge pressure need be specified. The boundary layer edge entropy is determined from a straightforward normal shock-isentropic expansion calculation within the code. The boundary layer edge pressure distribution may be determined a number of ways, from the very simple modified Newtonian or tangent-cone theories to the more complex method of characteristics solutions.

For the cases considered here, real gas three dimensional method of characteristics solutions were attempted using the Rakich (Reference 27) computer code. In all cases, the method of characteristics solutions developed instabilities in the pressure distribution on the leeward side of the vehicle. These instabilities were observed to occur farther forward on the vehicle at higher angles of attack. Attempts at using the method of characteristics pressure distributions with the instabilities present as boundary layer edge conditions in the 3-D code resulted in instabilities also occurring in the boundary layer solutions. The boundary layer instabilities were sufficient to cause a loss of several meridional solutions on the leeward side of the vehicle, in spite of a forced relaxation of the energy conservation criteria. This difficulty led to the abandonment of the use of method of characteristics solutions for specification of the angle of attack pressure distributions.

Two approaches to the specification of the angle of attack pressure distributions remained. A simple modified Newtonian theory could be used to describe the surface pressure distribution on a blunt cone at angle of attack or the analytical tables of Jones (Reference 28) can be used to describe the surface pressure distribution on a sharp cone at angle of attack. With the latter approach one would lose the nose bluntness features insofar as they apply to the pressure distribution. The most significant nose bluntness effect, entropy layer entrainment, was lost from the outset due to the inability of the three dimensional viscous flow field solution to properly account for the entropy layer gradient. In actuality, a better approximation to the boundary layer edge entropy can be obtained with an assumed sharp cone flow than with a blunt cone normal shock-isentropic expansion, since nearly all entropy swallowing was seen to occur upstream of the transition region for the zero angle of attack boundary layer solutions. The method of Jones was therefore selected for the angle of attack boundary layer edge pressure distribution.

In the absence of nose bluntness, the pressure distribution is independent of axial location on the vehicle and dependent solely on the meridional location. The meridional distribution of pressure on a sharp 9-degree half angle cone for angles of attack of 1.5, 3.0 and 4.5 degrees are shown in Figure 20. Implicit in these results is a freestream Mach number of 23.14 and a freestream pressure of 2801 N/m^2 .

Due to the addition of a sharp nose tip to the basic reference vehicle for the angle of attack viscous flow field calculations, alternatives existed for maintaining either the vehicle length or the base diameter the same as the blunt nose

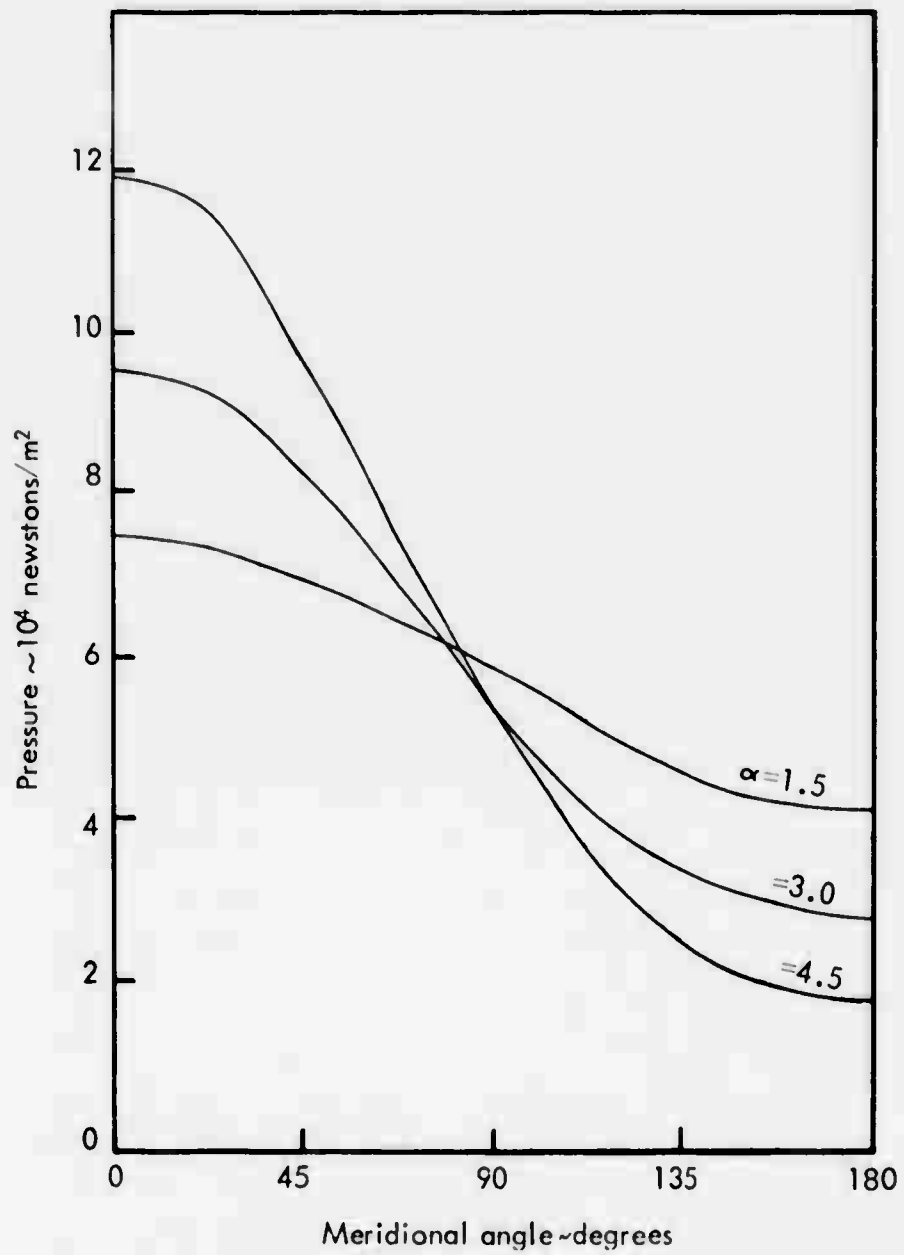


FIGURE 20 SHARP CONE PRESSURE DISTRIBUTION AT ANGLE OF ATTACK

zero angle of attack calculations. The latter alternative was selected, thus increasing the overall length of the vehicle to 1.918 meters as opposed to the 1.824 meters blunt nose vehicle length.

An asymmetrical transition front was employed for all three angle of attack viscous flow field solutions. The orientation of the transition front with respect to the body was consistent with the previous zero angle of attack calculations and also consistent with ground test transition experiments where leeward side progression of the transition front is observed. The transition front was a simple linear variation between complete laminar flow on the windward side of the vehicle to transitional flow on the leeward side of the vehicle. Leeward transition began at an axial distance of .61 meters and ended at an axial distance of 1.22 meters. Fully turbulent flow existed aft of the 1.22-meters axial station and fully laminar flow existed forward of the .61-meters axial station. The transition front was maintained constant at all three angles of attack.

The wall temperature and mass transfer rate distributions developed previously in Section 2.3 for the zero angle of attack viscous flow field solutions were applied directly to the present angle of attack calculations. Specifically, the distributions for fully laminar flow in Section 2.3 were used for the windward side distributions and the distributions for transitional flow in Section 2.3 were used for the leeward side distributions. A linear variation with meridional angle was used between these two extremes. All angle of attack viscous flow field calculations employed non-zero mass transfer rate distributions.

The results of the angle of attack three dimensional boundary layer calculations are shown in Figures 21 through 26. The first three figures show the streamwise variation in the wall shear stress at four different meridional angles. The

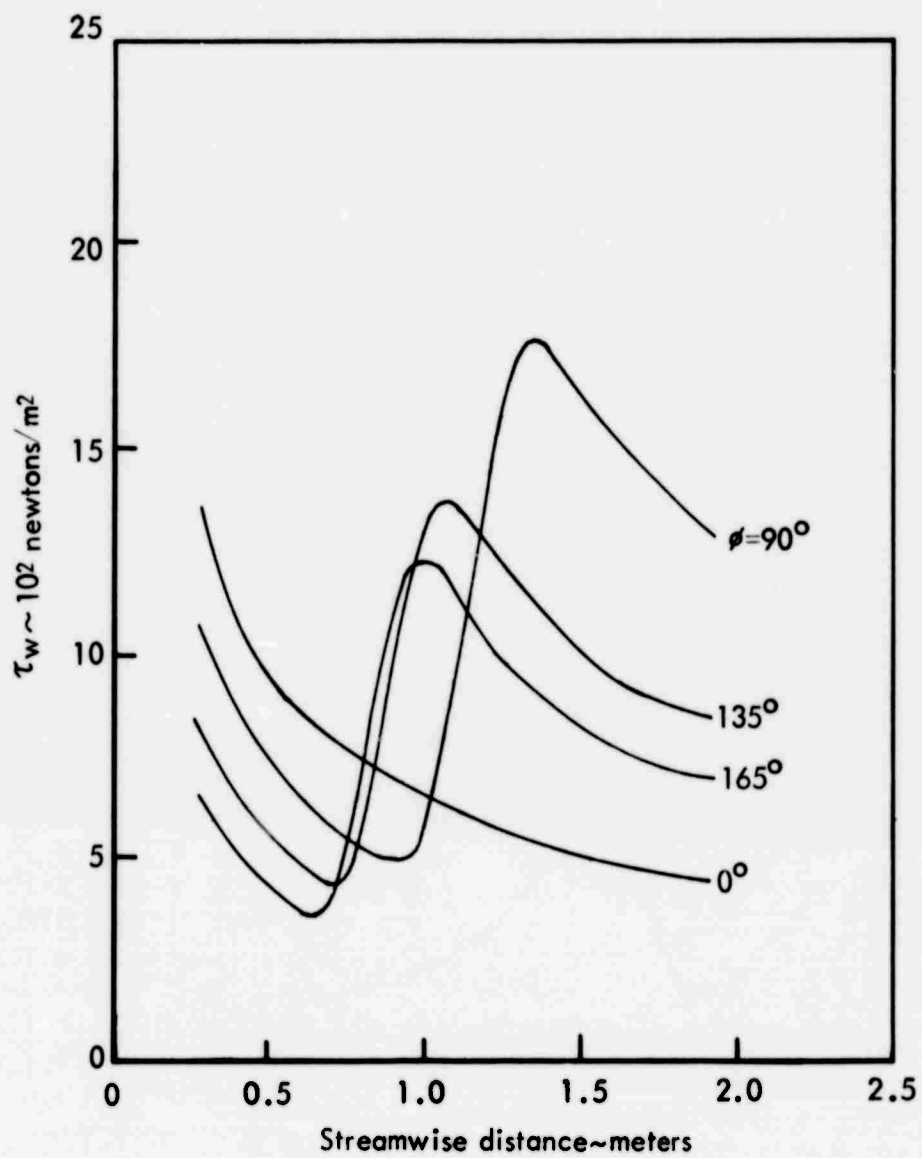


FIGURE 21 WALL SHEAR STRESS DISTRIBUTION, $\alpha=1.5$ DEGREES

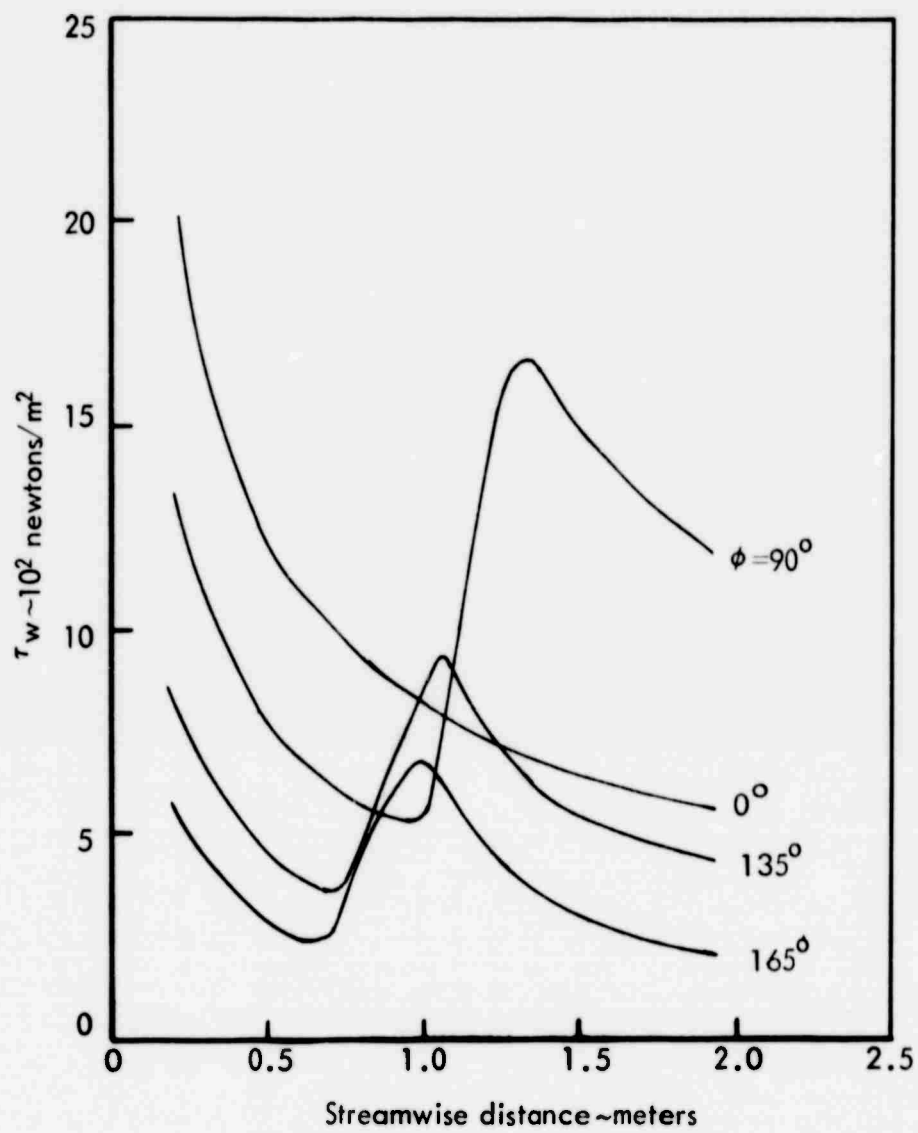


FIGURE 22 WALL SHEAR STRESS DISTRIBUTION, $\alpha=3.0$ DEGREES

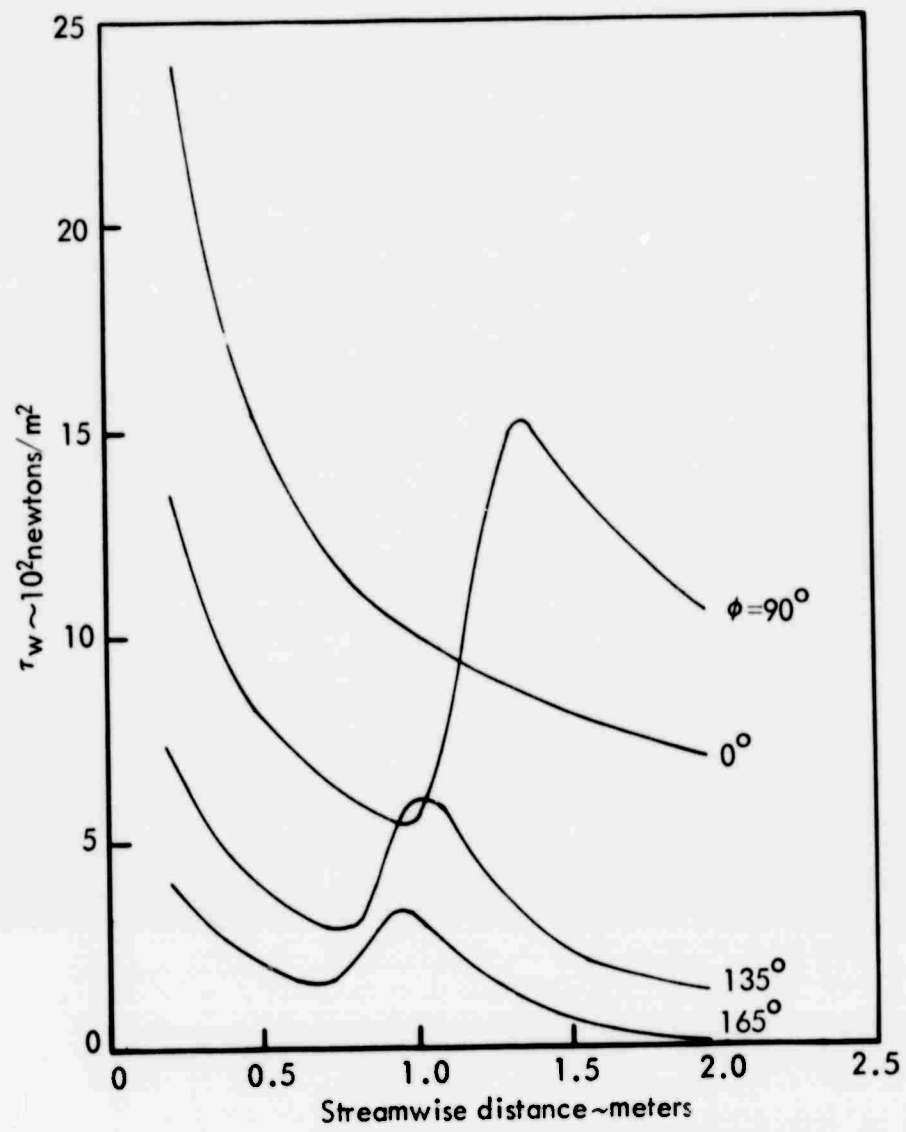


FIGURE 23 WALL SHEAR STRESS DISTRIBUTION, $\alpha=4.5$ DEGREES

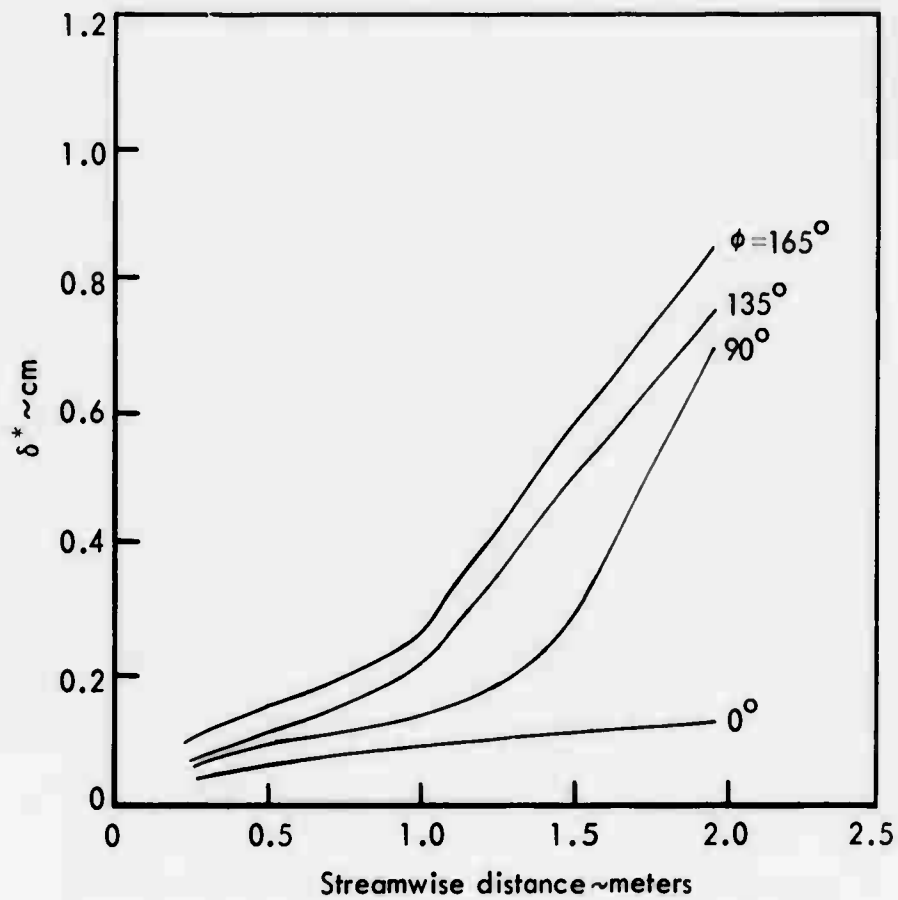


FIGURE 24 BOUNDARY LAYER DISPLACEMENT THICKNESS, $\alpha=1.5$ DEGREES

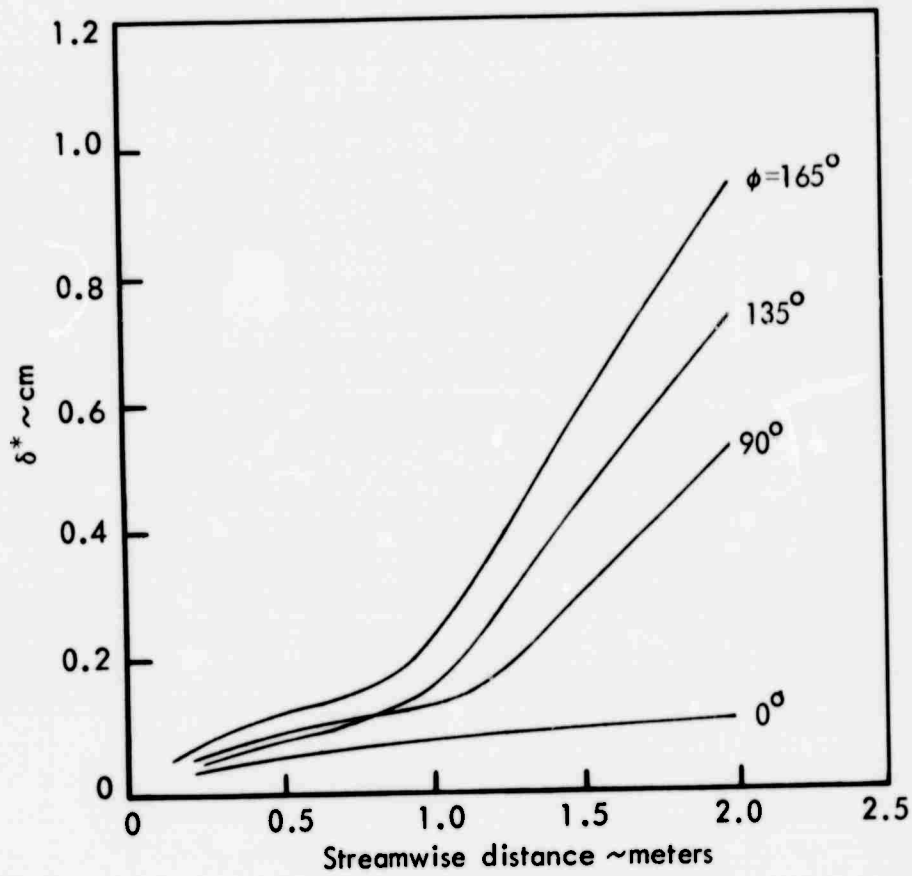


FIGURE 25 BOUNDARY LAYER DISPLACEMENT THICKNESS, $\alpha=3.0$ DEGREES

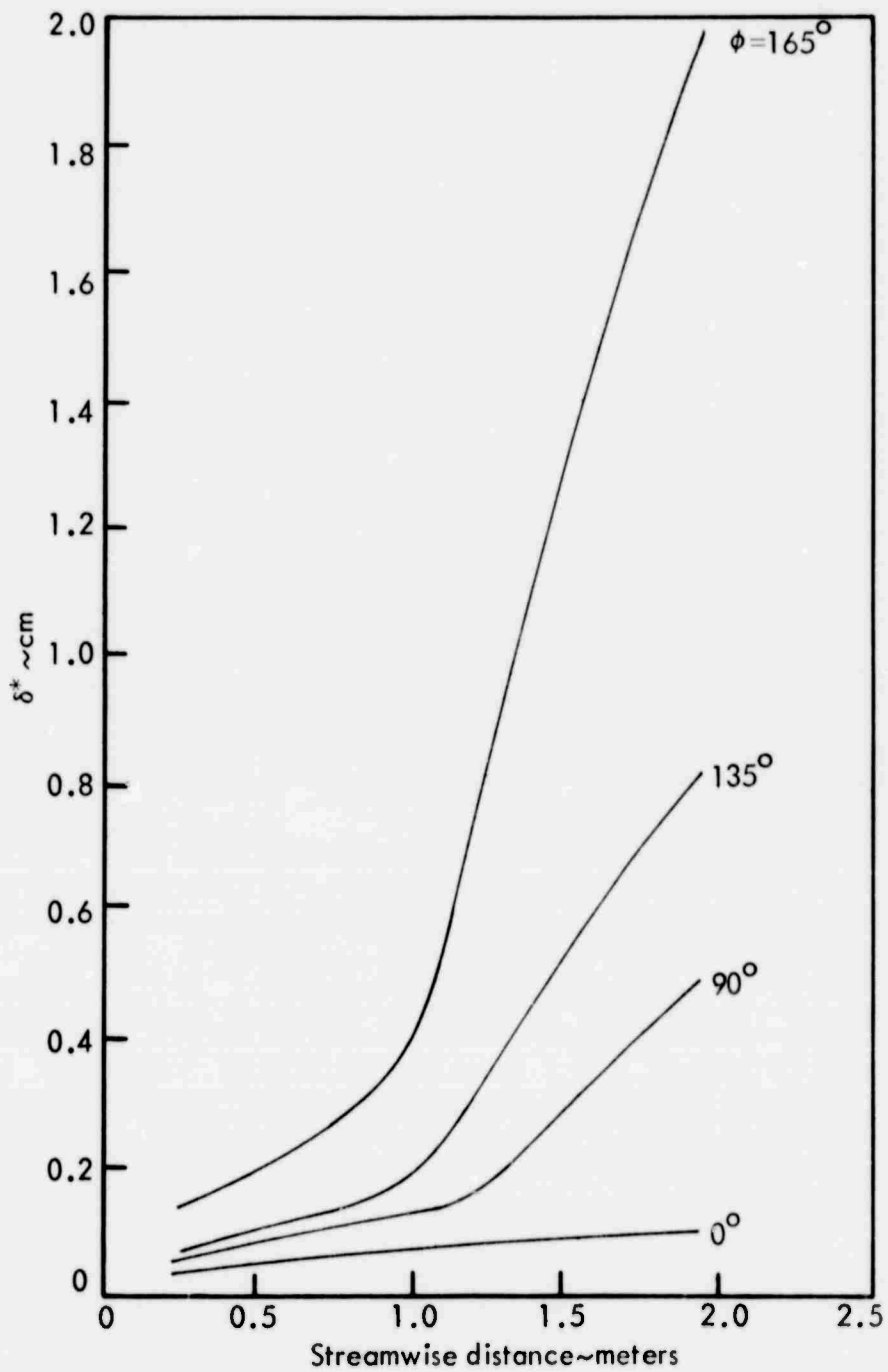


FIGURE 26 BOUNDARY LAYER DISPLACEMENT THICKNESS, $\alpha=4.5$ DEGREES

data shown in these figures indicate that the maximum turbulent shear stress occurs along the 90-degree meridian, half-way between the windward meridian at 0 degrees and the leeward meridian at 180 degrees. Inspection of the raw data indicates that the maximum is really near $\approx 40-45$ degrees meridionally and is at the very end of the body. Inception of transition is readily detected in the shear stress distribution, initially occurring on the leeside and gradually moving around the vehicle, but never reaching, the windward meridian.

Comparison of the shear stress distributions calculated for zero angle of attack in Section 2.4.1 with those presented here reveal two distinct differences.

1. The effects of the blunt nose overexpansion and recompression for the zero angle of attack calculations are not in evidence here due to the sharp nose configuration employed for the non-zero angle of attack calculations.
2. Turbulent boundary layer shear stresses for the zero angle of attack calculations appear higher than those calculated for the non-zero angle of attack cases. The superior treatment of entropy gradient effects in the zero angle of attack calculations is believed to be the cause of this difference.

The streamwise variation in the boundary layer displacement thickness for the three angle of attack calculations are shown in Figures 24 through 26. Once again, the effects of the onset of transition are much in evidence with, in general, about a factor of five increase in the rate of boundary layer growth

coincident with the transitional flow region along any meridian. The boundary layer displacement thickness does not change significantly between angles of attack of 1.5 and 3.0 degrees but dramatic increases are observed between 3.0 and 4.5 degrees.

2.4.3 Sharp Cone at Zero Angle of Attack

Fundamental differences are seen in the shear stress distributions obtained for the blunt cone zero angle of attack calculations obtained with the LTBLCEQL computer code as opposed to the sharp cone angle of attack calculations obtained with the 3-D boundary layer code. The blunt cone data do not appear to match-up well with the sharp cone data between 0- and 1.5-degrees angle of attack. To provide a consistent set of data for the understanding of angle of attack effects, a sharp cone solution was obtained for zero angle of attack. Free stream conditions, wall mass transfer rates and wall temperatures were identical to those mentioned above for both the sharp cone at angle of attack and the blunt cone at zero angle of attack.

The results of the sharp cone at zero angle of attack calculations are shown in Figures 27 through 29, where distributions of wall shear stress, boundary layer displacement thickness and boundary layer velocity thickness are depicted as a function of the streamwise distance. Results for the blunt cone at zero angle of attack are shown on the same figures as dashed lines. Differences between the two solutions are very apparent, particularly with the wall shear stress distribution. No attempt has been made to try and isolate the source of these differences. It is believed, however, that the use of the perfect gas equation of state, constant inviscid cone pressure and constant boundary layer edge entropy with the sharp cone results versus the real gas equilibrium equation of state, method of characteristics inviscid pressure distribution and entropy swallowing with the blunt cone results are the sources of the differences in the two solutions.

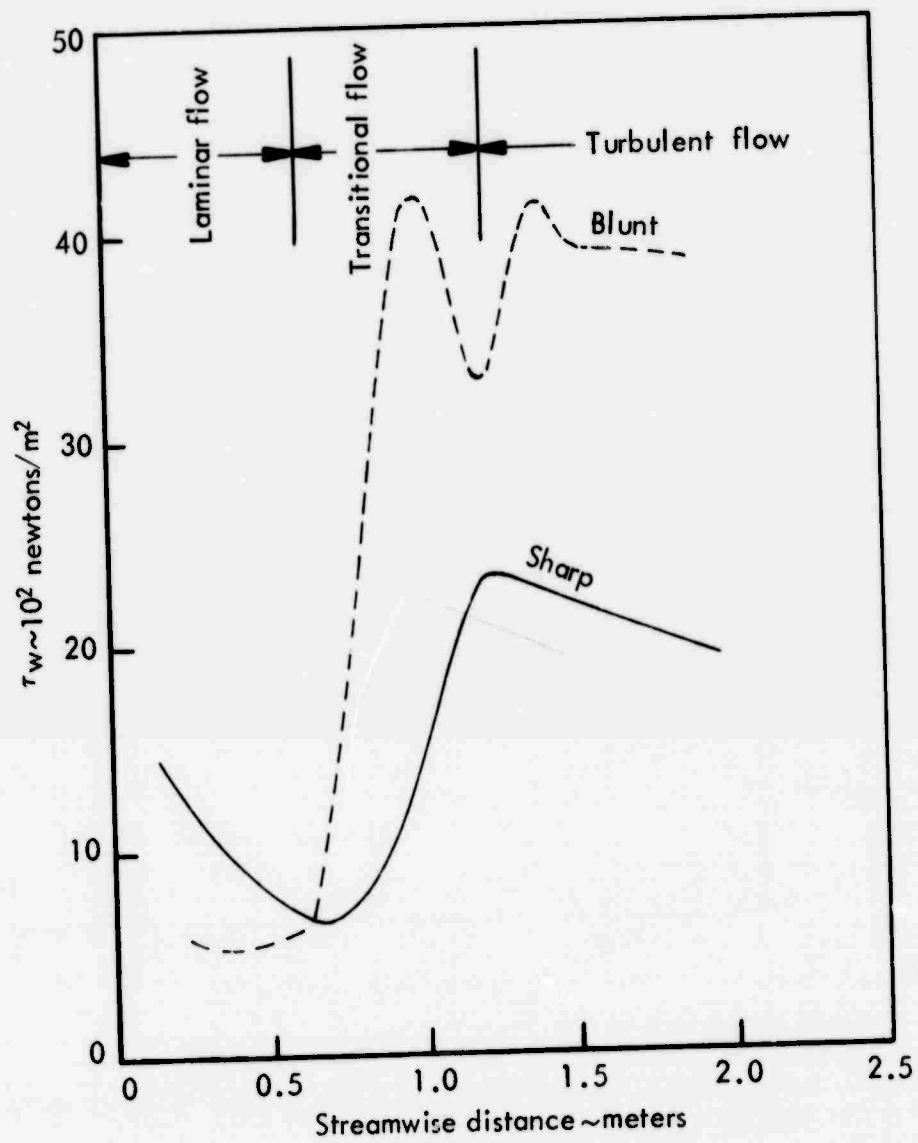


FIGURE 27 WALL SHEAR STRESS COMPARISON, SHARP VERSUS BLUNT CONE

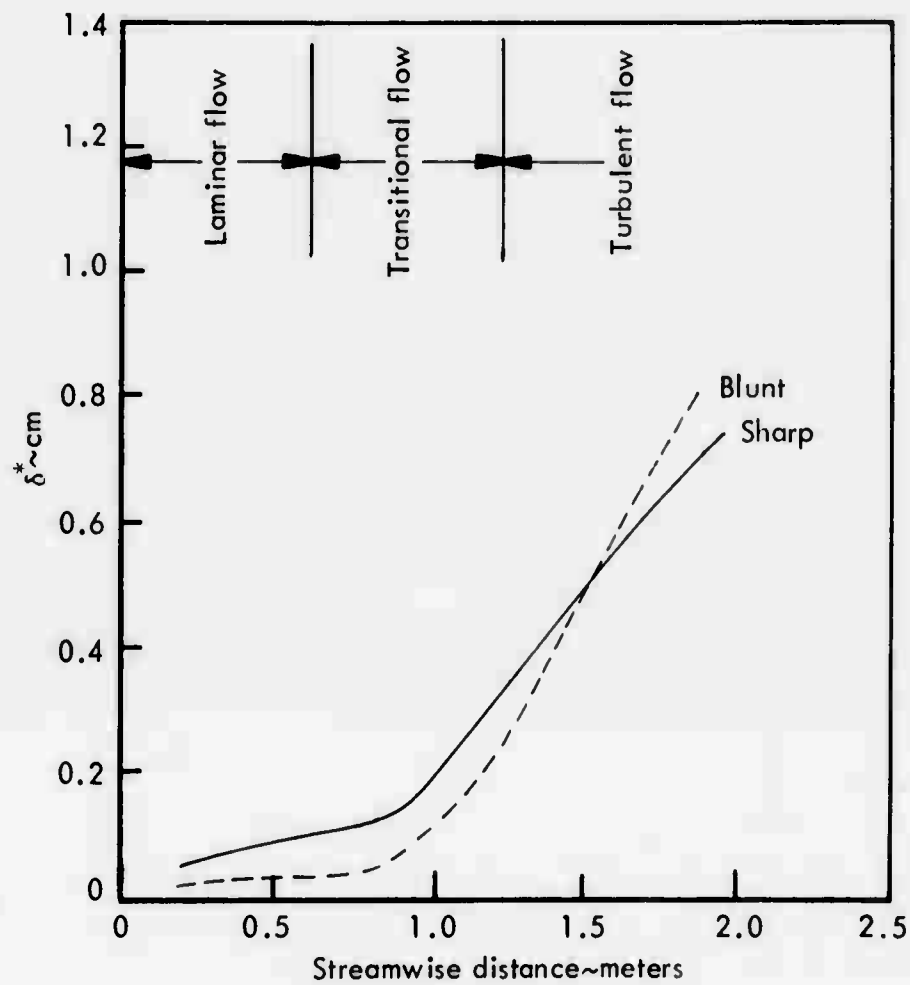


FIGURE 28 BOUNDARY LAYER DISPLACEMENT THICKNESS COMPARISON, SHARP VERSUS BLUNT CONE

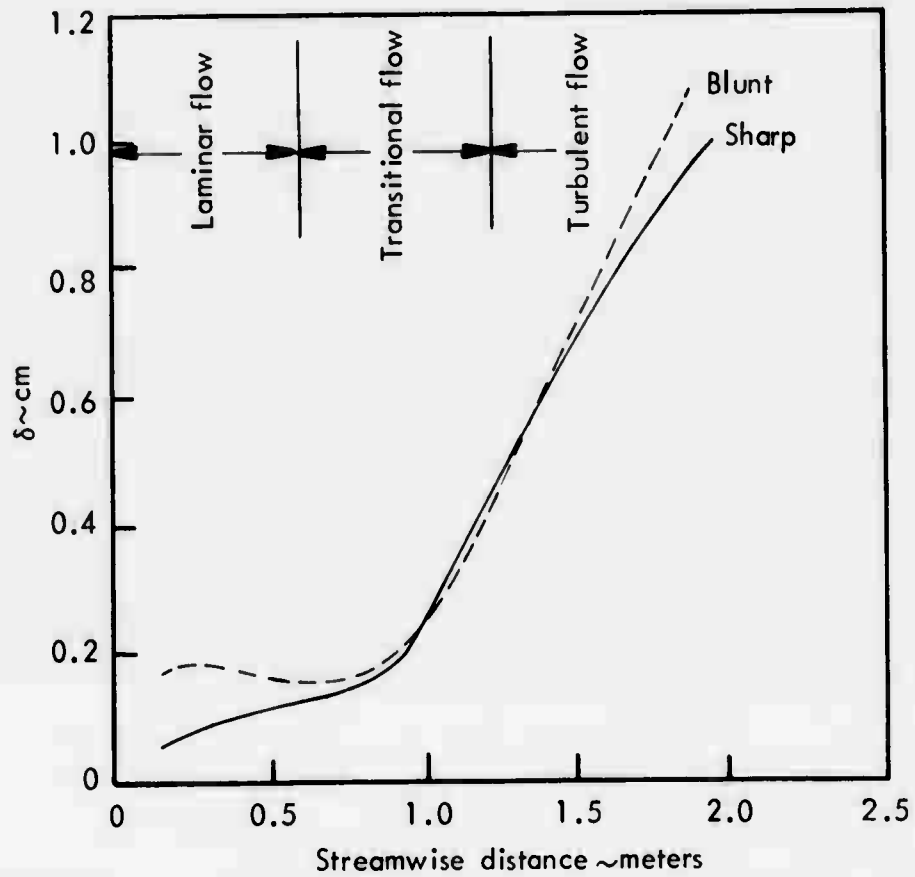


FIGURE 29 BOUNDARY LAYER VELOCITY THICKNESS COMPARISON, SHARP VERSUS BLUNT CONE

2.5 Aerodynamic Forces and Moments

A significant step in assessing the relative importance of transitional boundary layer phenomena on the dynamic behavior of reentry vehicles is to quantify the boundary layer parameters in terms of actual forces and moments acting on the vehicle. The boundary layer displacement effect is manifested as an increase in the pressure on the body which in turn causes changes to the axial and normal forces and pitching moments acting on the body. The skin friction forces also cause changes to the axial forces and pitching moments. A normal force can be associated with the heatshield ablation rate since the finite velocity of the ablation products permeating the surface of the body has an accompanying thrust. It is the purpose of this section to quantify those effects related to boundary layer transition which may be a source of static or dynamic instabilities for reentry vehicles.

The importance of carbon phenolic ablation in producing thicker boundary layers by itself has been addressed above. The concern was that the increased wall mass transfer rates associated with turbulent boundary layer heating may be the cause of significantly thicker boundary layers and corresponding greater induced pressures, independent of the occurrence of transition and the onset of turbulence within the boundary layer. By zeroing out the mass transfer associated with heatshield ablation, it was determined that the onset of turbulence was the principal contributor to increased boundary layer displacement thickness and increases in the induced pressure following transition. The inclusion of wall mass transfer rates associated with carbon phenolic ablation to turbulent heating only added about 10 percent to the boundary layer displacement thicknesses.

The significance of ablation thrust can be addressed using a straightforward approach to the conservation of momentum, which is written as

$$F = \frac{d}{dt} (mv) = v \frac{dm}{dt}$$

where v is the velocity of the ablation products at the wall and dm/dt is the mass flow rate of ablation products at the wall. The mass flow rate for turbulent heating is discussed in Section 2.3 and reaches a maximum of $.176 \text{ kg/m}^2\text{sec}$ on the rear of the cone. Assuming thermodynamic equilibrium of the ablation products at the wall temperature, the velocity of the ablation products is 2.68 m/sec , giving a total ablation thrust of

$$F/A = (.176)(2.68) = .47 \text{ N/m}^2$$

In comparison to the inviscid pressure of 57500 N/m^2 acting on the cone, the ablation thrust of $.47 \text{ N/m}^2$ is indeed small and will hereafter be dismissed.

The boundary layer displacement thickness profiles will be the starting point for definition of the boundary layer-caused induced pressures. The induced pressures will be determined using the full tangent-cone hypothesis, given as

$$\frac{\Delta P}{P_\infty} = \frac{2\gamma}{\gamma+1} (K_s^2 - 1) + \frac{\gamma(K_s - K)^2 (+1)}{\gamma-1 + 2/K_s^2} \quad (74)$$

where $K = M_\infty \beta$, $\beta =$ shock angle

$K_s = M_\infty (\theta_c + d\delta^*/dx)$, $\theta =$ half-cone angle

$d\delta^*/dx =$ boundary layer displacement thickness gradient

K_s and K are related by

$$\frac{K_s}{K} = \frac{\gamma+1}{\gamma+3} + \sqrt{\left(\frac{\gamma+1}{\gamma+3}\right)^2 + \frac{2}{\gamma+3} \frac{1}{K^2}} \quad (75)$$

Using the above equations, the induced pressures caused by boundary layer thickening can be determined. For the blunt cone zero angle of attack calculations for both fully laminar and transitional boundary layer flow, the tangent-cone method produces the induced pressures shown in Figure 30. Keeping in mind that the rearward two-thirds of the body experiences an inviscid pressure of about 57500 N/m^2 , the transitional boundary layer induced pressure is seen to be a significant fraction of this.

We will postulate a highly asymmetrical transition front for the reference body at zero angle of attack in an effort to bound the problem to a certain extent. Assume that one meridian along the body experiences boundary layer transition beginning at the 0.61-meter axial station and that a meridian 180 degrees opposite to the first has completely laminar flow. Between these two extremes the boundary layer induced pressure and shear stress will be defined according to the following distribution

$$\Delta P = \Delta P_{\max} \cos\left(\frac{\phi}{\phi_{\max}}\right) \frac{\pi}{2} \quad (76)$$

$$\Delta \tau = \tau_{\ell} + (\tau_t - \tau_{\ell}) \cos\left(\frac{\phi}{\phi_{\max}}\right) \frac{\pi}{2}$$

where $\phi_{\max} = \pi \left(\frac{x - 0.61}{1.83} \right)$ for $x \geq 2$

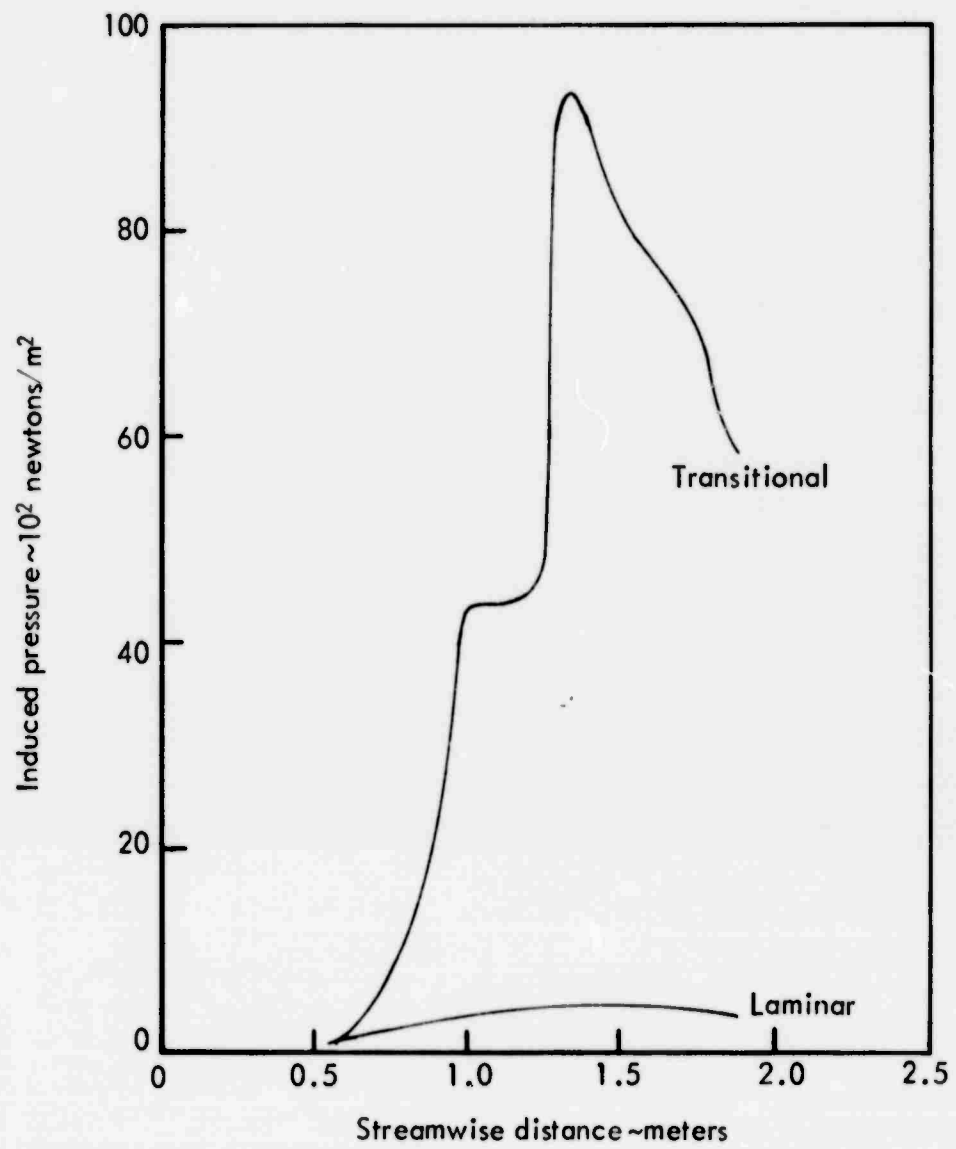


FIGURE 30 BOUNDARY LAYER DISPLACEMENT THICKNESS INDUCED PRESSURE DISTRIBUTIONS

- x = axial station in meters
 τ_t = transitional flow shear stress at x
 τ_l = laminar flow shear stress at x
 ΔP_{\max} = difference between transitional and
laminar induced pressures

The description of ϕ_{\max} above produces the desired transition front which begins along a single meridian at $x = .61$ meters and varies linearly with meridional angle until it reaches the end of the body coincidentally with the $\phi = \pi$ meridian. Outside of this transition region laminar boundary layer values uniformly apply.

Integration of the induced pressures and shear stresses over the body surface is performed to determine the forces and moments acting on the body. The body center of gravity is located at a point 61-percent of the length of the vehicle, which is $x = 1.10$ meters. Using the induced pressure and shear stress distributions given in Equations 76, the following forces and moments results.

Normal force (δ^*)	2086 Newtons
Pitching moment (δ^*)	780 N·m
Pitching moment (τ)	212 N·m

The pitching moments from both sources act in concert and trim the vehicle out at about 1/2 degree angle of attack. Furthermore, the transitional meridian would be pitched up to the leeward side, which is precisely the side favored for transition. Thus the presence of any asymmetry in the transition front is reinforced by the static stability of the vehicle. Additionally, the boundary layer displacement effect is predominant over the shear stress effect.

For the sharp cone angle of attack calculations, the integration of the induced pressures and shear stresses over the entire body is a straightforward operation. The induced pressures are once again determined using the tangent-cone method. The results of the force and moment integrations are shown in Figures 31, 32, and 33 as functions of the angle of attack. Figure 31 portrays the normal force as a function of angle of attack which results from the boundary layer displacement effect. This force acts in a direction opposite to the normal force associated with the inviscid pressure distribution on a cone at angle of attack, and is a consequence of the favored leeward side transition that is postulated. This boundary layer induced normal force is relatively constant until angles of attack above 3-degrees are experienced, where the force begins to increase noticeably. The normal force calculated for a sharp cone at zero angle of attack is approximately one-half the normal force determined above for the zero angle of attack blunt cone.

The variation of pitching moment due to the boundary layer displacement effect as a function of angle of attack is depicted in Figure 32. Once again, this pitching moment is acting in the opposite direction to the inviscid pitching moment due to the leeside favored transition. The zero angle of attack sharp cone pitching moment is about one-half that determined for the blunt cone, and would cause the vehicle to trim at a smaller angle of attack than the 1/2 degree mentioned previously for the blunt cone.

The shear stress pitching moment is shown as a function of angle of attack in Figure 33. At low angles of attack, the shear stress pitching moment acts in concert with the boundary layer displacement effect pitching moment and opposite to the inviscid aerodynamic pitching moment. This direction sense is in agreement

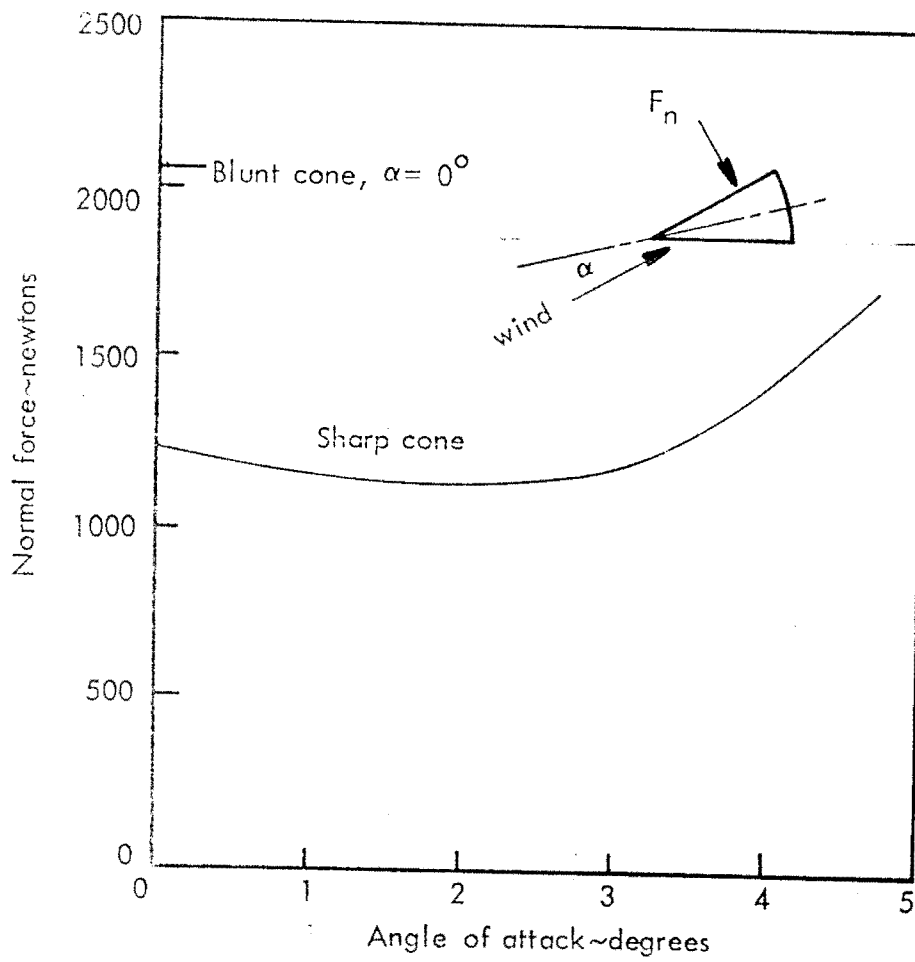


FIGURE 31 BOUNDARY LAYER DISPLACEMENT THICKNESS INDUCED NORMAL FORCE

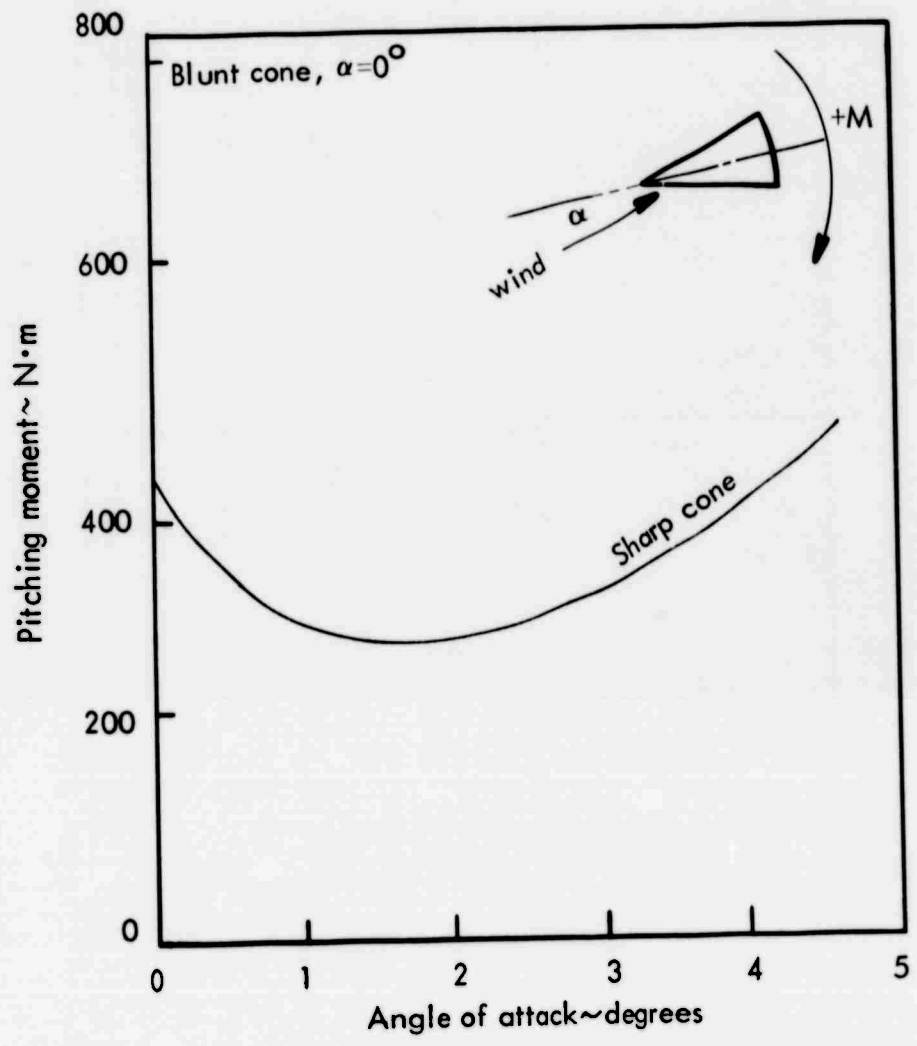


FIGURE 32 BOUNDARY LAYER DISPLACEMENT THICKNESS INDUCED PITCHING MOMENT

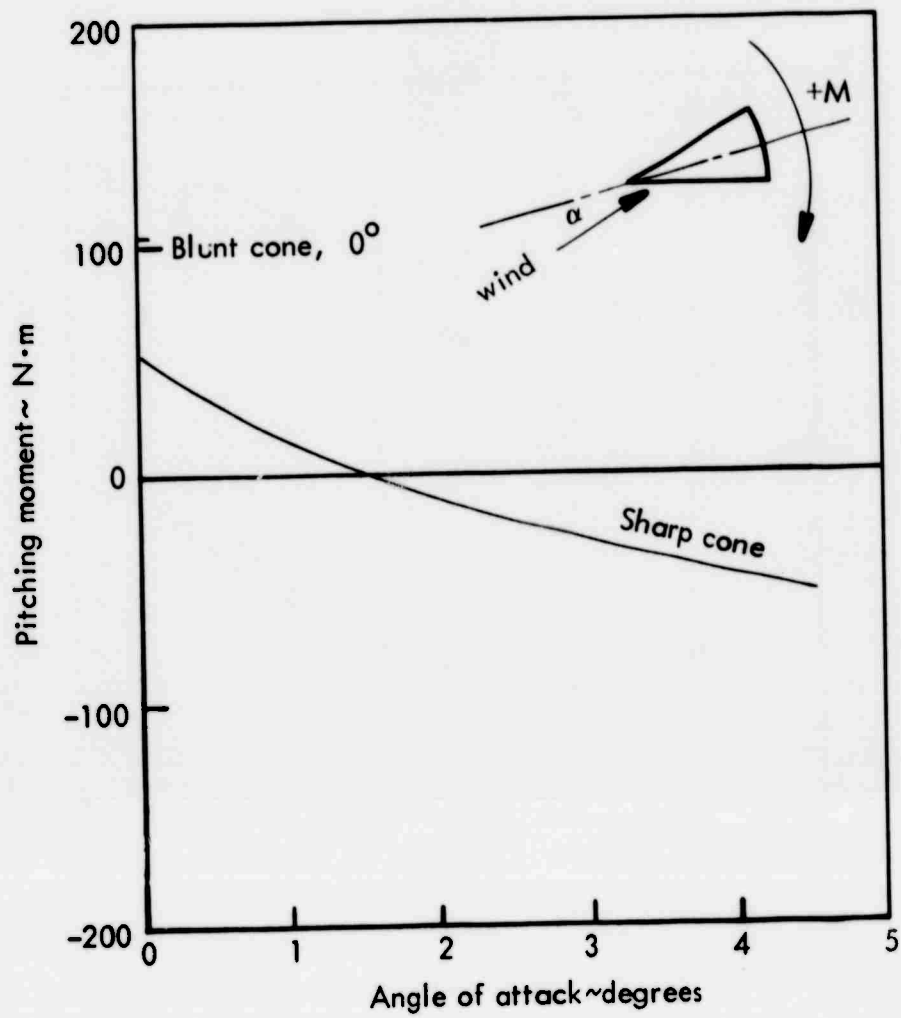


FIGURE 33 WALL SHEAR STRESS PITCHING MOMENT

with the blunt cone zero angle of attack results. At about 1.5-degrees angle of attack, the shear stress moment is nulled out, and above that angle of attack the moment takes the opposite sense of direction. Once again, the displacement effect pitching moment for a sharp cone at zero degrees angle of attack is approximately a factor of four greater than the shear stress moment but both are about one-half the values determined previously for the blunt cone. This latter difference is believed to be due to the differences associated with entropy gradient effects between the two types of solution.

The relative importance of the boundary layer effects in comparison to the inviscid aerodynamic forces and moments can be visualized more effectively in Figures 34 and 35 where the total forces and moments are shown as a function of angle of attack, with and without the contributions due to the sharp cone boundary layer. Some caution should be given to these data since it has been observed that the sharp cone boundary layer effects are about one-half that seen for the zero angle of attack blunt cone. Secondly, while the transition front selected in this analysis was chosen to represent an extreme condition as far as the geometry of the transition front is concerned, it may not represent an extreme as far as the important pitching moment is concerned. For instance, it is apparent from inspection of the induced pressure distribution shown in Figure 30 that a greater moment would result if the induced pressure distribution for transitional flow were moved rearward about .3 meters, providing much greater moment arms about the $x = 1.10$ -meters center of gravity.

Inspection of Figure 35 indicates that asymmetrical boundary layer transition effects on a sharp cone produce a 270-400 N·m decrease in the net pitching moment acting on the vehicle. The inviscid aerodynamic moment (which is

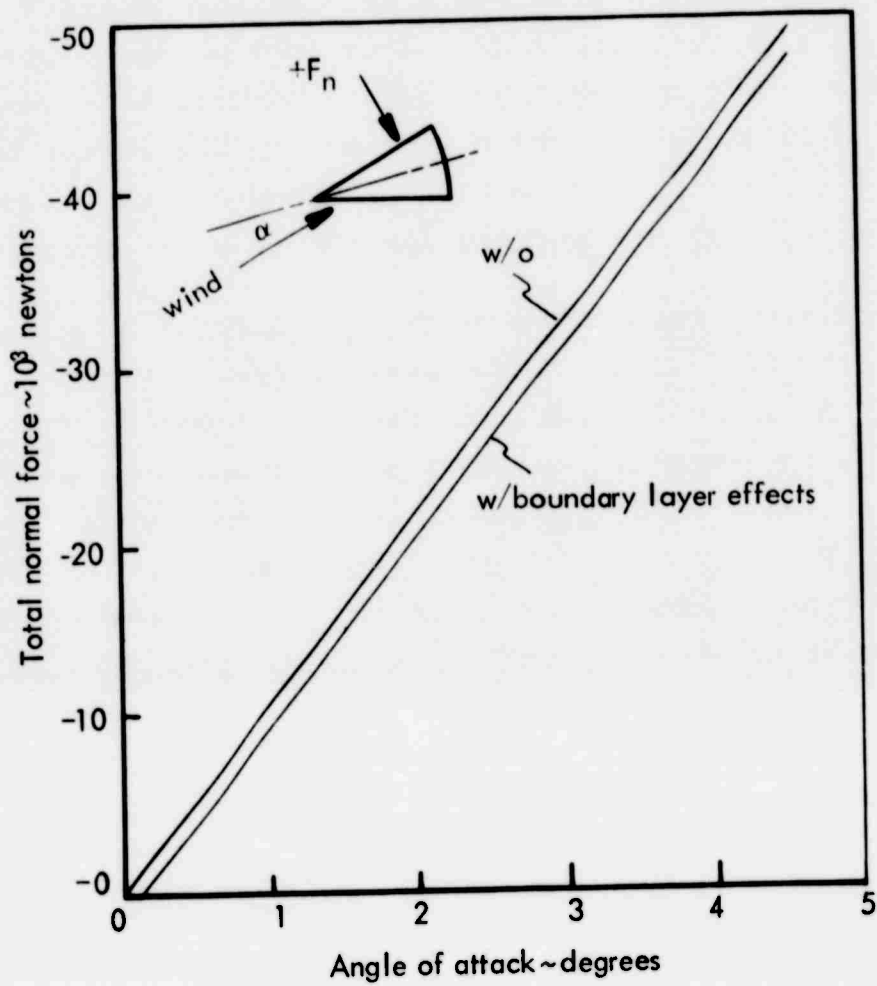


FIGURE 34 TOTAL NORMAL FORCE WITH AND WITHOUT BOUNDARY LAYER EFFECTS

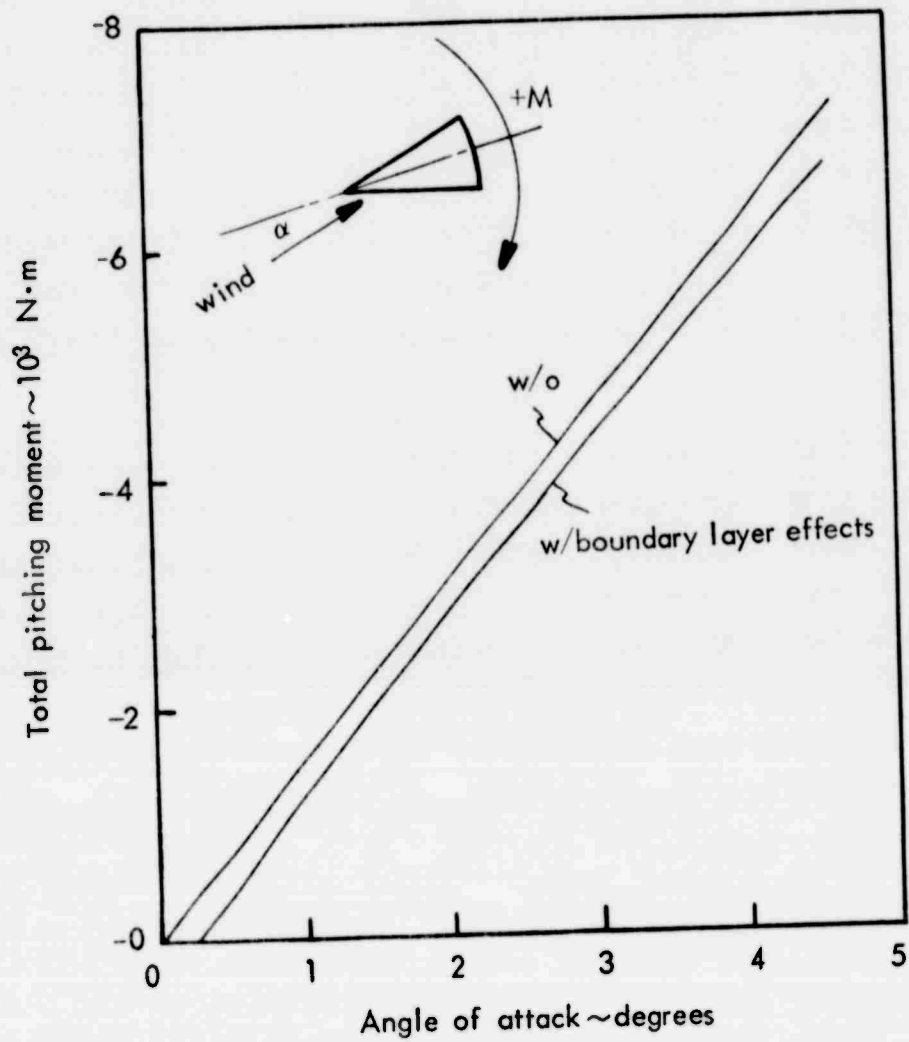


FIGURE 35 TOTAL PITCHING MOMENT WITH AND WITHOUT BOUNDARY LAYER EFFECTS

independent of boundary layer effects) is roughly 1360 N·m per degree of angle of attack. Based upon this comparison of the pitching moment contributions, the sharp cone vehicle shape should be stable above 0.3-degrees angle of attack, at which point the inviscid aerodynamic moment should exceed the destabilizing boundary layer induced moment. Once again, the reader is reminded of the conservatism of the sharp cone boundary layer induced moment of 270-400 N·m. A more realistic maximum destabilizing moment which considers blunt body boundary layer flow and less severe boundary layer transition front asymmetrical geometries is probably in the range of 700-1400 N·m, which raises the angle of attack to achieve stability to 0.5-1.0 degrees.

In conclusion, it must be emphasized that asymmetrical boundary layer effects are important only at small angles of attack, say less than 1.0 degrees, and cannot be significant contributors to the in-plane vehicle aerodynamic characteristics above that point. This would further suggest that if in-plane aerodynamics are the cause of the observed transient reentry vehicle excursions during boundary layer transition, then small angles of attack are required for the development of these excursions.

3.0 BOUNDARY LAYER MEASUREMENTS - SURVEY RESULTS

3.1 Pressure Measurements

Several investigators have reported on experiments in which measurements were made of pressure of the flow field boundary layer on reentry vehicles or wind tunnel models. Some of the more pertinent data and statements concerning sources of measurement inaccuracy are summarized in this section.

The pressure exerted on a reentry vehicle by the viscous flow field exhibits both average (or static) and fluctuating (or acoustic) properties. The measurement of these properties are common excepting for the frequency range over which the properties are measured, i.e. the static pressure is normally considered to be a "steady-state" or "average" value at the moment the measurement value is taken, whereas the fluctuating, r.m.s. (root-mean-square), or SPL (sound power level) is an indication of the rate and depth of change of pressure in a short time interval near the instant of measurement. Figure 36 is a qualitative illustration of pressure properties in the boundary layer.

There is no well-defined distinction to be made between static and acoustic measurements in that the normal static measurement implies a data bandwidth especially in a reentry environment. In wind tunnel tests, where supply pressure can be held steady, a low bandwidth can be applied. Acoustic measurements are usually qualified as having a low and a high frequency cutoff. The low frequency end may overlap considerably what is normally regarded as a static measurement band e.g. 10 to 1000 Hz.

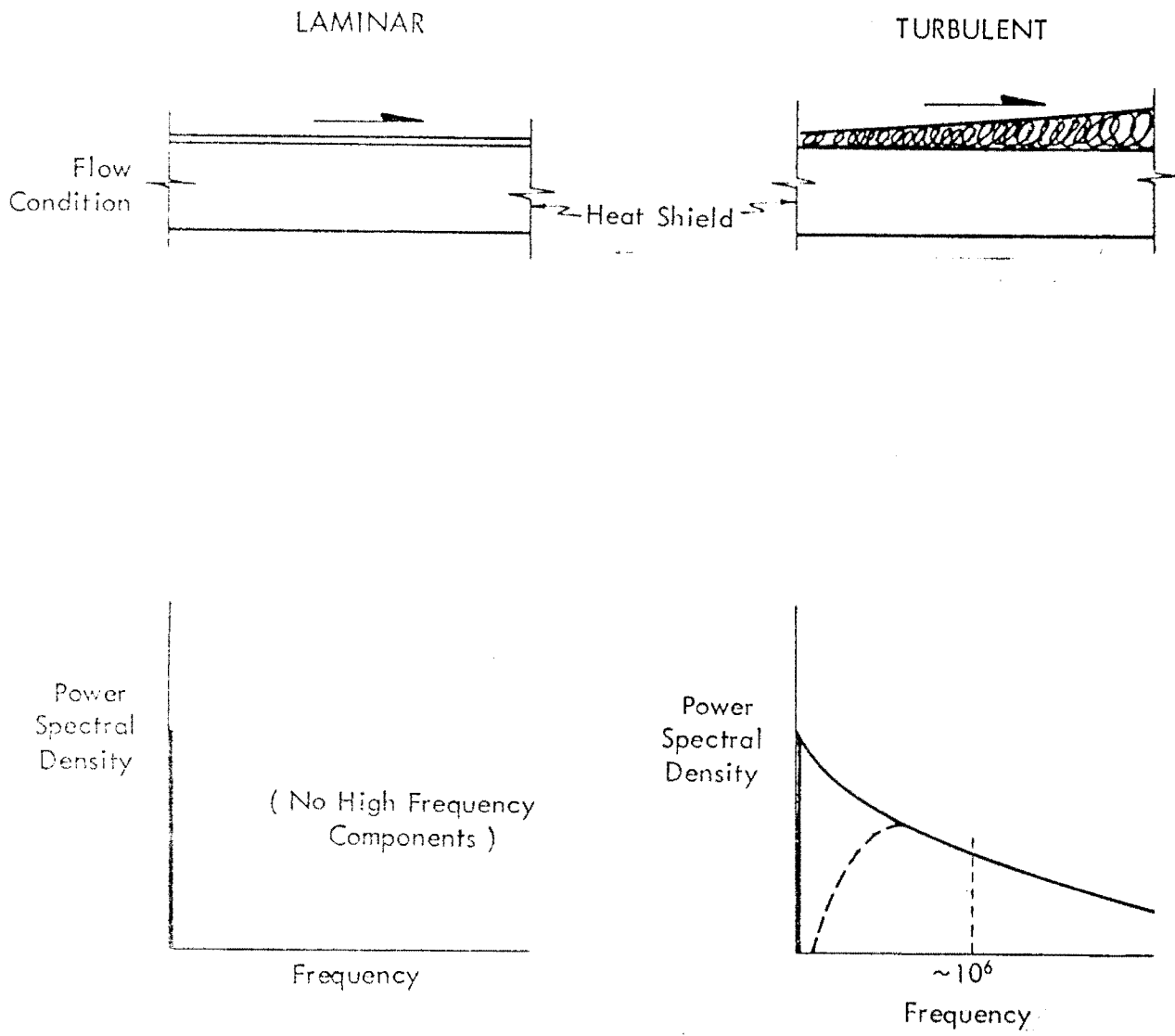


FIGURE 36 FLOW CHARACTERISTICS

Several factors contribute to the inaccuracy of pressure measurements, including:

- 1) Transducer size and shape
- 2) Port aerodynamic and erosion effects
- 3) Temperature environments
- 4) External noise interferences.

3.1.1 Transducer Size and Shape

The results of an investigation into the effects of transducer size, shape and surface sensitivity were reported by White (Reference 29) in 1967; he referenced earlier work by Corcos after whom is named the correction at high frequencies for large diameter transducers. The Corcos correction results from the random character and short correlation lengths of pressure fluctuations in the boundary layer. Figure 37, extracted from Reference 29, shows that high frequencies are attenuated significantly by larger diameter transducers; flow conditions are also significant in this correction and convection velocity should be computed for each application. Shape and surface sensitivity are also to be corrected for in measurements of the high frequency pressure components. The effect of non-uniform surface response (e.g. an edge clamped diaphragm) effectively reduces the transducer diameter with respect to the Corcos correction factor.

Lewis and Dods (Reference 30) completed a series of wind tunnel experiments with 11 flush-mounted transducers of different types and manufacturers. Data were obtained at three tunnel Mach numbers and plotted as shown in Figure 38. Their comments on the data were that size effects dominated the low frequency end of the spectrum, smaller diameters yielding higher power

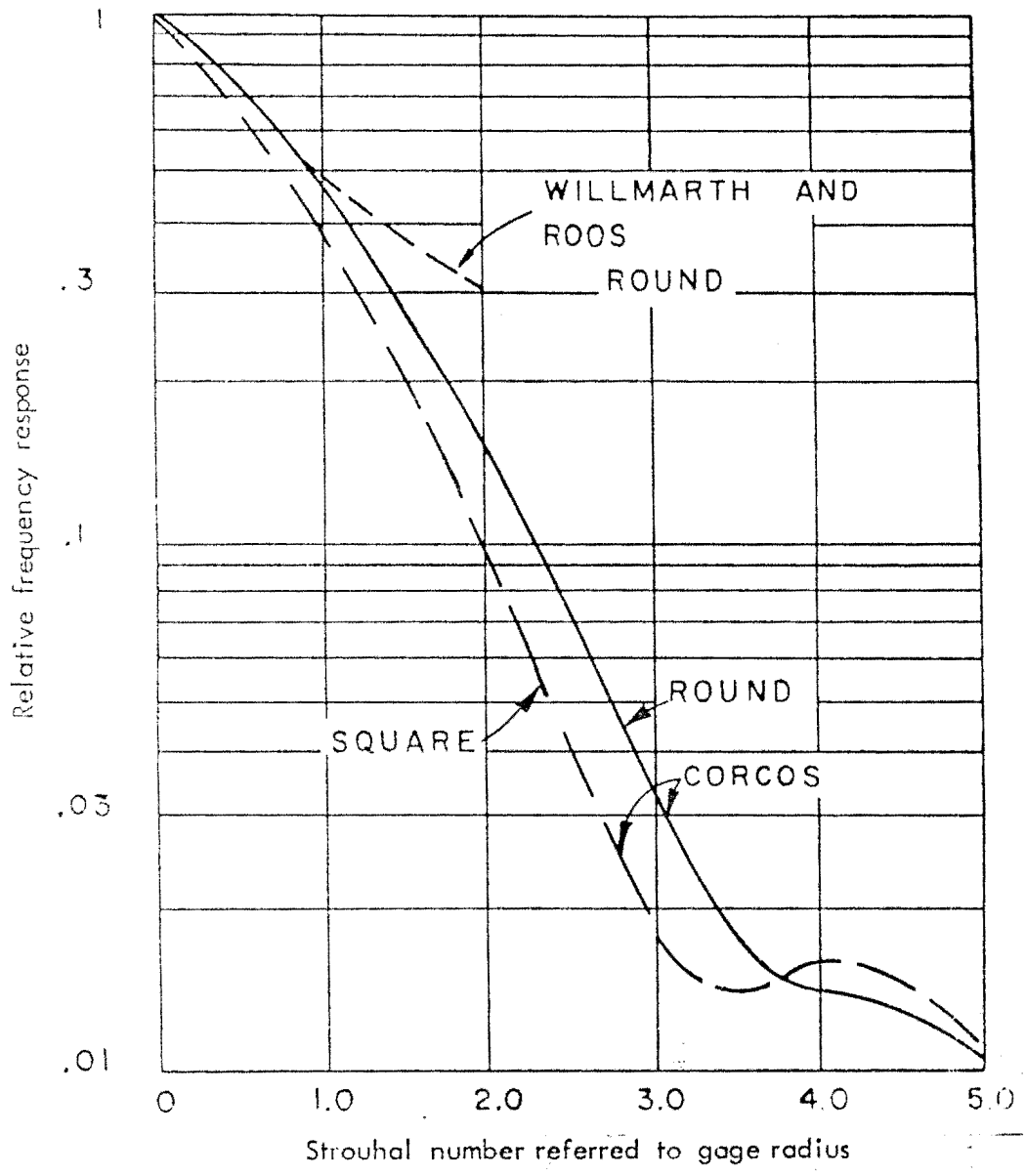


FIGURE 37 THEORETICAL SIZE CORRECTION FACTOR FOR UNIFORM TRANSDUCER RESPONSE
(REFERENCE 29)

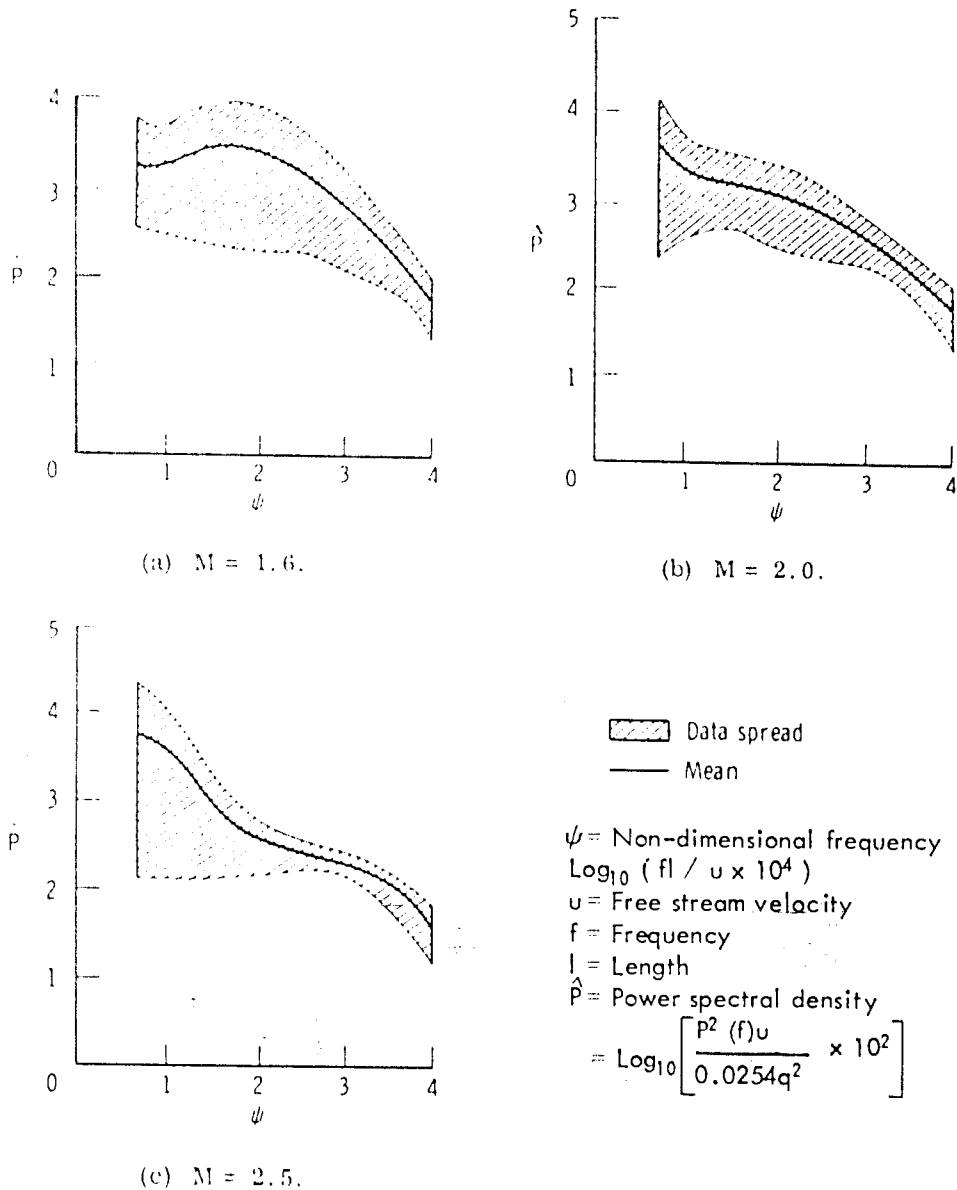


FIGURE 38 VARIATIONS IN THE ESTIMATED POWER-SPECTRAL-DENSITY MEASUREMENTS OF THE SURFACE-PRESSURE FLUCTUATIONS AS DETERMINED FROM 11 DIFFERENT TRANSDUCERS (REFERENCE 38)

spectral density levels at all frequencies than larger diameters. Transducer mounting and system noise levels were ruled out and uncertainties were attributed to some undefined surface pressure fluctuation-transducer interaction. This conclusion implies potential errors may be encountered with a static pressure measurement, even with restricted bandwidth.

3.1.2 Port Aerodynamics

A small diameter tube or port connecting the flow field to the sensor has been applied by many researchers to separate the sensor from the boundary layer environment. The port, however, introduces some additional effects which cause the measured pressure to be in error. Heller and Widnall (Reference 31) found that the high frequency response with flow is increased over that for no external flow, the change depending on flow field parameters; the data presented, however, was not conclusive and was limited to 7 kHz maximum frequency.

Johnson and Macourek (Reference 32) made measurements with ported, flush, and back-surface transducers in a wind tunnel at $M_0 = 4$. Their data showed that noise in the boundary layer increased during transition and diminished immediately after but continued to increase as tunnel pressure was increased; data were taken up to 20 kHz. They noted that acoustic detection of transition is consistent with thermal methods. Differences between ported and flush-mounted transducer data at low frequencies were attributed to tunnel noise.

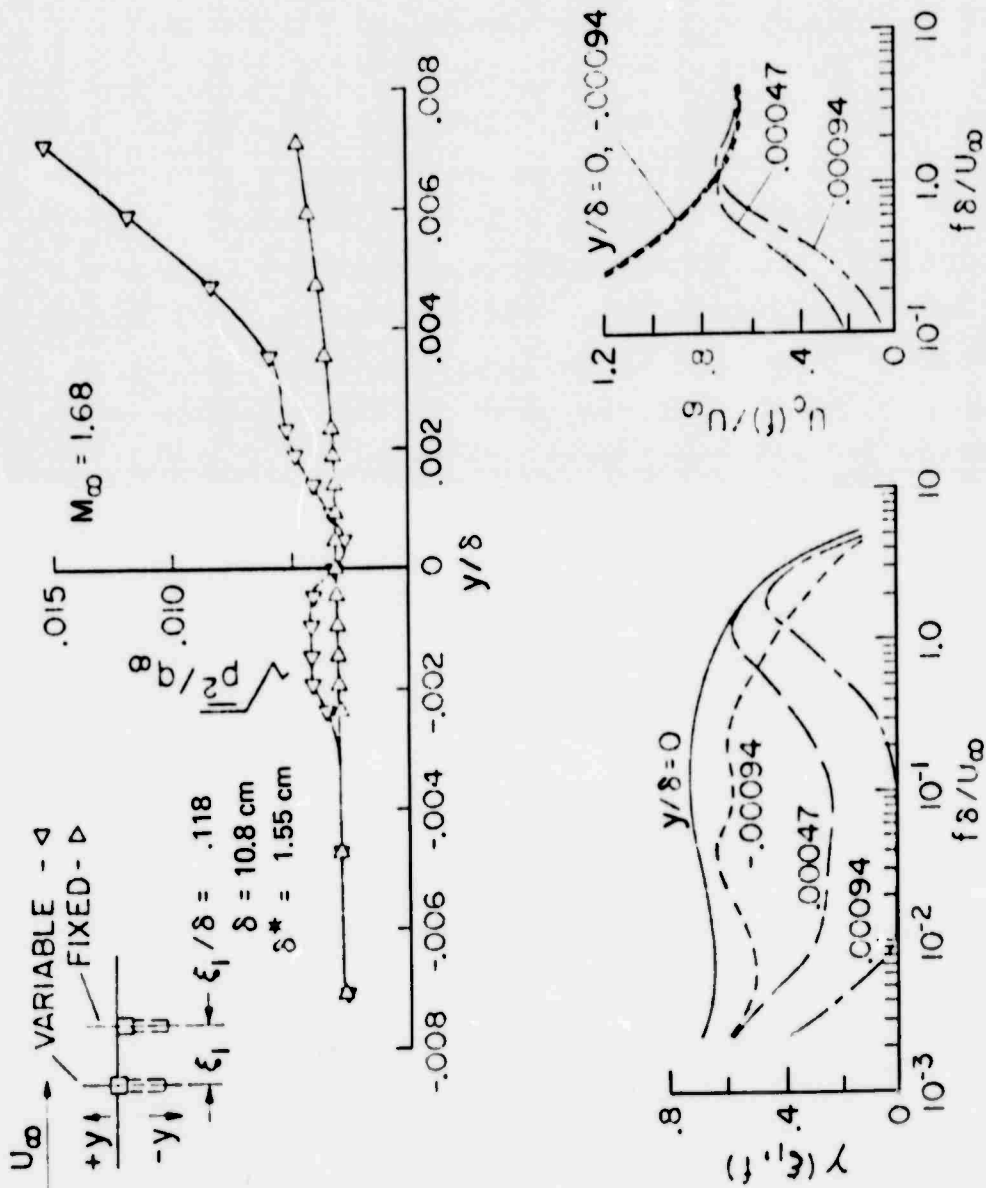
By using flush transducers for reference, Franklin and Wallace (Reference 33) measured the correction required in ported static measurements in wind tunnels, using extreme care to machine the edges of the holes. They state that even if a hole is near-perfect, a residual error remains due to local

changes in boundary conditions and consequent disturbance of the boundary layer.* By referencing their data to the wall shear stress, they obtained a consistent error curve which also included the tunnel flow conditions; their data are shown in Figure 40. It should be noted that the error, e , relative to the shear stress is very large but smaller in relationship to the body pressure which may be an order-of-magnitude or more greater than the shear stress.

Cassanto has reported on wind tunnel and flight test experiments using ported gages (References 35, 36, 37, and 38). His data showed that transition is detectable but depends to a certain extent on the geometry of the transducer mount. Figure 41 illustrates different pressure signatures obtained by different port geometries in a wind tunnel environment. Cassanto postulates that this discrepancy could possibly be attributed to model misalignment. Earlier investigations (Reference 32) have revealed that porting and porting geometry effects both the spectral density and the total pressure measured in a wind tunnel environment (Figures 42 and 43). Cassanto also investigated port erosion effects in a rocket exhaust facility and showed that eroded ports record 15 to 30 percent lower pressures than non-eroded ports. He also suggested a layered disk arrangement to reduce port erosion effects in an ablation environment.

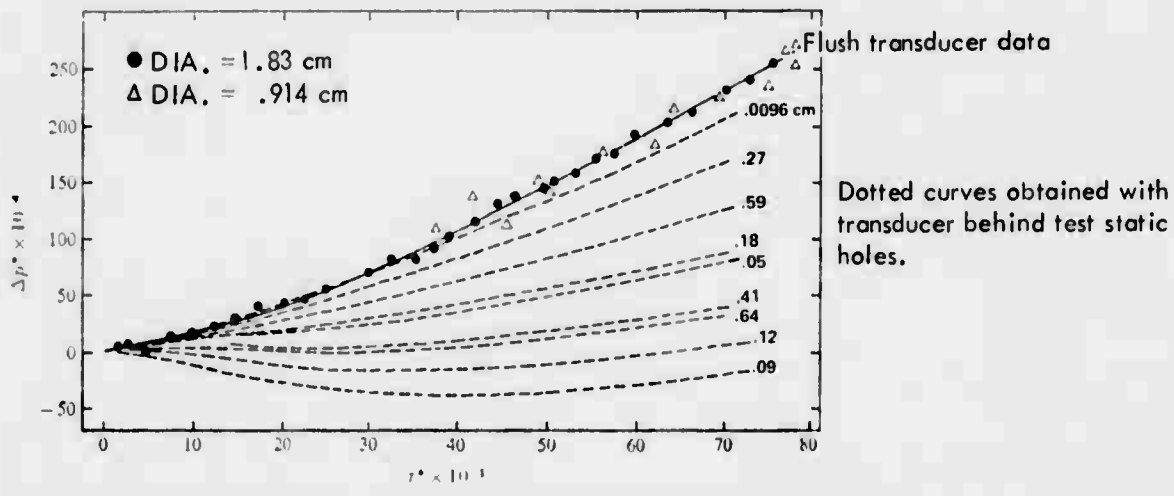
Pressure measurements on flight test reentry vehicles have been partially successful using ported gages. Data shown in Figure 44 show ported sensors responded to transition but

* Coe, in Reference 34, reinforced this observation in a discussion on transducer "flushness" by stating that very small discontinuities on the order of $y/\delta \leq \pm 0.001$ significantly affected rms intensities as well as coherence and convection-velocity measurements (see Figure 39).

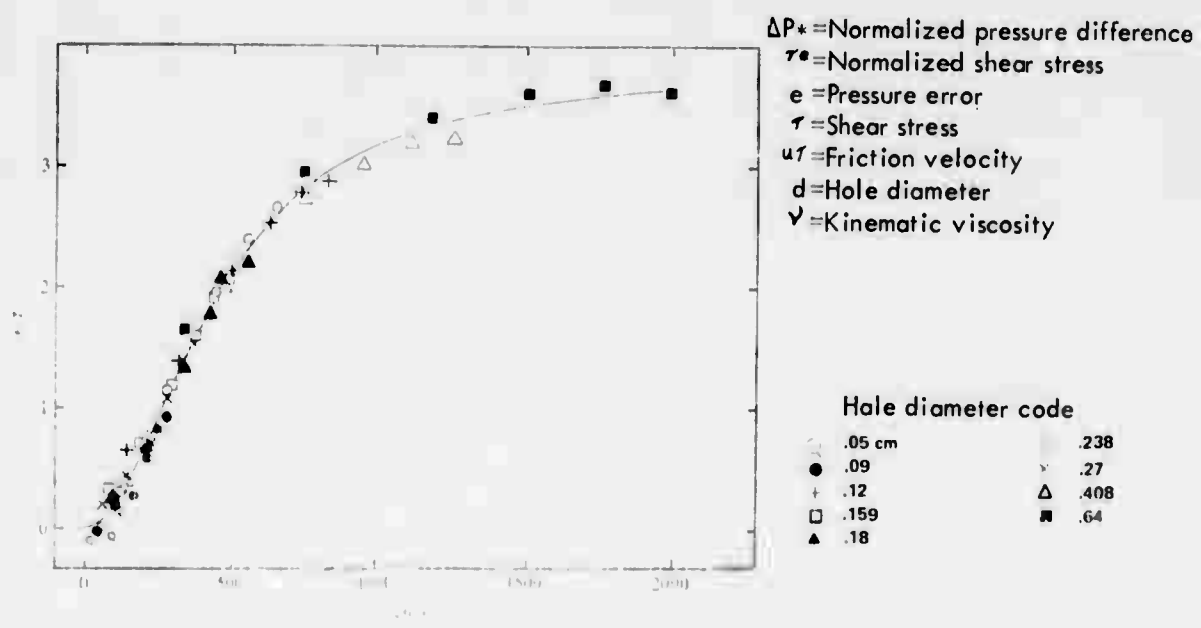


U_∞ = Free stream velocity
 U_c = Convection velocity
 P = R.M.S. pressure fluctuations
 Q_∞ = Free stream dynamic pressure
 $\gamma(\xi_1, f)$ = Coherence between two sensors separated by ξ_1 .
 δ = Boundary layer thickness

FIGURE 39 EFFECT OF THE FLUSHNESS OF A TRANSDUCER MOUNTING ON THE MEASUREMENT OF WALL PRESSURE FLUCTUATIONS (REFERENCE 34)



a) PRESSURE DROP DATA OBTAINED WITH FLUSH TRANSDUCERS



b) NON-DIMENSIONAL ERROR CURVE

FIGURE 40 STATIC HOLE PROPS BOUNDARY LAYER PRESSURE MEASUREMENTS (REFERENCE 5)

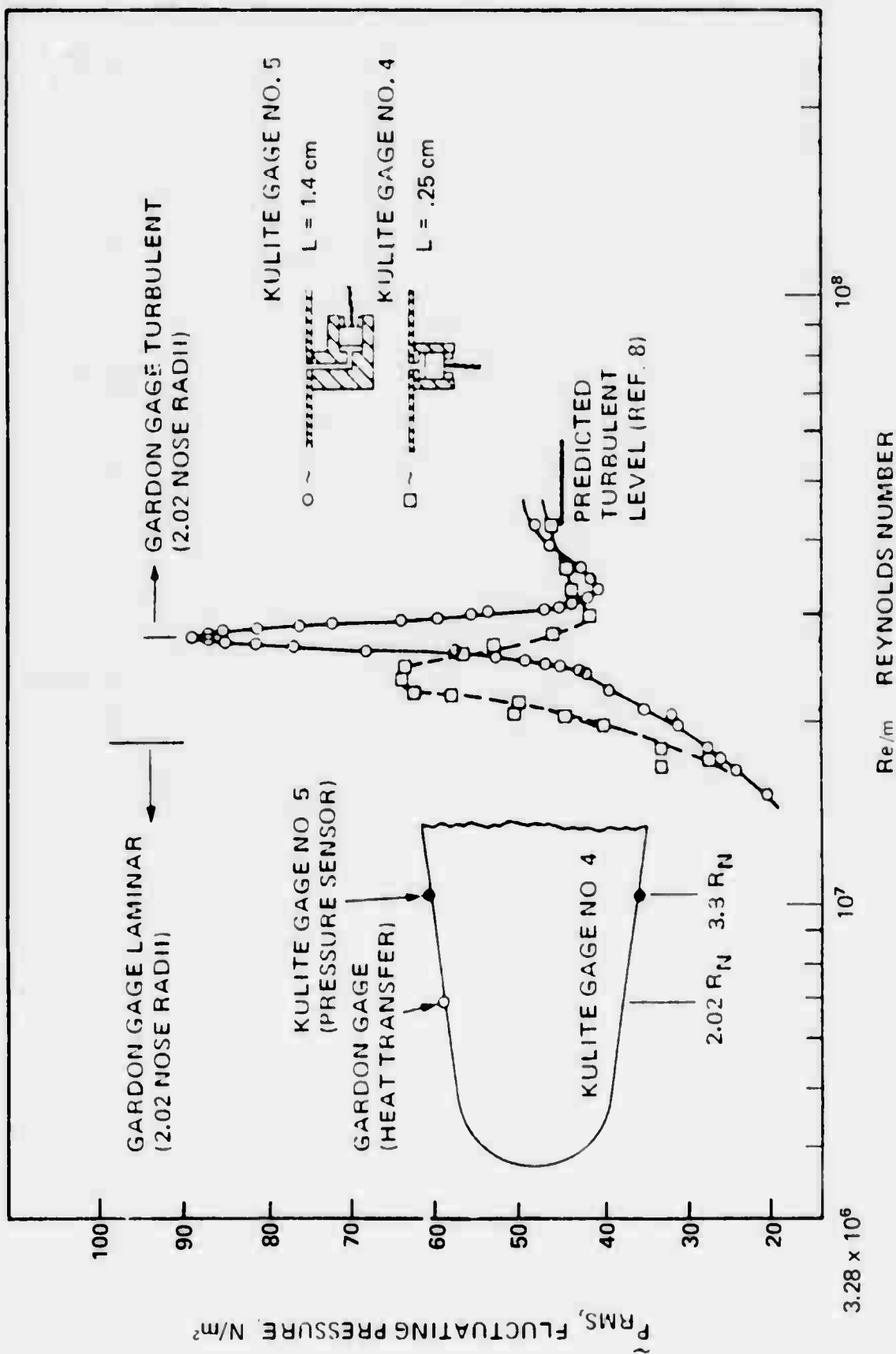


FIGURE 41 COMPARISON OF FLUCTUATING PRESSURE DATA FROM THE SHORT AND LONG PORT AT 3.3 NOSE RADII (REFERENCE 35)

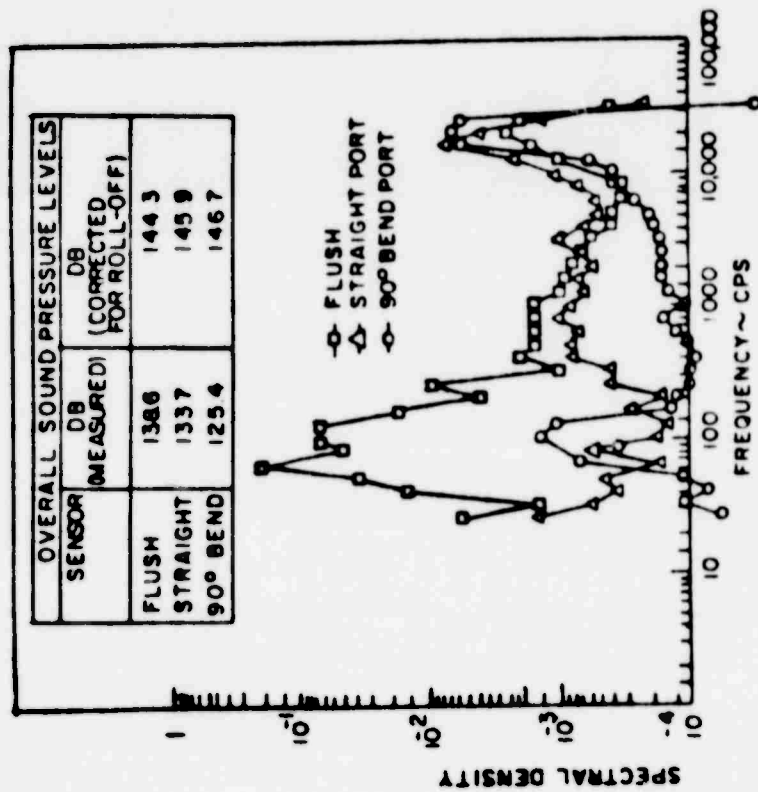


FIGURE 42 POWER SPECTRAL DENSITY
 (REFERENCE 32)

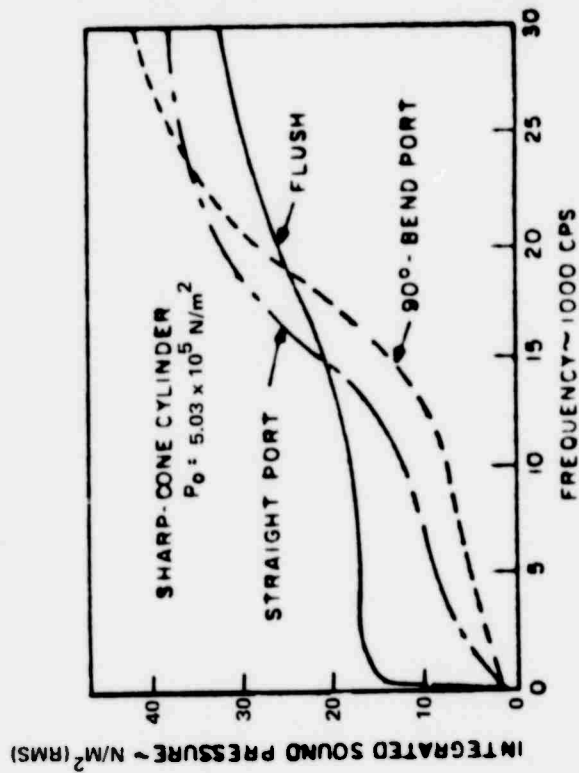


FIGURE 43 INTEGRAL SOUND PRESSURE LEVELS
 (REFERENCE 32)

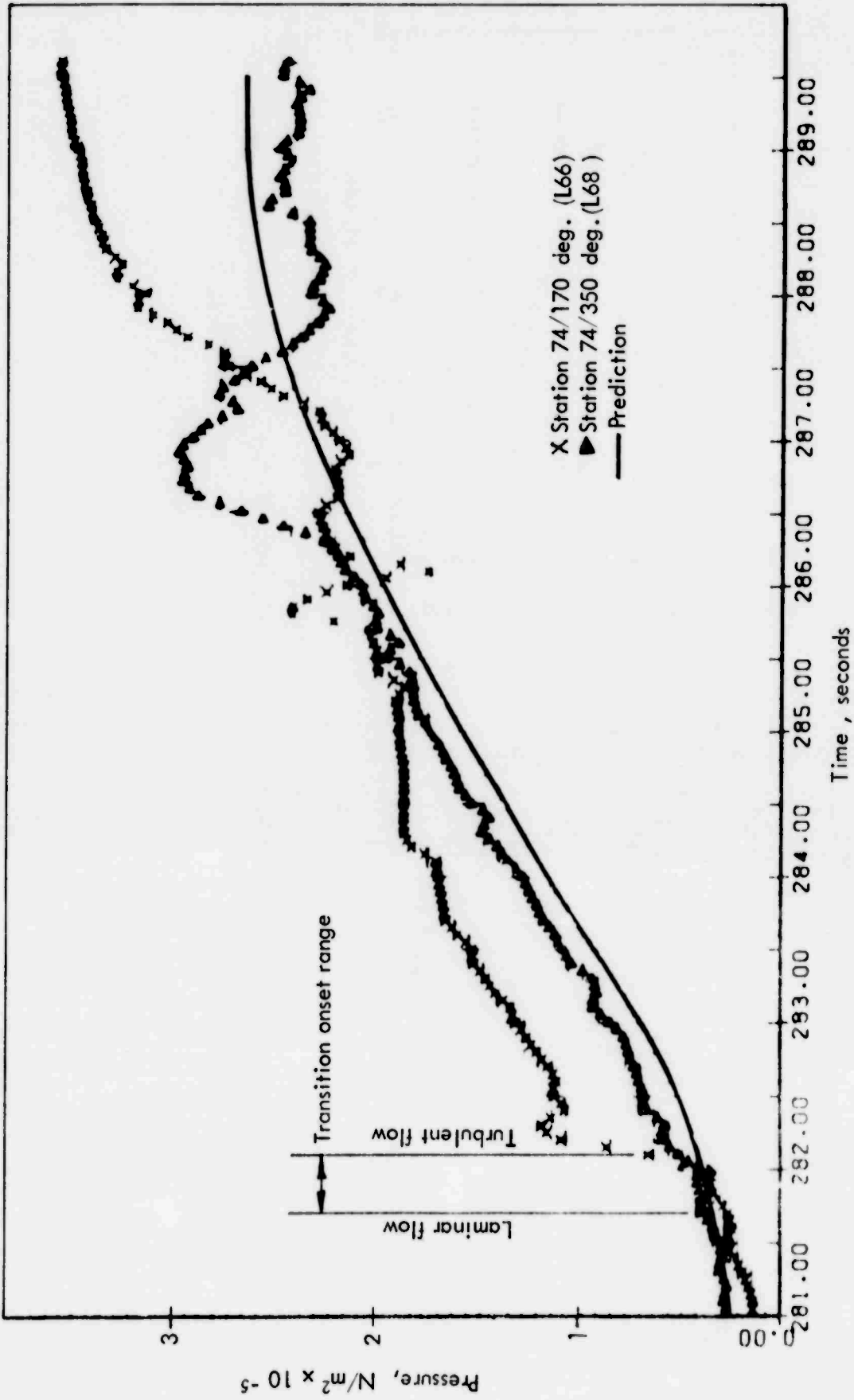


FIGURE 44 PORTED GAGE MEASUREMENT, FLIGHT TEST (REFERENCE 39)

produced anomalous results thereafter (Reference 39). In another flight test (with a different reentry vehicle) results down to transition followed predictions, but were also anomalous thereafter; Figure 45 shows these data (Reference 39). These data also indicate discrepancies which can arise between identical ports on the same reentry vehicle.

Flight data obtained with different port geometries on the same flight show a marked difference in the pressure signatures at onset of transition (Figure 46).

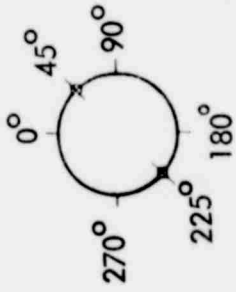
3.1.3 Temperature Environments

In wind tunnel tests, boundary layer gas temperatures approach the plenum temperatures; the model will approach the same temperature in a long test period. Typical temperatures encountered range from 480°K to 1100°K ; thus sensors mounted flush with the surface will encounter transient temperature effects which cannot be calibrated in the transducers presently available from vendors. This source of error was not discussed in the reports covered in the survey.

Errors of this type will potentially be even larger during flight tests where much larger temperature gradients are encountered.

3.1.4 External Noise Interference

All pressure measurements in wind tunnels are made in high level noise environments due to the noise generated by turbulence or tunnel walls or other disturbances upstream from the test model. Reshotko (Reference 40), Kendall (Reference 41) and Beckwith (Reference 42), Owen (Reference 43) and Harvey (Reference 44) separately addressed the influence of tunnel noise on transition in the boundary layers of test models.



SYM	RANGE	ϕ	STATION
o	$0 - 6.9 \times 10^5 \text{ N/m}^2$	45°	59.52
□	$0 - 6.9 \times 10^5 \text{ N/m}^2$	225°	59.52

— $\alpha = 0^\circ$ PREDICTION } REFERENCE 4
 I $\alpha = +1^\circ$ PREDICTION }

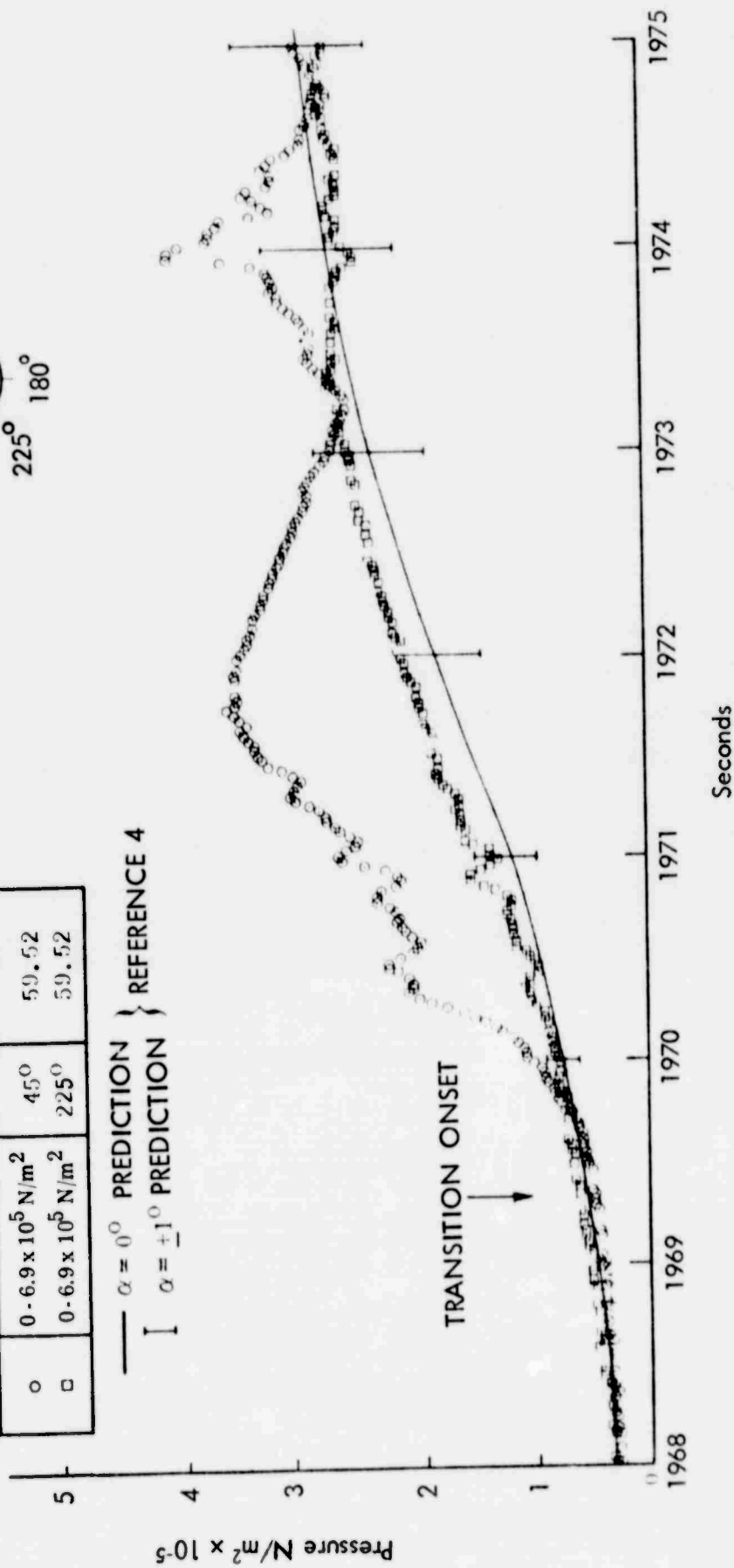
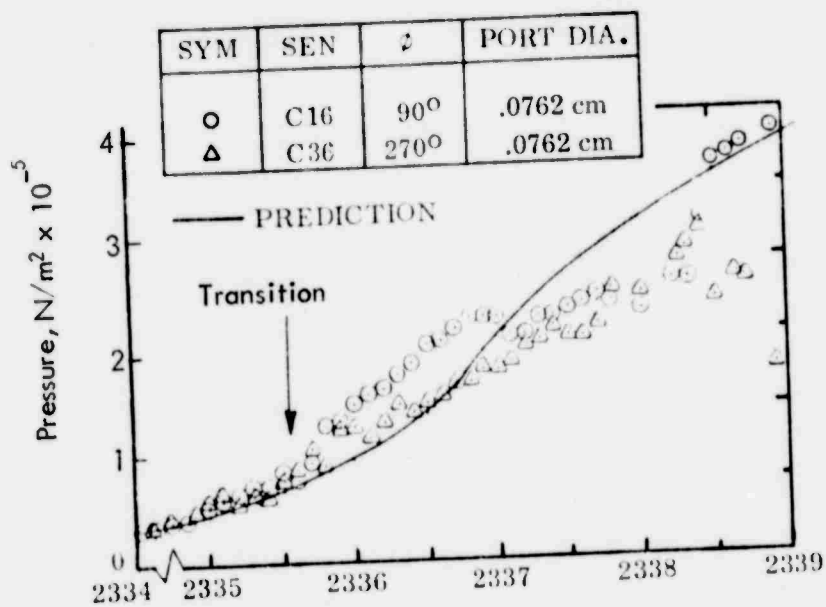


FIGURE 45 PORTED GAGE MEASUREMENTS (REFERENCE 39)



NOTES:

SYM	SEN	ϕ	PORT DIA.
○	C18	135°	.152 cm
△	C38	320°	.152 cm

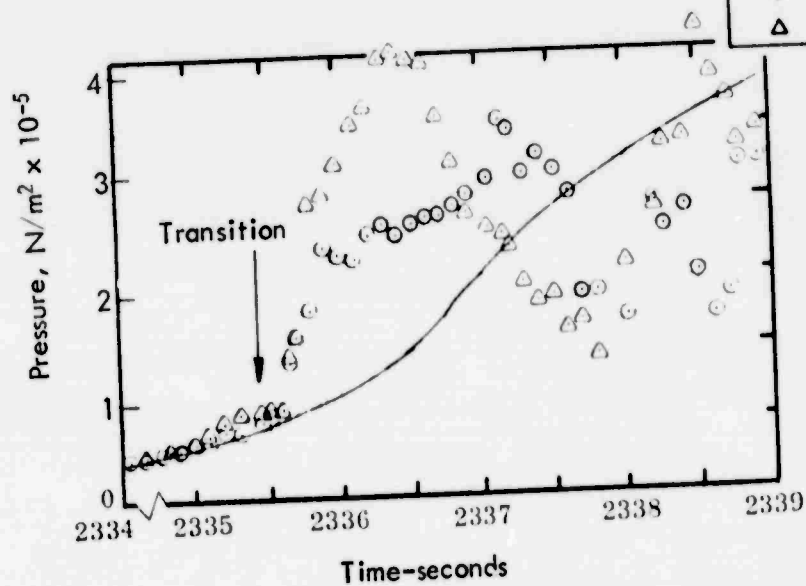


FIGURE 46 PORTED GAGE MEASUREMENTS, FLIGHT TEST (REFERENCE 39)

There was agreement that wind tunnel noise is of such a magnitude as to be the predominant factor in transition on test models. Pitot measurements by Harvey (Reference 44), et al at $M_\infty = 5$ showed that background fluctuation levels reached as high as 3% of p_∞ with frequency components out to 250 kHz; Figure 47 is extracted from his report. Typical boundary layer noise levels range from 0.2 to 1% of p_∞ .

The principal reason for citing the above is to illustrate that wind tunnel test data of boundary layer noise must be corrected for the high background level or erroneous interpretation may result. Also, in very noisy tunnels wherein pressure sweeps are used to facilitate transition measurements, turbulence may be initiated erratically and provide apparently anomalous results. Figure 48 (Reference 42) illustrates sources of noise in wind tunnels and Figure 49 (Reference 42) shows that boundary layer noise was significantly larger due to turbulence only at a peak near 60 kHz while tunnel noise dominated below 30 kHz.

3.2 Temperature Measurements

Classical definitions of transition evolved from temperature measurements of wall temperature and surface heating rates. Using thermocouples either singly to obtain wall temperature, or differentially in pairs to obtain heating rate, data are plotted versus distance or versus Re_∞ on conical or inclined flat plates and certain features are then identified which are related to transition. Recent plots by three investigators are shown in Figures 50, 51, and 52; these data were presented by Owen (Reference 43), Demetriades (Reference 45) and Martellucci (Reference 46) respectively.

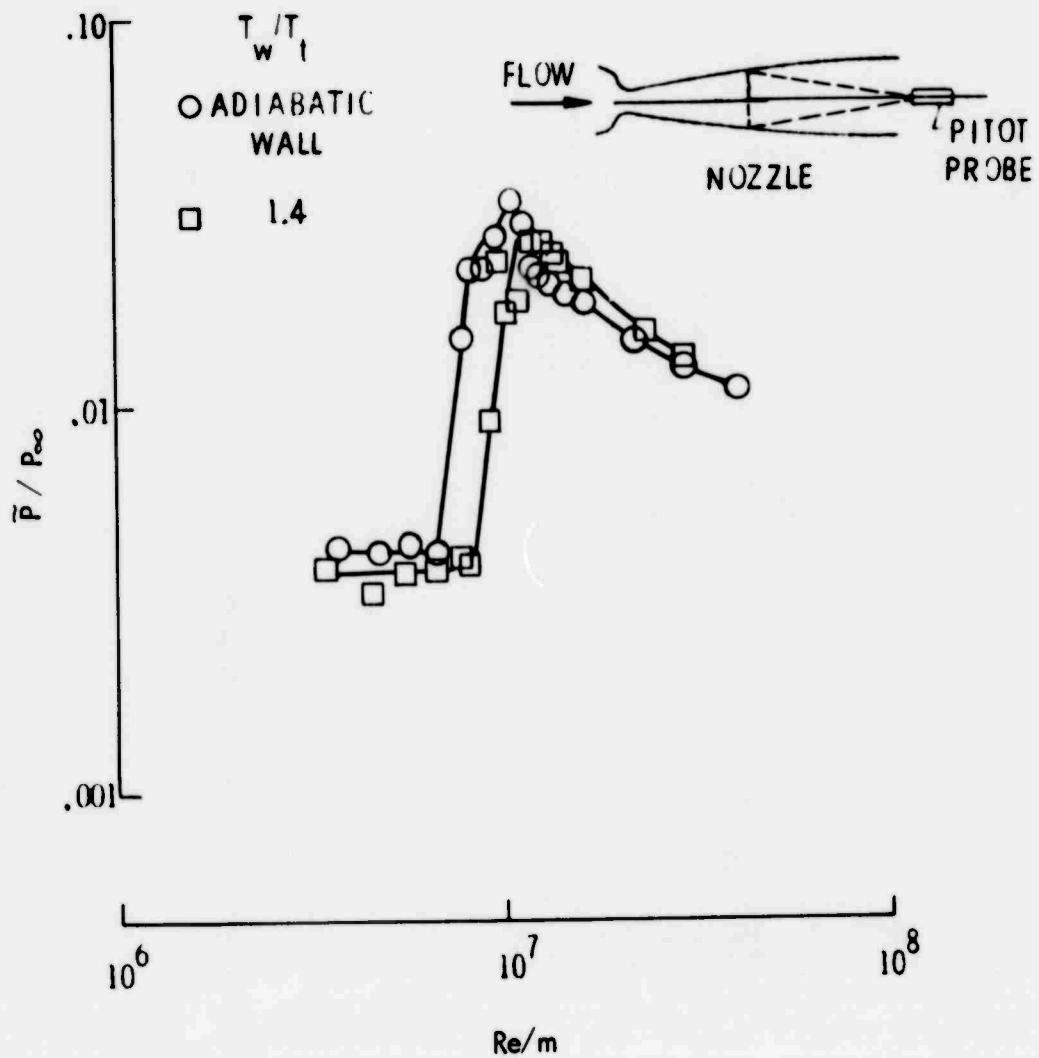


FIGURE 47 EFFECT OF NOZZLE WALL TEMPERATURE ON DISTURBANCE LEVELS IN FREESTREAM (REFERENCE 44)

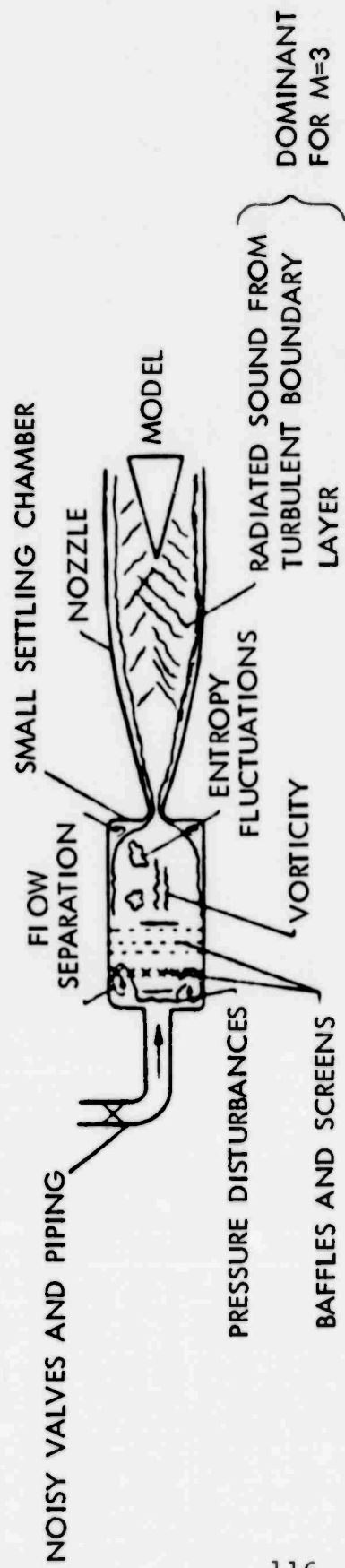
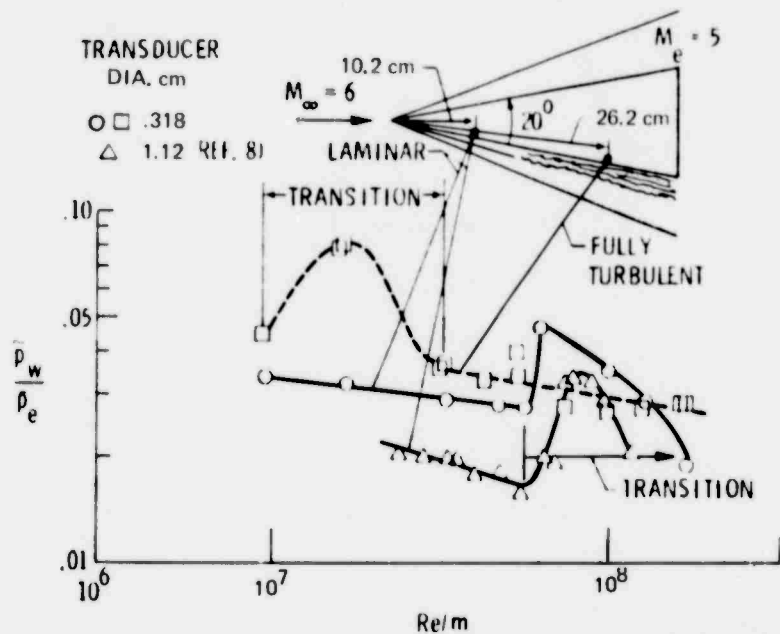
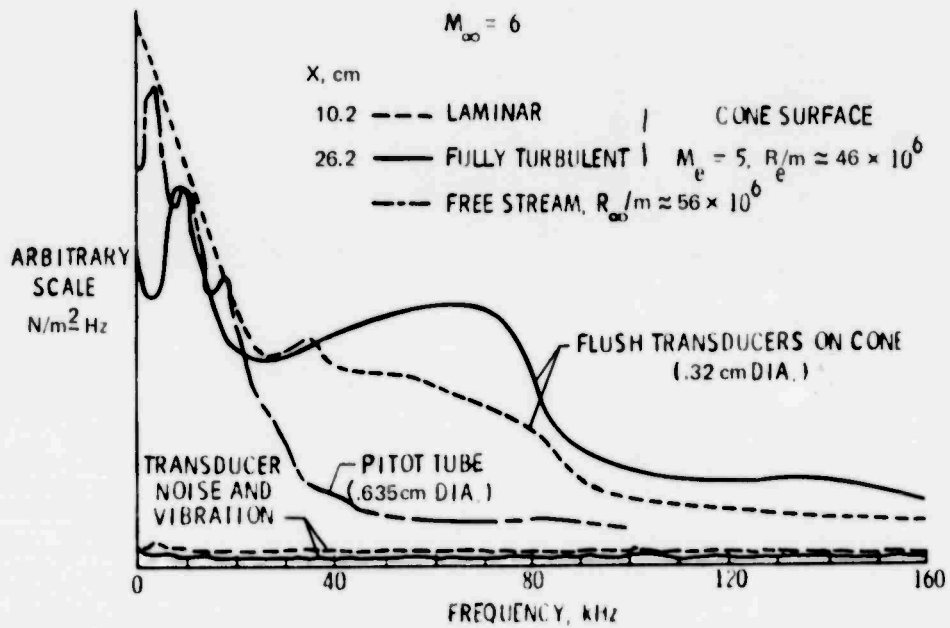


FIGURE 48 SOURCES OF NOISE IN WIND TUNNELS (REFERENCE 42)



a) VARIATION OF OVERALL RMS PRESSURE WITH UNIT REYNOLDS NUMBER



b) SPECTRA OF PRESSURE FLUCTUATIONS WITH $\Delta f = 200 Hz$

FIGURE 49 MEASUREMENTS OF FLUCTUATION PRESSURES UNDER LAMINAR AND BOUNDARY LAYERS ON A SHARP CONE IN MACH 6 HIGH REYNOLDS NUMBER TUNNEL AT NASA LANGLEY- (REFERENCE 42)

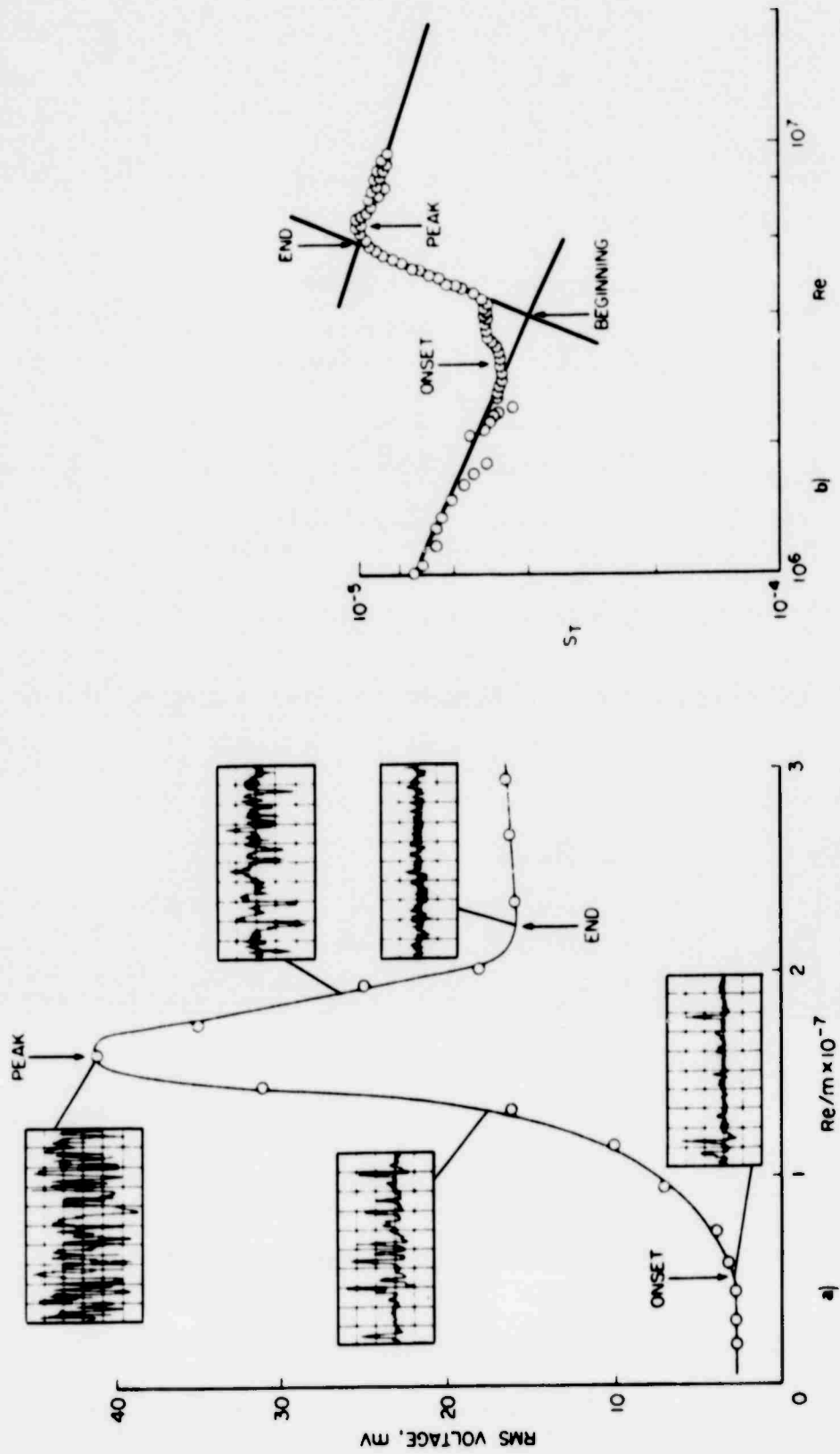


FIGURE 50 DETERMINATION OF TRANSITION LOCATION-
 a) THIN-FILM TECHNIQUE b) THERMOCOUPLE
 TECHNIQUE (REFERENCE 43)

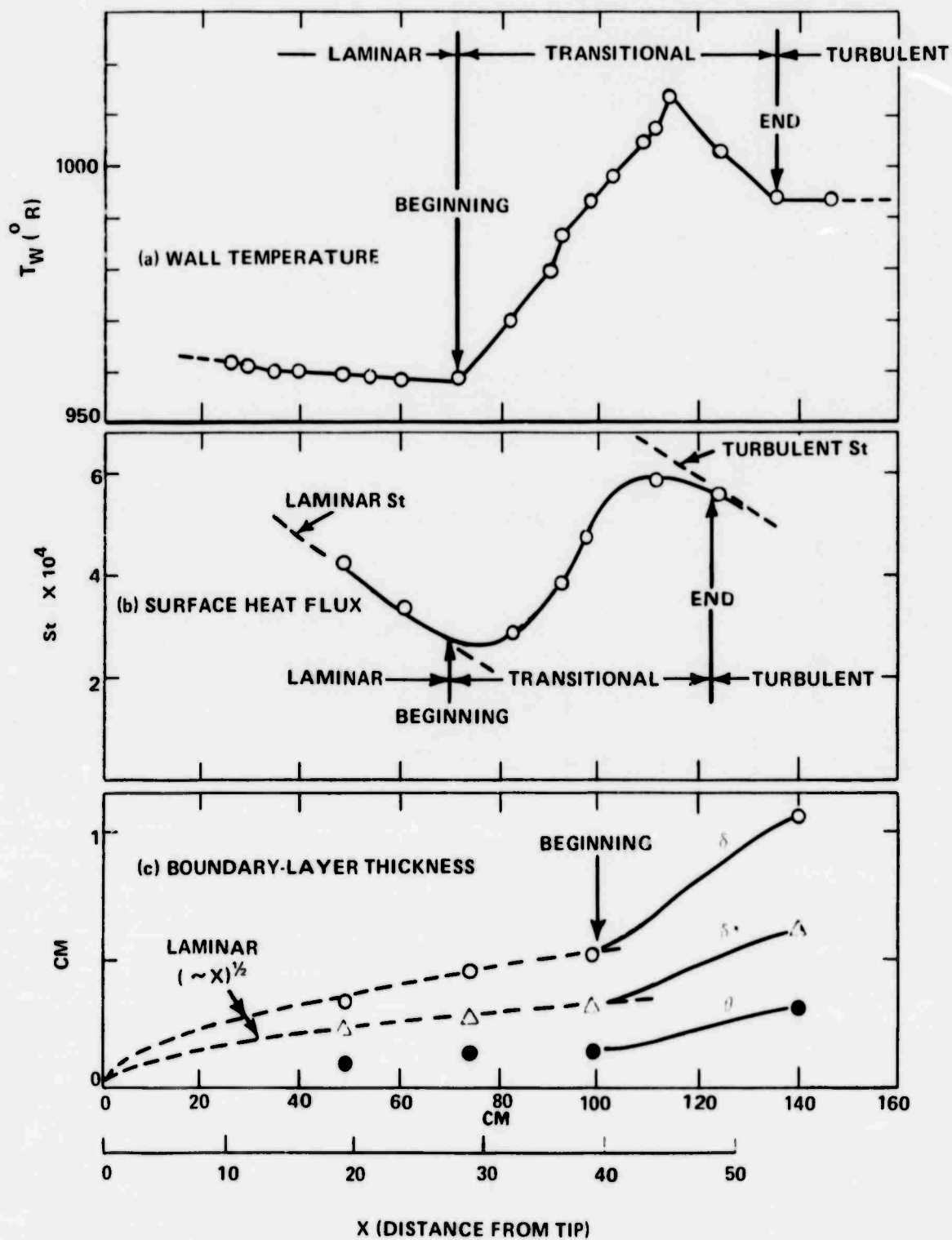


FIGURE 51 SURFACE TEMPERATURE AND HEAT FLUX, AND BOUNDARY-LAYER (REFERENCE 45)

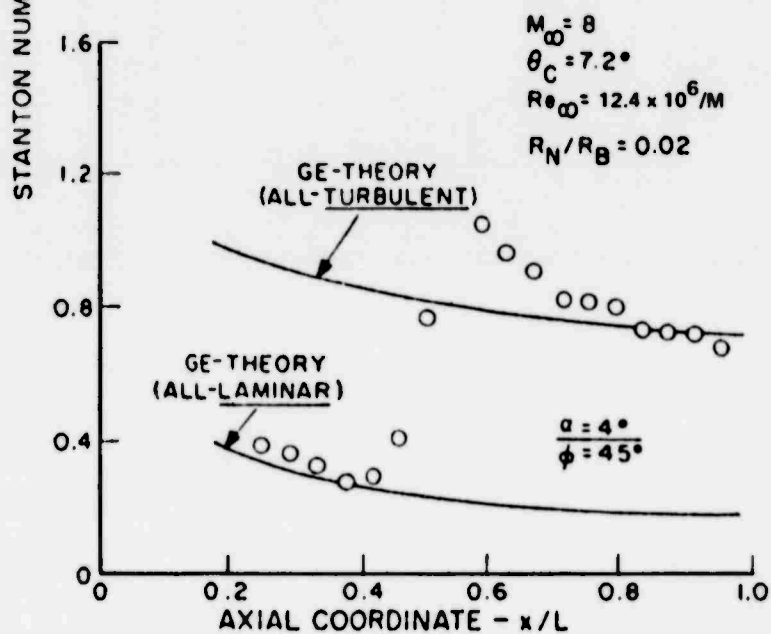
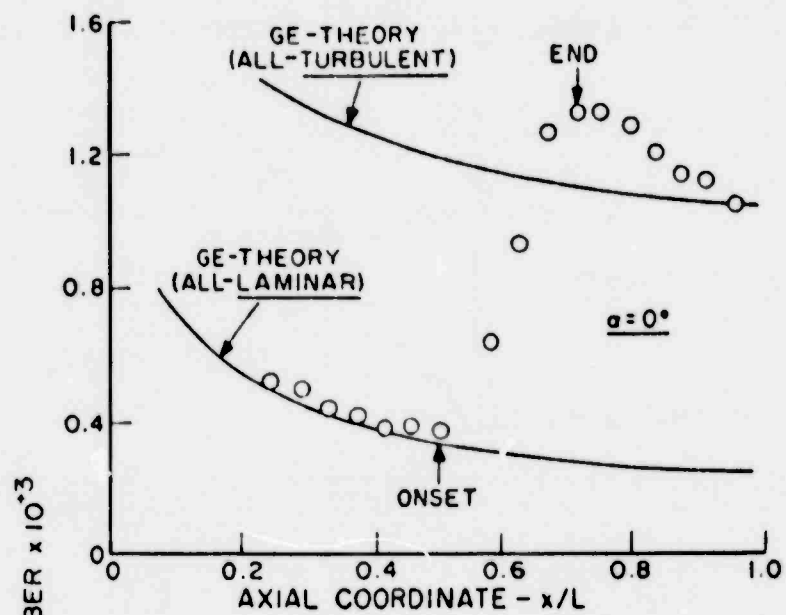


FIGURE 52 HEAT-TRANSFER DISTRIBUTION ON A CONE
 (REFERENCE 46)

Heating rate (heat flux or heat transfer) data have been plotted with Stanton number as the dependent variable by all three authors. The Stanton number is defined by the following relationship:

$$C_{n\infty} \equiv \frac{h}{C_p \rho_{\infty} V_{\infty}}$$

where h = heat flow film coefficient at the wall

C_p = specific heat

ρ_{∞} = gas density

V_{∞} = gas velocity.

6

Transitional features are noted by each author - onset, beginning, end, and peak. Onset is characterized by an upturn in the data away from the straight line given by the above equation where ρ_{∞} and V_{∞} are increasing. Beginning has been defined by Owen to be the point where the laminar slope and transition slope lines intersect. The peak is the maximum value of the data and the end is the point at which full turbulent slope intercepts the transition slope. It should be noted that Martellucci shows "end" at the peak rather than at the slope intercept (Figure 52), whereas Owen, et al show all four points - a beginning and an end which do not correspond with either of the other authors' definitions. (These comments are not intended to be critical of the individual workers, but rather to illustrate the lack of a common definition of transitional features.)

Owen also shows (Figure 50) definitions of transitional features based on thin film heating rate data and illustrates very strikingly the "burst" phenomena associated with transition. His data very neatly illustrate the transitional RMS

peak which also has been observed in experiments using microphone transducers.

Examples of thermocouple transducer assemblies used in these applications are shown in Figure 53; the majority of such devices which have been used in flight tests were designed and fabricated for the test and are not available as off-the-shelf devices. Typically, the thermocouples are placed in a bridge circuit and connected to an amplifier which provides the output.

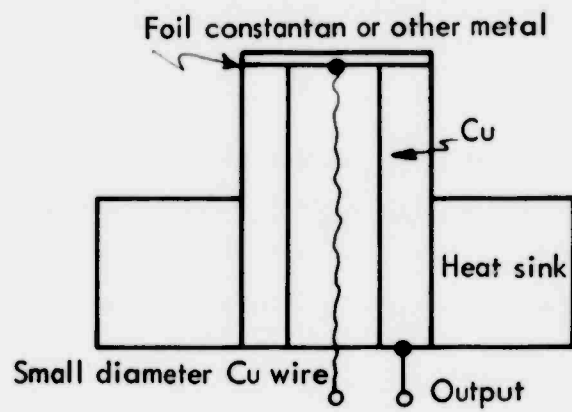
The Gardon gage in Figure 53(a) depends for its output on the slower rate of heat transfer from the center of a thin diaphragm to the edges which are in contact with the wall at a lower temperature. The rate of response depends on the diaphragm thickness and conductivity and on the center conductor diameter. This technique has been especially successful in wind tunnel experiments wherein the pressures and temperatures are both lower than in ICBM reentry. It can be seen that if the foil is thin, the device is very fragile and easily damaged.

The differential depth thermocouple pair (or " ΔT ") seen in Figure 53(b) has produced excellent flight test results. The General Electric Company has measured transition with response times shorter than 10 ms with this approach which was used on PVM and STM instrumented RV's. Failure occurs during reentry below transition altitude when the forward connection is ablated away.

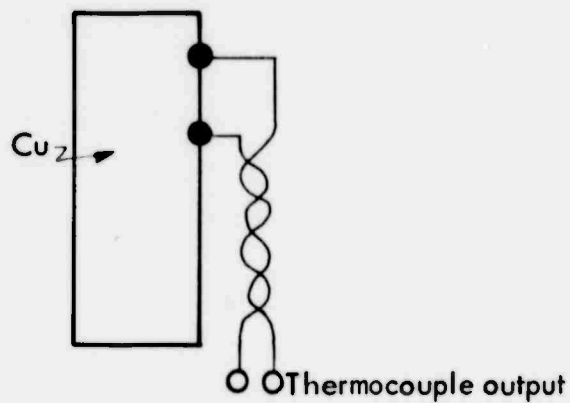
The final depiction in Figure 53(c) is a generalized view of a calorimeter which measures the integrated surface heat flux. The calorimeter output functions slowly when compared with the Gardon or ΔT types but is easily calibrated.

In addition to the above, Raman (Reference 47) used a very fast thin film thermocouple which responds essentially to the surface temperature. Mechanical features of the transducer he used are shown in Figure 54, which was taken from his report.

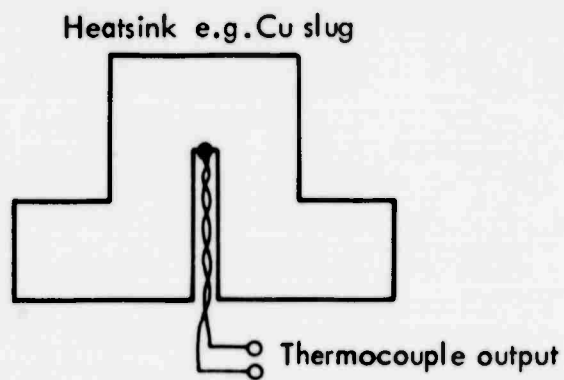
Thin films have been otherwise applied to measurement of fast-fluctuating heating rates by using them in resistive-type transducers at the surface of models. Owen (Reference 43, see also Figure 50 of this report) and Demetriades (Reference 45) both have made excellent measurements with thin films in wind tunnels. Owens stated that "more reliable results will always be obtained using thin-film gages" because it is easier to distinguish transition characteristics from thin film than it is thermocouple data.



a) FOIL OR GARDON TYPE



b) DIFFERENTIAL DEPTH THERMOCOUPLE OR ΔT TYPE



c) CALORIMETER TYPE

FIGURE 53 THERMOCOUPLE TECHNIQUE

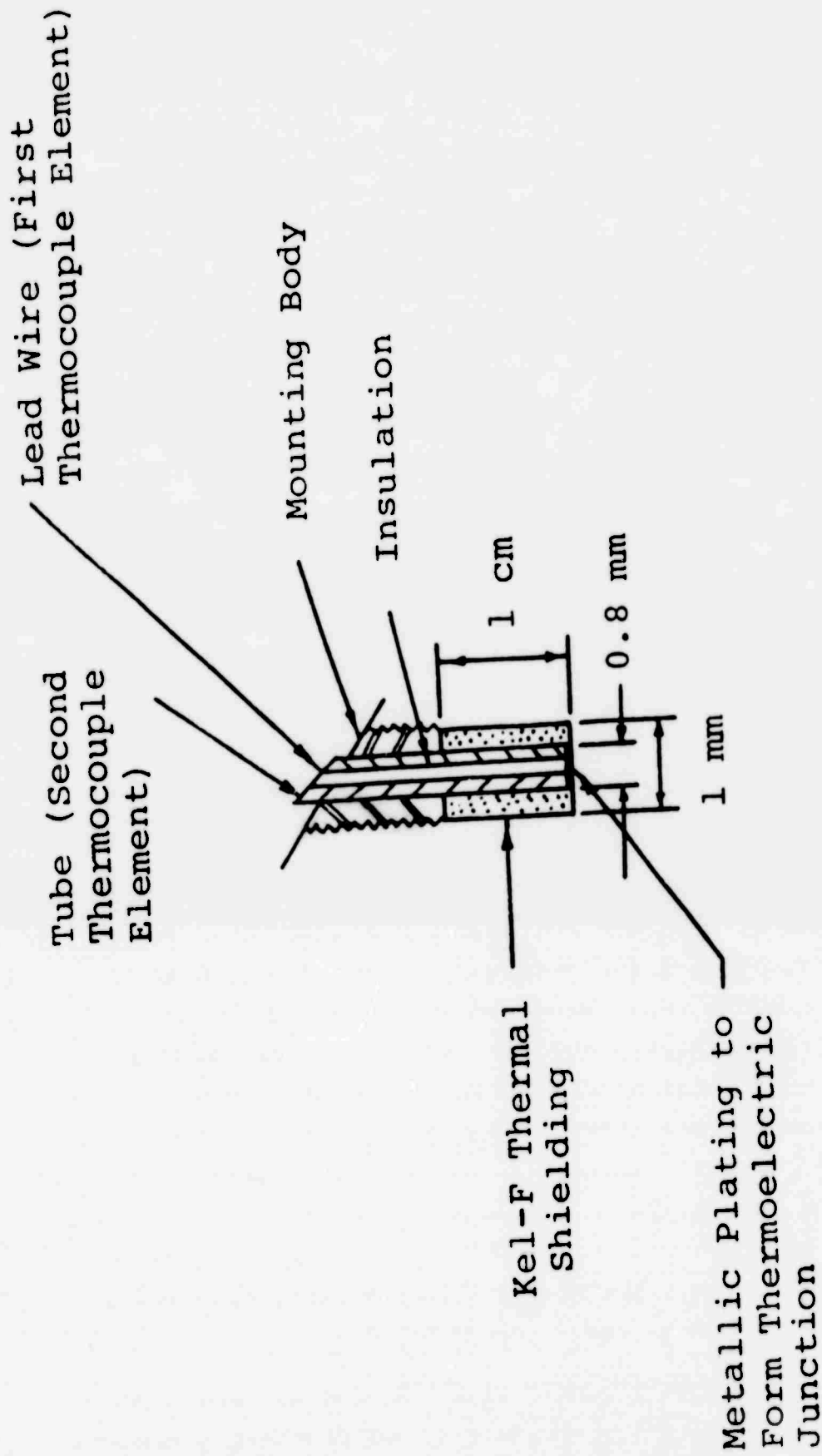


FIGURE 54 CROSS-SECTIONAL SCHEMATIC OF TCS SERIES PROBE
(REFERENCE 16)

4.0 CONCLUSIONS AND RECOMMENDATIONS

4.1 Conclusions

Analysis of the effects of asymmetrical boundary layer transition on conical reentry vehicles has shown that the most important effect of boundary layer transition on the vehicle forces and moments is the boundary layer thickening. This effect causes an increase in the normal pressure acting on the vehicle due to the boundary layer displacement effect. Using a postulated leeside favored transition, the induced pressure caused by the boundary layer displacement effect produces incremental forces and moments acting opposite to the inviscid forces and moments. Since the inviscid forces and moments, coupled with a positive vehicle static margin, produce the necessary static stability and angle of attack convergence during reentry, the induced pressure caused by leeside boundary layer transition can be expected to reduce this static stability and may even be a source of angle of attack divergence during the boundary layer transition event.

Comparisons between the wall shear stress and the induced pressure caused by the boundary layer displacement effect during transitional and fully-developed turbulent boundary layer flow has shown that the boundary layer displacement effect is of significantly greater importance than wall shear stress. The wall shear stress produces moments which tend to decrease the static stability during reentry below angles of attack of 1.5 degrees. Above 1.5 degrees, wall shear stress is found to increase vehicle static stability. Moments caused by the boundary layer displacement effect are approximately a factor of eight larger than moments derived from wall shear stress near zero degrees angle of attack.

The effects of surface mass transfer due to carbon phenolic ablation were found to be relatively unimportant with respect to the more significant boundary layer displacement effect.

Surface mass transfer contributes only approximately 10 percent to the net boundary layer displacement thickness for the transitional and fully-developed turbulent boundary layers.

If alterations in the static stability of reentry vehicles are the source of the observed transient behavior during boundary layer transition, then this analysis indicates that small angles of attack are essential prior to the boundary layer transition event before transient vehicle instabilities and angle of attack divergence can occur. This is because the incremental force and moment perturbations caused by asymmetrical boundary layer transition are significant with respect to the inviscid forces and moments at angles of attack of approximately 1 degree or less. The larger inviscid forces and moments which occur at the larger angles of attack are sufficient to overcome the asymmetrical boundary layer transition perturbations.

This analysis is incomplete in regard to the accurate specification of the dependence between the boundary layer asymmetrical transition pattern and vehicle angle of attack. Many investigators have attempted to determine this dependence experimentally using wind tunnel simulations. For instance, several investigators have found a strong dependence between the boundary layer transition asymmetry pattern and both angle of attack and body bluntness ratio. Wind tunnel simulations of boundary layer transition effects, however, must be viewed with some suspicion due to the great disparity in the observed transition unit Reynolds numbers between flight and wind tunnel environments.

A literature survey has been completed with the primary purpose to ascertain and assess methods which may be applied to measure pressures and determine location of transition of boundary layers on flight test reentry vehicles. Techniques

used in actual flight and in wind tunnel tests were sought and evaluated for the flight test application.

The conclusions reached concerning available transducers may be summarized as follows:

- 1) To measure vehicle forces, static pressure measurements with bandwidths up to 100 Hz desirable. The test results found in the survey of this measurement showed that sizable errors are encountered in some instances which are related to the interaction of the transducer with the boundary layer flow. Flush-mounted transducers and pitots inserted in the flow to be monitored provided the most accurate data with errors less than a few percent.

Other installations which used ports or inset transducers gave good data during laminar flow but produced erratic results during and after transition. Errors of 20 to 30% were observed in measurement of static pressure during turbulent flow on flight vehicles.

- 2) Acoustic pressure in boundary layers is a reliable measurand of transition location. Several experimenters used the noise from the boundary layer and achieved good results, in some cases in the presence of high level noise backgrounds in wind tunnel tests. Both ported and back-surface transducers were reported; back-surface transducers have the advantage that no penetration of the heatshield is required.

- 3) Temperature/Heating Rate Measurements. Temperature measurement devices provide excellent transition location data in moderate environments and function reasonably well in the more severe flight environment. Because of their inherent heat integrating (or calorimeter) characteristics, rapid response is difficult to achieve especially where measurements are to be made of an intermittent turbulent boundary layer. This is due mainly to heat diffusive time in heatshield or transducer materials being much longer than the changes in temperature at the heatshield surface.

Experimenters preferred thin film resistive devices over thermocouples if the application is permitted. Flight test data taken with thermocouples showed that transition beginning is detectable reliably, but later events are not detected. It should be noted, however, that temperature is not directly related to forces on the body.

4.2 Recommendations

In order that the effects of transition asymmetries can be fully understood it is recommended that fast-response transition monitors be used to fully map the development of turbulence in a flight test environment. These data would then be compared with the vehicle dynamic response data to determine the degree of correlation between trajectory perturbation and transition asymmetry.

In addition the following recommendations are submitted.

- 1) That new techniques be investigated for measurement of static pressure with an accuracy goal of 0.3 n/m^2 during the transition period. This is a technically challenging task because of the reentry vehicle boundary layer environment, but is not beyond transducer state-of-the-art. This measurement need only to have bandwidths from 0 to 100 Hz.

- 2) That additional emphasis be given to boundary layer acoustic noise measurements, especially those which can be made from the back surface of the heatshield, not contacting the hypersonic flow of the boundary layer. There was some optimism in the few reports of this type of measurement that transition asymmetries can be readily detected with the noise generated by turbulence.

5.0 REFERENCES/BIBLIOGRAPHY

1. Gregorek, G. M. and Korkan, K. D., Hypersonic Blunt Body Similitude in a Perfect Gas, Air Force Flight Dynamics Laboratory FDL-TDR-64-92, Wright-Patterson Air Force Base, June 1964.
2. Simon, W. E. and Walters, L. A., Approximations for Supersonic Flow Over Cones, AIAA Journal, Volume 2, No. 7, July 1963.
3. Inouye, M., Blunt Body Solutions for Spheres and Ellipsoids in Equilibrium Gas Mixtures, NASA TN D-2780, May 1965.
4. Arne, C. L., et al, Subject of Flight Tests, MDAC, April 1968.
5. Lees, L., Laminar Heat Transfer Over Blunt Nosed Bodies at Hypersonic Speeds, Jet Propulsion, Volume 26, No. 4, April 1956.
6. Walker, G. K., The Growth of Laminar Boundary Layers With Zero Pressure Gradient, General Electric Company, GE-MSVD TFM-8151-008, January 1963.
7. Walker, G. K., A Particular Solution to the Turbulent Boundary Layer Equations, Journal of the Aeronautical Sciences, Volume 27, No. 9, September 1960.
8. Walker, G. K. and Schuman, B. A., The Growth of Turbulent Boundary Layers, General Electric Company GE-MSVD TIS R61SD123, July 1961.

9. Hansen, C. F., Approximations for the Thermodynamics and Transport Properties of High Temperature Air, NASA TR-50, 1959.
10. Lees, L., Convective Heat Transfer with Mass Addition and Chemical Reactions, Third AGARD Colloquium, Palermo, Sicily, 1958.
11. Scala, S. M. and Gilbert, L. M., Sublimation of Graphite at Hypersonic Speeds, AIAA Journal, Volume 3, No. 9, September 1965.
12. Fogaroil, R. P. and Brant, D. N., Reevaluation of Graphite Thermochemical Ablation, General Electric Company, TFM 9151-060, October 1968.
13. Miner, E. W., Anderson, E. C. and Lewis, C. H., A Computer Program for Two-Dimensional and Axisymmetric Nonreacting Perfect Gas and Equilibrium Chemically Reacting Laminar, Transitional and/or Turbulent Boundary Layer Flows, VPI-E-71-8, May 1971.
14. Van Driest, E. R., On Turbulent Flow Near A Wall, Journal of the Aeronautical Sciences, Volume 23, No. 11, November 1956.
15. Inouye, M., Rakich, J. and Lomax, H., A Description of Numerical Methods and Computer Programs for Two-Dimensional and Axisymmetric Supersonic Flow Over Blunt Nosed and Flared Bodies, NASA TN D-2970, August 1965.
16. Frieders, M. C. and Lewis, C. H., Effects of Mass Transfer into Laminar and Turbulent Boundary Layers Over Cones at Angle of Attack, VPI-AERO-031, March 1975.

17. Moore, F. K., "Three Dimensional Boundary Layer Theory," Advances in Applied Mechanics, Vol. 4, Academic Press, N. Y., 1956.
18. Adams, J. C., Implicit Finite Difference Analysis of Compressible Laminar, Transitional, and Turbulent Boundary Layers Along the Windward Streamline of a Sharp Cone at Incidence, AEDC TR-71-235, December 1971.
19. Reichardt, H., Vollständige Darstellung der Turbulenten Geschwindigkeitsverteilung in Glatten Lutungen, ZAMM, Volume 31, 1951.
20. Cebeci, T., Behavior of Turbulent Flow Near a Porous Wall With Pressure Gradient, AIAA Journal, Volume 8, No. 12, December 1970.
21. Klebanoff, P. S., Characteristics of Turbulence in a Boundary Layer With Zero Pressure Gradient, NASA TN-3178, 1954.
22. Dhawan, S. and Narashima, R., Some Properties of Boundary Layer Flow During the Transition from Laminar to Turbulent Flow, Journal of Fluid Mechanics, Volume 3, No. 4, April 1958.
23. McGowan, J. J. and Davis, R. T., Development of a Numerical Method to Solve the Three Dimensional, Compressible, Laminar Boundary Layer Equations with Applications to Elliptical Cones at Angle of Attack, Aerospace Research Laboratories ARL 70-0341, Wright-Patterson AFB, December 1970.
24. Dwyer, H. A., Boundary Layer on a Hypersonic Sharp Cone at Small Angle of Attack, AIAA Journal, Volume 19, No. 2, February 1971.

25. Krause, E., Comment on "Solution of a Three Dimensional Boundary Layer Flow with Separation", AIAA Journal, Volume 7, No. 3, March 1969.
26. Richtmyer, R. D., Difference Methods for Initial Value Problems, Interscience Publishers, New York, 1957.
27. Rakich, J. V., A Method of Characteristics for Steady Three Dimensional Supersonic Flow with Application to Inclined Bodies of Revolution, NASA TN D-5341, October 1969.
28. Jones, D. J., Numerical Solutions of the Flow Field for Conical Bodies in a Supersonic Stream, NRC Aeronautical Report LR-507, July 1968.
29. White, Pritchard H., Effect of Transducer Size, Shape, and Surface Sensitivity on the Measurement of Boundary Layer Pressures, The Journal of the Acoustical Society of America, Volume 41, No. 5, 1967, p. 1358.
30. Lewis, T. L. and Dods, J. B., Jr., Wind-Tunnel Measurements of Surface Pressure Fluctuations at Mach Numbers of 1, 6, 2.0, and 2.5 Using 12 Different Transducers, NASA TN D-7087, October 1972.
31. Heller, H. and Widnall, S., Dynamics of an Acoustic Probe for Measuring Pressure Fluctuations on a Hypersonic Reentry Vehicle, The Journal of the Acoustical Society of America, Volume 44, No. 4, 1968, p. 885.
32. Johnson, R., Macourek, M., Saunders, H., Boundary Layer Acoustic Measurements in Transitional and Turbulent Flow at $M_\infty = 4.0$, AIAA Paper 69-344, AIIA 4th Aerodynamics Testing Conference, April 1969.

33. Franklin, R. and Wallace, J., Absolute Measurements of Static-Hole Error Using Flush Transducers, J. Fluid Mechanics (1970), Volume 42, Pt. 1, pp. 33-48.
34. Coe, C. F., "Surface-Pressure Fluctuations Associated with Aerodynamic Noise," Basic Aerodynamic Noise Research, NASA-SP-207, U. S. GPO, Washington, D. C., p. 409.
35. Cassanto, J. M. and Rogers, D. A., An Experiment to Determine Nose Tip Transition With Fluctuating Pressure Measurements (Ground Test Data), AIAA Paper No. 74-625, July 1974.
36. Cassanto, J. M., An Assessment of Port Erosion Effects, AIAA Paper 75-150, January 1975.
37. Cassanto, J. M., A Miniature Solid-State Pressure Transducer for R/V Flight Test Applications, Journal of Spacecraft and Rockets, Volume 12, No. 2, February 1975, p. 121.
38. Cassanto, J. M., Monfort, A. and Fehl, C., An Experiment to Determine the Existence of R/V Nose Tip Transient Shocks, AIAA Paper 76-54, January 1976
39. Erwin, T. and Farrentine, J., Subject of Flight Test Results, General Electric Company, October 1973.
40. Reshotko, Eli, A Program for Transition Research, AIAA Journal Volume 13, No. 3, March 1975, p. 261.
41. Kendall, J. M., Wind Tunnel Experiments Relating to Supersonic and Hypersonic Boundary-Layer Transition, AIAA Journal, Volume 13, No. 3, March 1975, p. 290.

42. Beckwith, I. E., Development of a High Reynolds Number Quiet Tunnel for Transition Research, AIAA Journal, Volume 13, No. 3, March 1975.
43. Owen, F. K., et al, Comparison of Wind Tunnel Transition and Freestream Disturbance Measurements, AIAA Journal, Volume 13, No. 3, March 1975, p. 266.
44. Harvey, W. D., et al, Nozzle Wall Boundary Layer Transition and Freestream Disturbances at Mach 5, AIAA Journal, Volume 13, No. 3, March 1975, p. 307.
45. Demetriades, A., Hydrodynamic Stability and Transition to Turbulence in the Hypersonic Boundary Layer Over a Sharp Cone, Aeronutronic Ford Publication U-6139, Interim Progress Report October 1974-March 1975, 15 April 1975.
46. Martellucci, A. and Neff, R. S., Influence of Asymmetric Transition on Reentry Vehicle Characteristics, J. of Spacecraft, Volume 8, 1 May 1971, p. 476.
47. Raman, K. R., A Study of Surface Pressure Fluctuations in Hypersonic Turbulent Boundary Layers, NASA CR-2386, February 1974.
48. Williams, D. J. M., Measurements of the Surface Pressure Fluctuations in a Turbulent Boundary Layer in Air at Supersonic Speeds, University of Southampton, England, December 1960.
49. Owen, F. K., et al, Comparison of Wind Tunnel Transition and Freestream Disturbance Measurements, AIAA Journal, Volume 13, No. 3, March 1975, pp. 266-269.

50. Johnson, R. and Saunders, H., "New Avenues of Boundary Layer Acoustics Research," Basic Aerodynamic Noise Research, NASA-SP-207, U. S. GPO, Washington, D. C., p. 493.
51. Pierce, H. and Mayes, W., "Hypersonic Boundary Layer Noise Measurement," Basic Aerodynamic Noise Research, NASA-SP-207, U. S. GPO, Washington, D. C., p. 337.
52. Willmarth, William A., Wall Pressure Fluctuations in a Turbulent Boundary Layer, NACA-TN-4139, March 1958.
53. Kistler, A. L. and Chen, W. S., The Fluctuating Pressure Field in a Supersonic Turbulent Boundary Layer, Journal of Fluid Mechanics, Volume 16, Pt. 1, May 1963.
54. Serafini, J. S., Wall Pressure Fluctuations and Pressure-Velocity Correlations in a Turbulent Boundary Layer, NASA TR R-165, December 1963.
55. Speaker, W. V. and Ailman, C. M., Spectra and Space-Time Correlations of the Fluctuating Pressures at a Wall Beneath a Supersonic Turbulent Boundary Layer Perturbed by Steps and Shock Waves, NASA CR-486, May 1966.
56. White, Pritchard H., Effect of Transducer Size, Shape, and Surface Sensitivity on the Measurement of Boundary Layer Pressures, Journal of Acoustical Society of America, Volume 41, No. 5, 1967.
57. Chubb, T. W., The Response of a Narrow Bore Pressure Measuring System to Step and Oscillatory Pressures, Royal Aircraft Establishment, Technical Report 68010, January 1968.
58. Harvey, W. D., Bushnell, D. M. and Beckwirth, I. E., Fluctuating Properties of Turbulent Boundary Layers for Mach Numbers up to 9., NASA TN D-5496, October 1969.

59. Raman, K. R., Subminiature Sensor for Unsteady Pressures, Tech Brief 71-10114, May 1971.
60. Pate, S. R. and Brown, M. D., Acoustic Measurements in Supersonic Transitional Boundary Layers, AIAA Paper No. 69255.
61. Cooper, L., Kriebel, A. R., and Tickner, E. G., Reentry Vehicle Acoustical Environment Study, Aerotherm Technical Note 74-23, May 1974.
62. Church, J. M., Miniature Transducer Assembly for Measuring the Properties of the Wall-Pressure Field in Turbulent Flows, The Journal of the Acoustical Society of America, Volume 40, No. 1, 1966, p. 254.
63. Bies, D. A., A Review of Flight and Wind Tunnel Measurements of Boundary Layer Pressure Fluctuations and Induced Structural Response, NASA CR-626, 1966.
64. Potter, J. L., Boundary-Layer Transition on Supersonic Cones in an Aeroballistic Range, AIAA Journal, Volume 13, No. 3, March 1975.
65. Kirsch, A. A., A Proposed Dynamic Stability Solution, AIAA Paper No. 73-100, January 1973.
66. Cassanto, J. and George, F., A New Concept for Low-Range Pressure measurements on Full-Scale Reentry Vehicles, Journal of Spacecraft, Volume 16, No. 10, October 1969, p. 1184.
67. Lewis, T. L. and Banner, R. D., Boundary Layer Transition Detection on the X-15 Vertical F in Using Surface Pressure-Fluctuation Measurements, NASA TM X-2466, December 1971.

68. Martellucci, A., et al, Analysis of Flight Test Transition and Turbulent Heating Data, Part I, Boundary Layer Transition Results, NASA CR-129045, November 1972.
69. Flame V Flight Test Results, Acoustic Monitor Presentation to SAMSO, Kaman Sciences Corporation, November 1975.

DISTRIBUTION LIST

DEPARTMENT OF DEFENSE

Director
Defense Advanced Research Project Agency
ATTN: Strategic Tech. Office

Defense Communication Engineer Center
ATTN: Code 720, John Worthington

Director
Defense Communications Agency
ATTN: NMCSSC, Code 510

Defense Documentation Center
12cy ATTN: TC

Director
Defense Intelligence Agency
ATTN: DI-7D
ATTN: DT-1C, Nuc. Eng. Branch
ATTN: DT-2, Wpns. & Sys. Division

Director
Defense Nuclear Agency
ATTN: STSI, Archives
ATTN: DDST
ATTN: STSP
3cy ATTN: STTL, Tech. Library
3cy ATTN: SPAS

Director of Defense Rsch. & Engineering
ATTN: DD/S&SS
ATTN: AD/DS
ATTN: AD/OS

Commander
Field Command
Defense Nuclear Agency
ATTN: FCTMOF
ATTN: FCPR
ATTN: FCTMD

Director
Joint Strat. Tgt. Planning Staff, JCS
ATTN: JLTW-2
ATTN: JPTM
ATTN: JPTP

Chief
Livermore Division, Field Command, DNA
ATTN: FCPRL

OJCS/J-5
ATTN: J-5, Plans & Policy R & D Division

DEPARTMENT OF THE ARMY

Program Manager
BMD Program Office
ATTN: DACS-BMZ
ATTN: DACS-BMT, John Shea
ATTN: DACS-BMZ-D, Julian Davidson
ATTN: DACS-BMT, Clifford E. McLain

Commander
BMD System Command
ATTN: BDMSC-TEN, Noah J. Hurst

DEPARTMENT OF THE ARMY (Continued)

Dep. Chief of Staff for Rsch. Dev. & Acq.
ATTN: NCB Division

Deputy Chief of Staff for Ops. & Plans
ATTN: Dir. of Chem. & Nuc. Ops.

Commander
Harry Diamond Laboratories
ATTN: DRXDO-RC, Robert B. Oswald, Jr.
ATTN: DRXDO-NP
ATTN: DRXDO-RBH, James H. Gwaltney

Commander
Picatinny Arsenal
ATTN: SMUPA-MD, Henry Opat
ATTN: SARPA-ND-C-T, Donald Miller
ATTN: SARPA-FR-E, Louis Avrami

Commander
TRASANA
ATTN: R. E. DeKinder, Jr.

Director
U. S. Army Ballistic Research Labs.
ATTN: Robert E. Fichelberger
ATTN: DRXBR-TB, J. T. Frasier
ATTN: DRXRD-BVL, William J. Schuman, Jr.

Commander
U. S. Army Mat. & Mechanics Rsch. Ctr.
ATTN: DRXMR-III, John F. Dignam

Commander
U. S. Army Materiel Dev. & Readiness Cmd.
ATTN: DRCDE-D, Lawrence Flynn

Commander
U. S. Army Missile Command
ATTN: DRSMI-XS, Chief Scientist
ATTN: DRSMI-RRR, Bud Gibson
ATTN: DRS-RKP, W. B. Thomas
ATTN: DRCPM-PE-EA, Wallace O. Wagner

Commander
U. S. Army Nuclear Agency
ATTN: ATCA-NAW

DEPARTMENT OF THE NAVY

Chief of Naval Material
ATTN: Mat. 0323, Irving Jaffe

Chief of Naval Operations
ATTN: OP 985D
ATTN: OP 62
ATTN: OP 985

Chief of Naval Research
ATTN: Code 464, Thomas P. Quinn

Director
Naval Research Laboratory
ATTN: Gerald Cooperstein, Code 7770
ATTN: Marlo A. Persechino, Code 5180
ATTN: Tech. Library, Code 2027

DEPARTMENT OF THE NAVY (Continued)

Commander
Naval Sea Systems Command
ATTN: 0333A, Marlin A. Kinna

Commander
Naval Surface Weapons Center
ATTN: Code 323, W. Carson Lyons
ATTN: Code WA501, Navy Nuc. Prgms. Off.
ATTN: Code 2302, Leo F. Gowen

Director
Strategic Systems Project Office
ATTN: NSP-272, CDR Leslie Stoessl

DEPARTMENT OF THE AIR FORCE

AF Materials Laboratory, AFSC
ATTN: MAS
ATTN: MBC, Donald L. Schmidt
ATTN: T. Nicholas

AF Rocket Propulsion Laboratory, AFSC
ATTN: RTSN, G. A. Beale

AF Weapons Laboratory, AFSC
ATTN: SUL
ATTN: DYS, Lt E. J. Burns
ATTN: DYV
ATTN: Dr. Minge

Commander
Foreign Technology Division, AFSC
ATTN: TDFBD, J. D. Pumphrey
ATTN: TDPTN

Hq. USAF/RD
ATTN: RDPM
ATTN: RDQ
ATTN: RDQSM
ATTN: RD
ATTN: RDQPN

SAMSO/DY
ATTN: DYS

SAMSO/MN
ATTN: MNNR

SAMSO/RS
ATTN: RSSE
ATTN: RSS

Commander in Chief
Strategic Air Command
ATTN: DOXT
ATTN: XPFS

ENERGY RESEARCH AND DEVELOPMENT ADMIN

Division of Military Application
ATTN: Doc. Con. for Res. & Dev. Branch
ATTN: Doc. Con. for CDR Richard E. Peterson
ATTN: Doc. Con. for LTC Donald L. McNutt

University of California
ATTN: C. Joseph Taylor, L-92
ATTN: Joseph E. Keller, Jr., L-125
ATTN: G. Staihle, L-24

ENERGY RESEARCH AND DEVELOPMENT ADMIN
(Continued)

Los Alamos Scientific Laboratory
ATTN: Doc. Con. for J. W. Taylor
ATTN: Doc. Con. for John McQueen
ATTN: Doc. Con. for R. S. Thurston

Sandia Laboratories
ATTN: Raymond Ng
ATTN: Doc. Con. for T. Gold
ATTN: Doc. Con. for C. S. Hoyle
ATTN: Doc. Con. for 8131, H. F. Norris, Jr.

Sandia Laboratories
ATTN: Doc. Con. for Albert Chabai
ATTN: Doc. Con. for R. R. Boade
ATTN: Doc. Con. for D. McCloskey

DEPARTMENT OF DEFENSE CONTRACTORS

Aeronautical Rsch. Assoc. of Princeton, Inc.
ATTN: Coleman Donaldson

Aeronutronic Ford Corporation
Aerospace & Communications Ops.
Aeronutronic Division
ATTN: P. Spangler

Aerospace Corporation
ATTN: W. Barry
ATTN: R. Allen
ATTN: Richard Crolius, A2-RM1027

Avco Research & Systems Group
ATTN: John Gilmore, J400
ATTN: John E. Stevens, J100

Battelle Memorial Institute
ATTN: Merwyn R. Vanderlind
ATTN: W. Pfeifer

The Boeing Company
ATTN: Brian Lemplere

Brown Engineering Company, Inc.
ATTN: Ronald Patrick

Effects Technology, Inc.
ATTN: Robert Wengler

General Electric Company
Space Division
ATTN: G. Harrison
ATTN: Carl Anderson
ATTN: Phillip Cline

General Electric Company
TEMPO-Center for Advanced Studies
ATTN: DASIAC

General Research Corporation
ATTN: Robert E. Rosenthal

Institute for Defense Analyses
ATTN: Joel Bengston
ATTN: IDA Librarian, Ruth S. Smith

Ion Physics Corporation
ATTN: Robert D. Evans

DEPARTMENT OF DEFENSE CONTRACTORS
(Continued)

Kaman Aavidyne
Division of Kaman Sciences Corp.
ATTN: Norman P. Hobbs

Kaman Sciences Corporation
ATTN: Albert P. Bridges
ATTN: Thomas Meagher
ATTN: Frank H. Shelton
ATTN: Jerry L. Harper
ATTN: J. C. Nickell
ATTN: V. D. Peckham
ATTN: John R. Hoffman

Lockheed Missiles and Space Company
ATTN: A. P. Hardt
ATTN: Lloyd F. Chase
ATTN: Raymond R. Capioux
ATTN: F. G. Borgardt

Martin Marietta Aerospace
ATTN: Laird Kinnaird

McDonnell Douglas Corporation
ATTN: L. Cohen
ATTN: J. Kirby
ATTN: J. F. Garibotti
ATTN: R. J. Reck

National Academy of Sciences
ATTN: National Materials Advisory Board for
Donald G. Groves

Northrop Corporation
ATTN: Don Hicks

Physics International Company
ATTN: Doc. Con. for James Shea

DEPARTMENT OF DEFENSE CONTRACTORS
(Continued)

Prototype Development Associates, Inc.
ATTN: John Slaughter

R & D Associates
ATTN: Albert L. Latter
ATTN: Jerry Carpenter
ATTN: Harold L. Brode
ATTN: F. A. Field

Science Applications, Inc.
ATTN: R. Fisher
ATTN: G. Ray

Science Applications, Inc.
ATTN: J. Courtney

Southern Research Institute
ATTN: C. D. Pears

Stanford Research Institute
ATTN: Donald Curran
ATTN: Herbert E. Lindberg
ATTN: George R. Abrahamson

Stanford Research Institute
ATTN: Harold Carey

Systems, Science and Software, Inc.
ATTN: G. A. Gurtman
ATTN: Russell E. Duff

Terra Tek, Inc.
ATTN: Sidney Green